Towards depth-resolved multi-cubic-centimeter field of view endoscopic camera for intraoperative nerve identification.

By

Yong-Chul Yoon

Submitted to the Harvard-MIT Program in Health Sciences and Technology
in Partial Fulfillment of the Requirements for the Degree of
Doctor of Philosophy in Medical Engineering and Medical Physics
at the
MASSACHUSETTS INSTITUTE OF TECHNOLOGY
September 2024

Authored by: Yong-Chul Yoon
Harvard-MIT Program in Health Sciences and Technology
August 13, 2024

Certified by: Benjamin J. Vakoc, PhD
Associate Professor of Harvard Medical School
Wellman Center for Photomedicine at Massachusetts General Hospital
Member of the Harvard-MIT Health Sciences & Technology Faculty
Thesis Supervisor

Accepted by: Collin M. Stultz, MD, PhD
Director, Harvard-MIT Health Sciences and Technology program
Nina T. and Robert H. Rubin Professor in Medical Engineering and Science
Professor of Electrical Engineering and Computer Science, MIT

Towards depth-resolved multi-cubic-centimeter field of view endoscopic camera for intraoperative nerve identification.

by

Yong-Chul Yoon

Submitted to the Harvard-MIT Program in Health Sciences and Technology
on August 16, 2024 in partial fulfillment of the requirements for the degree of

DOCTOR OF PHILOSOPHY IN MEDICAL ENGINEERING AND MEDICAL PHYSICS

ABSTRACT

One out of every five peripheral nerve injuries in the United States has an iatrogenic origin. These injuries can cause chronic neuropathies, paresthesia, and varying functional losses. To reduce the risk of nerve injury, surgeons meticulously identify and track nerves within the surgical field using white-light magnification. However, small (sub-millimeter diameter) and buried nerves are often difficult to identify with this approach. This has motivated a long-standing effort to develop improved nerve visualization technologies that are deployable in both open and minimally invasive surgical workflows. Fluorescence imaging is the most commonly explored strategy, and multiple exogenous fluorophores that bind to nerve-specific targets have been developed. However, fluorescence imaging has several limitations, including a disrupted workflow (due to the need for specialized lighting) and a significant regulatory burden. For these reasons, fluorescence-based nerve visualization has not yet been clinically adopted.

Polarization-based optical coherence tomography (OCT) approaches to nerve visualization would inherently mitigate each of these translational challenges. First, OCT imaging is not affected by room light and thus can be used simultaneously with surgical lighting. Second, OCT is label-free and avoids regulatory pathways associated with new drug development. However, because OCT offers high-resolution, three-dimensional imaging. a surgical OCT

system supporting video-rate acquisition of cubic centimeter fields would require signal capture bandwidths that are several orders of magnitude higher than what is available today. It is unlikely that this gap will be addressed through incremental advances in existing OCT platforms.

In this thesis, we present a radically different OCT platform designed to aggressively reduce signal capture bandwidths while also simplifying the optical and electronic subsystem designs. The proposed approach is contour-looping (CL-) OCT (pronounced cloaked). It retains the depth-sectioning capability upon which OCT is based but discards the requirement of comprehensive three-dimensional imaging that results in impractical signal capture bandwidths. As such, CL-OCT defines a strategy for low-bandwidth depth-sectioned imaging that may be sufficient for specific imaging tasks such as nerve identification. Importantly, the CL-OCT platform is compatible with a camera-based (i.e., scan-free) deployment that is advantageous for endoscopic deployments. In a second component of this thesis, we provide extensive theoretical and experimental studies on how optical amplifiers can be used in OCT to address sensitivity challenges of high-speed surgical OCT platforms like CL-OCT. Together, these lines of research define a new approach to meeting the need for OCT-based solutions for intraoperative nerve identification. This technology, if successfully translated, may lead to a lower incidence of iatrogenic nerve injury.

Thesis supervisor: Benjamin J. Vakoc
Title: Associate Professor at Harvard Medical School, Wellman Center for Photomedicine, Massachusetts General Hospital, Member of the Harvard-MIT Health Sciences Technology Faculty

Acknowledgments

First and foremost, I would like to thank my mentor, Ben Vakoc, for the guidance on research matters and for supporting me in all (good and bad) of my life events: A temporary COVID lab closure, my wedding, a random health issue of unknown cause, and finally the birth of my son on 06/22/2024. The immense intellectual and professional growth over the past five years was possible because of your effective mentorship and communication style. Also, I would like to thank my academic mentor, Brett Bouma, for keeping me on track and offering big-picture career advice. I am also grateful to former and current lab members for bouncing off crazy research ideas with me during my time in the Vakoc lab: Mohsen, Stephanie, Tae Shik, Hyun-Sang, Jongyoon, Danielle, and, especially, Yongjoo.

Outside the lab, I owe a lot to my friends and community members. First, I thank my former housemates Alan Zhang and Brian Do for fun discussions over meals and board games. Rohan Thakur, my fellow MEMP friend, your enthusiasm for science and microfluidics always keeps me on my toes - thank you. I appreciate the past and current Midnight Motion musicians Jon, Ben, Aaron, Abby, Graham, Sadie, Ben O, and Paul for keeping me company and being funky. I also want to thank the OHCC families for keeping me grounded.

Finally, and most importantly, I thank my family - Elizabeth, Daniel (although you are just getting used to the outside world), Yeon, Sunghee, and HyungChul - and the Lindquist family - Mark, Kristin, Rachel, Catie, Sarah, Merriam, Suzanna, Sophia, Bethany, Grammy, and Farfar - for their unwavering support and love. It truly has been a journey filled with many blessings; I could not have done it alone.

Contents

List of Figures

List of Tables

Chapter 1

Introduction

1.1 Clinical Overview

Nerve injuries during surgery are surprisingly common. Of all traumatic nerve injuries, approximately 20-25 % of them are iatrogenic [1][2]. There are various mechanisms of injury: (1) direct nerve damage by surgical tools, (2) pressure due to surgical position, (3) compression of hematoma, (4) tourniquet, (5) dressings, casts, or orthotic devices, (5) injection of neurotoxic substance, and (6) radiation [1]. But, the most prevalent is the first one. A large-scale study showed that 25% of sciatic nerve lesions, 94% of accessory nerve lesions, and 60% of femoral nerve lesions that required treatment were iatrogenic [1]. They have been reported for various kinds of orthopedic surgery, head and neck surgery, and facial reconstruction surgery. [3][4][5]. The most frequently damaged nerves in these open surgeries were the median nerve, followed by the accessory nerve, radial nerve, and peroneal nerve [6]. These nerve damages could lead to various side effects including temporary or permanent facial paralysis (in case of trigeminal nerve damage), and loss of function [7]. Nerve injuries are also common in minimally invasive surgeries (MIS) for tumor removal. In robotic-assisted laparoscopic prostatectomy, surgeons rely on experience and certain anatomical landmarks to spare cavernous nerves and the neurovascular bundle to minimize surgical complications due to nerve damages including temporary or permanent impotence, paresthesia, and phantom pains [8][9][10]. A conventional surgical microscope based on white-light imaging is insufficient to identify exposed and superficially embedded nerves. There is a clinical need

for a real-time, label-free visualization tool that improves the accuracy of nerve identification and possibly reduces the incidence of iatrogenic nerve injuries.

1.2 Technical Overview

Optical coherence tomography (OCT) provides high-resolution, three-dimensional tomographic images of weakly scattering samples. Conceptually, OCT works like ultrasound (US). It measures the time delay of optical echoes from inhomogeneous tissue boundaries. The magnitude of the echo is proportional to the square root of the local reflectivity and the delay localizes the origin of the reflection. At optical frequencies (100 THz), a micrometer resolution is achievable. However, modern electronics cannot directly respond to optical frequency, which is more than six orders of magnitude faster than the ultrasonic frequency (10 MHz). For this reason, OCT employs an interferometric technique to down-convert the frequency by coherently mixing the backscattered sample light with a reference field. Coherent detection also has a significant sensitivity advantage compared to direct detection. This allows OCT to image much deeper into the scattering medium than other optical imaging modalities like confocal microscopy. The fact that OCT has a resolution much higher than that of US and a penetration depth longer than microscopy makes it a unique imaging modality for certain biomedical applications.

James G. Fujimoto's group at MIT developed the first OCT system for imaging the eye *in vivo* circa 1991 [11]. They showed that OCT can identify the retinal nerve fiber layer (RNFL), a highly scattering structure important in glaucoma, based on intensity contrast. Their system had FWHM axial and lateral resolution of 2 μm and 9 μm in air, respectively, with -100 dB system sensitivity. The structural OCT image showed an excellent match with the histology slide of the identical sample. However, imaging a single 2 mm depth profile, or A-line, took 1.2 seconds, resulting in a three-minute imaging time for a single cross-section. The lack of speed made OCT susceptible to motion artifacts, detrimental to clinical applications. This prompted the development of high-speed OCT systems for clinical applications.

Around 2000, OCT technology reached an important milestone with the introduction of Fourier-domain (FD) OCT. These systems no longer required reference mirror translation to capture each A-line. Instead, an A-line could be reconstructed by sampling the interference fringe in time or space and performing Fourier transforms. Systems that employed a linearly chirped laser source and a high-throughput single-channel digitizer were termed swept-source (SS-)OCT, while those that employed a low coherence source and a spatially dispersive element with a high-speed line-scan camera were termed spectral-domain (SD-) OCT. Furthermore, FD-OCT systems were shown to have more than 20 dB sensitivity benefit over the traditional, time-domain (TD-) OCT given typical and identical imaging conditions. Wojtkowski et al. developed an SD-OCT system and demonstrated volumetric imaging of the human retina at dimensions of 10 (slow axis) by 2048 (fast axis) by 1024 (depth sampling) in 1.3 seconds, which was about a hundred times faster than the TD-OCT systems [12]. By 2005, FD-OCT was firmly established as superior to TD-OCT, and almost all technology development focused on the FD-OCT.

For applications where greater than 2 mm axial sample motion was expected, SS-OCT became the preferred system. A non-mechanical means of optical filtering resulted in rapid sources with cm to km coherence length. Between 2010 and 2020, the source A-line rate increased almost 1000-fold from 10 kHz to 10 MHz. This meant volumetric imaging of 1000 px by 1000 px by 1000 px became possible at 10 frames per second. This capability motivated several hardware groups to develop surgical-grade OCT systems for intraoperative guidance. Functional extensions of OCT, such as angiography and polarization-sensitive (PS-) OCT, could provide unique label-free tissue contrasts, helping surgeons identify tissue of interest with less effort. The surgical time would be reduced, and patient comorbidities and complications would decrease. However, it became obvious that bringing volumetric tomographic imaging capability to a surgical environment requires more than a high-speed laser source.

1.3 Technical Challenges of Surgical OCT Systems

OCT-integrated surgical microscopes exist. In ophthalmology, surgeons can use the intraoperative OCT (iOCT) to monitor the surgical fields and adapt techniques depending on the feedback [13]. These systems can display a two-dimensional cross-sectional image of the field at 20,000 - 100,000 A-lines per second with 5-7 μm axial resolution. However, since they cannot display the full three-dimensional volumetric tomogram, the field of view is limited for continuous surgical guidance. As a result, the surgery may be lengthened, leading to additional complications.

The surgical OCT systems described in this dissertation are different from the iOCT systems, and satisfy the following imaging requirements:

1. Large field of view (FOV): defined as larger than 2 cm by 2 cm.
2. Long imaging range: defined as longer than 3 cm to accommodate dynamic sample motions.
3. Video-rate streaming: defined as more than 30 frames-per-second (fps) to not interrupt the linear surgical flow.
4. Micrometer resolution: anywhere between 10 μm and 100 μm depending on the target nerves.
5. Volumetric information content: defined as three-dimensional tomograms instead of two-dimensional.
6. Compatible with endoscopic camera: motivated by the increased adoption of minimally invasive procedures. This implies bulky scanners cannot be used and imaging approach must be compatible with a 2D imaging sensor.

Currently, OCT systems that simultaneously satisfy all five criteria do not exist. As discussed below, simply scaling existing OCT platforms results in multiple non-trivial technical bottlenecks, which call for alternative approaches.

1.3.1 System Sensitivity Reduction

There are two mechanisms of sensitivity reduction in surgical OCT systems: (1) increased system speed and (2) increased imaging field. OCT can achieve shot-noise-limited sensitivity which is expressed as

$$\Sigma_{shot} = -10log_{10}(\frac{\eta P_0}{h\nu f_A}) \tag{1.1}$$

where η is the detector quantum conversion efficiency, P_0 is the average power incident on the sample, h is the Planck's constant, ν is the optical frequency of the center wavelength and f_A is the source A-line rate. This shows that the system's sensitivity decreases as the imaging speed increases. Compared to a 10 kHz system, a 10 MHz system would suffer a 30 dB sensitivity penalty if other parameters are constant.

For surgical applications, the sample location dynamically changes across a few centimeters of depth. This requires a loosely focused beam to achieve a long depth of focus. In high-resolution OCT imaging, the lateral resolution in air is approximately 10 μm. For surgical applications, increased lateral resolution around 80 μm in the air is desired to realize the depth of focus (DOF) of 1 cm in tissue (the larger the beam spot size, the longer the DOF and vice versa). However, an eight-fold increase in beam spot size means a sixty-fourth reduction of the optical power delivered per area. Thus, the sensitivity suffers by about 18 dB. Therefore, a surgical OCT system takes about 48 dB sensitivity penalty compared to a standard, research-grade OCT system due to the spatiotemporal distribution of photons.

1.3.2 Data Acquisition Electronics Bottleneck

In SS-OCT, the RF bandwidth requirement can be expressed as

$$f_{RF} = 2\pi\frac{\Delta\lambda\Delta z}{\lambda_c^2}f_A \tag{1.2}$$

where $\Delta\lambda$ and λ_c are the source bandwidth and center wavelength, respectively, Δz is the imaging range, and f_A is the A-line rate. To meet the Nyquist criteria, the requisite digitization rate is $f_{digitization} = 2 \times f_{RF}$. For a conservative source with 50 nm optical bandwidth

at 1500 nm center wavelength and 10 kHz A-line rate, imaging 2 mm depth requires 2.8 MHz bandwidth and 5.6 MSamples/second digitization rate. For surgical OCT systems that require a 20 times longer imaging range and 1000 times higher speed, the requisite RF bandwidth is 56 GHz, and the digitization rate is 112 GSamples/second. This is about an order of magnitude faster than the fastest digitizer on the market.

In addition to the RF bandwidth requirement, there is the fundamental issue of data throughput. Suppose 1000 px (x-dimension) by 1000 px (y-dimension) by 10000 px (z-dimension) volumes can be captured at 30 fps. Assuming each pixel has a 2-byte digitization depth, the required data throughput is 600 GB/s. This is beyond the currently achievable streaming rate and an incremental innovation of data bus is unlikely to meet this specification.

1.3.3 Beam Scanning Requirement

A systematic review found that the average residence case volumes for minimally invasive surgery (MIS) increased from 270 to 368 (36 %) over the 16-year period since 2003 [14]. MIS is steadily gaining popularity due to faster patient recovery time and reduced surgical complications. It would be ideal for surgical OCT systems to be compatible with endoscopic applications.

Typically, volumetric tomograms are acquired by laterally scanning the beam across the sample. For open surgery with a static surgical field, the scanner size is not the biggest problem. Combining a galvanometer scanner sweeping around 100 Hz and a resonant scanner sweeping around 10 kHz can achieve video-rate image capture as long as a high-speed digitizer with sufficient bandwidth is available. However, the scanning requirement becomes prohibitive for MIS, where surgeons employ front-facing endoscopic probes with a centimeter diameter to perform complex procedures. The size of these probes prohibits the use of bulky, high-speed scanners.

Some groups have explored scan-free approaches to OCT to overcome these barriers. Borycki et al. demonstrated a full-field swept-source OCT (FF-SS-OCT) with a camera running at

15.9k fps where each frame containing discrete wavelength information [15]. They demonstrated that coherent cross-talk could be eliminated with computational means. Though appealing, this same method would not scale for endoscopic applications. The fastest endoscopic camera on the market runs at 120 fps, which is a few orders of magnitude slower. At this rate, the sample motion will de-correlate the phase relationship between frames, resulting in unusable fringes. Moreover, cameras are much slower devices compared to single-channel digitizers. Overcoming the data throughput bottleneck will be even more challenging for cameras.

1.3.4 Volumetric Data Visualization

Surgeons are accustomed to seeing two-dimensional images. Therefore, streaming raw, volumetric datasets at video rate would likely be more distracting than useful. This is a data visualization problem. Suppose the goal of the surgical OCT system is to help surgeons visualize some structure of interest. Then, an ideal display highlights only the relevant features and provides the volumetric information available in the raw dataset. This is an open-ended problem and will likely have multiple viable solutions. The challenge is to determine an algorithm that maximally utilizes the volumetric information capture of OCT, while showing camera-like images.

1.3.5 System Hardware Complexity

The last technical challenge is managing the system complexity. It is possible to implement a brute-force method to increase the FOV to meet the surgical requirement or use an extremely expensive, custom-made digitizer to achieve a decently long imaging range. However, such a solution will face challenges with adaptation and, eventually, commercialization. As the OCT field focuses on application-specific system development, managing hardware complexity will be critical. This requires knowing the hard boundary conditions. In the case of surgical OCT, the problem outlined in section 1.3.4 serves as a hard boundary condition - it would be extremely challenging to convince surgeons to forgo conventional ways of looking at the surgical field. Based on this knowledge, system hardware complexity could be reduced. The

other important consideration is the fast-evolving field of integrated photonic technology. There have been exciting advances in chip-based OCT technology that can substantially miniaturize the system and eventually reduce cost via mass production. Thus, the hardware development should aim towards minimizing the complexity given the application-specific boundary condition and, at the same time, consider the manufacturability of the technology, should the approach work.

1.4 Thesis Organization

The goal of this work was to develop a novel surgical OCT system for intraoperative nerve identification, which achieves volumetric information capture at camera-like data throughput. In Chapter 2, the fundamental theory of OCT is presented. Only the relevant theories are covered to contextualize this work's theoretical and technological advancement. Chapter 3 presents strategies to overcome sensitivity reduction in surgical OCT systems. It comprises theoretical and experimental works demonstrating the advantages and disadvantages of the proposed approach. Chapter 4 is dedicated to the novel surgical OCT system for intraoperative nerve identification. The working principle of the novel system is presented, and preliminary imaging results are shown. Chapter 5 presents a possible future surgical application of nerve imaging in vagus nerve stimulator placement. Though the study was conducted with a conventional SS-OCT system, the novel surgical OCT system can provide real-time feedback on the stimulator placement. The dissertation concludes with possible future research areas given the advances made in this work. Overall, this work contributes to the progress toward realizing a volumetric, multi-cubic-centimeter field-of-view endoscopic camera-compatible OCT system for intraoperative nerve identification.

Chapter 2

Theory of OCT

Sir Isaac Newton attempted to explain an alternating dark and light fringe pattern forming on a curved glass plate placed above a flat glass plate in 1666. He proposed that every refractive event caused light to be in a different state. The transmitted power is modulated at each reflective element, leading to the radial fringe pattern [16]. Of course, the corpuscular nature of light alone could not fully explain this behavior. Now, we know that light behaves like a wave at the macroscopic scale and that the rings Newton had observed are due to interference between waves reflected at the glass-air boundary and those reflected at the air-glass boundary with increasing path length along the curve. These waves interfered as long as they remained correlated across space and time. This property of light is called optical coherence and is a function of the optical bandwidth. The larger the optical bandwidth, the shorter the coherence time or length, and vice versa. In 1881, Albert Abraham Michelson built the first interferometric device to exploit this property of light. The apparatus allowed him to measure the speed of light with unprecedented precision (within 0.05% of the currently accepted value), providing evidence against the then-prevalent aether theory [17]. The same physical principle applies to OCT, except it measures the backscattered sample field instead of the speed of light. This chapter aims to provide the essential theory of OCT upon which the thesis work was built. In particular, the image-forming mechanism, sensitivity, and recent attempt to overcome the data acquisition bottleneck are presented.

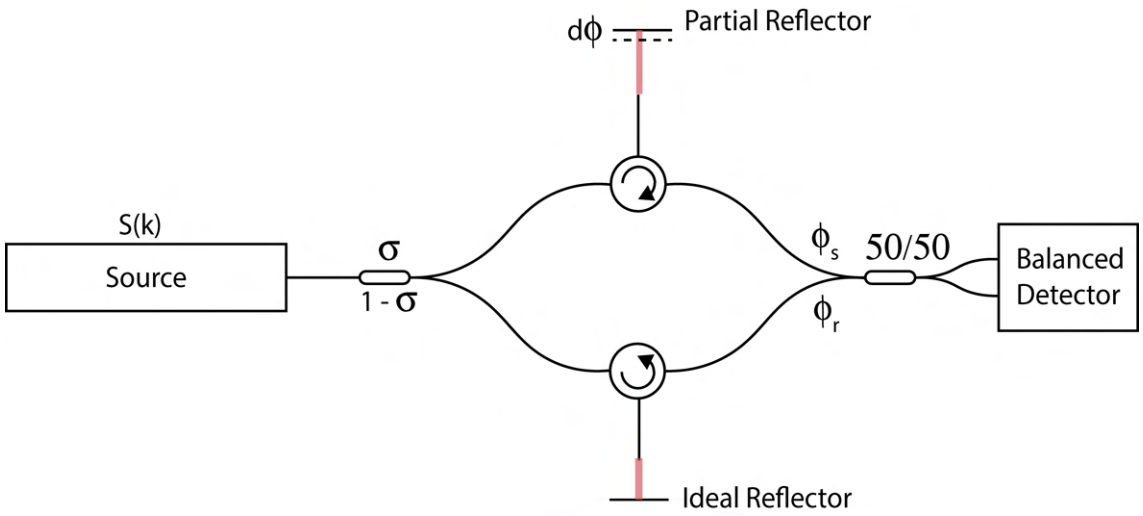

Figure 2.1: Simple MZI-based OCT system setup. The monochromatic light is split between the sample path and the reference path of the MZI. The sample arm accumulates ϕ_s total phase and contains a lossy element. The reference arm accumulates ϕ_r total phase. The two fields combine, and the two MZI outputs are coupled into the balanced detector. .

2.1 Image Formation in OCT

OCT can be built with a Michelson interferometer or Mach-Zehnder interferometer (MZI). Throughout the thesis, MZI-based OCT systems are concerned, though the same image formation principle applies to Michelson interferometer-based systems. In OCT, the spectral content of the source defines imaging properties such as the coherence length and axial resolution. Consider an idealized, lossless, dispersion-less MZI in Fig. 2.1. The source field is split between the sample arm and reference arm via the directional coupler. The optical fiber guides the light towards the circulator. The circulator directs the light to the sample and collects the backscattered light. The sample field and the reference field are superposed in the mixing coupler and the resultant field is detected. Assuming linearity, the field transfer matrix can describe the action of the splitting coupler, path mismatch, and the combining coupler on the linearly polarized source field

$$E_{source} = \sqrt{S(k)}e^{-i\Phi(k)} \tag{2.1}$$

where $S(k)$ is the power spectral density and $\Phi(k)$ is the wavelength-dependent source phase jitters. The electric field incident on the balanced detector is found by cascading each transfer matrix corresponding to relevant component in the interferometer

$$\begin{bmatrix} E_+ \\ E_- \end{bmatrix} = \begin{bmatrix} \frac{1}{\sqrt{2}} & \frac{1}{\sqrt{2}} \\ \frac{1}{\sqrt{2}} & -\frac{1}{\sqrt{2}} \end{bmatrix} \begin{bmatrix} \sqrt{r(z)}e^{i\phi_s} & 0 \\ 0 & e^{i\phi_r} \end{bmatrix} \begin{bmatrix} \sqrt{\sigma} & \sqrt{1-\sigma} \\ \sqrt{1-\sigma} & -\sqrt{\sigma} \end{bmatrix} \begin{bmatrix} E_{source} \\ 0 \end{bmatrix} \tag{2.2}$$

where σ is the sample power splitting ratio, $\phi_{s/r} = kl_{s/r}$ is the total phase accumulated in the sample path and the reference path, respectively, and $r(z)$ is the reflectivity of the partial mirror relative to the position of the reference arm mirror. The total phase difference between ϕ_s and ϕ_r is denoted by $d\phi = kz = k\frac{l_s - l_r}{2}$. The electric fields in each port of the balanced detector are

$$E_{+/-} = \frac{E_{source}}{\sqrt{2}}[\sqrt{r(z)\sigma}e^{i\phi_s} \pm \sqrt{1-\sigma}e^{i\phi_r}] \tag{2.3}$$

The balanced detector performs the difference operation upon photodetection

$$I_{BD} = \frac{\eta q}{h\nu}[< |E_+|^2 >_T - < |E_-|^2 >_T] \tag{2.4}$$

where, q is the unit charge, η is the detector quantum efficiency, $h\nu$ is the photon energy, and $<>_T$ is the time-averaging over the observation time. The resultant photocurrent is

$$I_{BD} = \frac{\eta q}{h\nu} < S(k)\sqrt{r(z)\sigma(1-\sigma)}(e^{i2kz} + e^{-i2kz}) >_T \tag{2.5}$$

Note the DC terms cancel and the AC terms are doubled in the field. Eq. 2.5 is clearly a function of k and z. In TD-OCT all spectral components are integrated within the observation time, whereas in SS-OCT each spectral component is resolved within the observation time. The critical image-forming factor is $S(k)$. Consider the TD-OCT system with a monochromatic source

$$S(k) = A(k)\delta(k - k_c) \tag{2.6}$$

where $A(k)$ is the amplitude and k_c is the wavenumber corresponding to the central wavelength. Then,

$$I_{BD}^{monochromatic} = \frac{\eta q}{h\nu}\sqrt{r(z)\sigma(1-\sigma)}\int_{-\infty}^{\infty} A(k)\delta(k-k_c)[e^{i2kz}+e^{-i2kz}]dk \tag{2.7}$$

$$= 2\frac{\eta q}{h\nu}\sqrt{r(z)\sigma(1-\sigma)}A(k_c)cos(2k_c z) \tag{2.8}$$

For a single partial reflector at z, the signal amplitude is determined by the cosine modulation. In this case, a DC signal would be measured at $z = 0$. If $r(z) = 1\forall z$, and the photocurrent is plotted as a function of z, the resulting plot would look like the cosine modulation that extends from $-\infty$ to ∞. In other words, a monochromatic source is unable to localize the point of back-reflection.

Now consider a TD-OCT with a Gaussian source of the form

$$S(k) = \frac{1}{\sqrt{2\pi\sigma_k^2}}exp[-\frac{(k-k_c)^2}{2\sigma_k^2}] \tag{2.9}$$

Substituting this into the photocurrent equation yields

$$I_{BD}^{Gaussian} = \frac{\eta q}{h\nu}\sqrt{\frac{r(z)\sigma(1-\sigma)}{2\pi\sigma_k^2}}\int_{-\infty}^{\infty} exp[-\frac{(k-k_c)^2}{2\sigma_k^2}][e^{i2kz}+e^{-i2kz}]dk \tag{2.10}$$

After massaging and using the integral look-up table, the photocurrent takes on a nice closed form solution

$$I_{BD}^{Gaussian} = 2\frac{\eta q}{h\nu}\sqrt{r(z)\sigma(1-\sigma)}exp[-2z^2\sigma_k^2]cos(2k_c z) \tag{2.11}$$

Note that this equation differs from Eq. 2.8 in that the amplitude is replaced by a dampening factor proportional to the σ_k^2, or the source spectral bandwidth. **Thus, the spectral width of the source determines the degree of localization of the point reflector. That is the source bandwidth determines the axial resolution**. This interpretation is true also for FD-OCT. Here, Eq. 2.5 is a function of k

$$I_{BD}[k] = 2\frac{\eta q}{h\nu}S[k]\sqrt{r(z)\sigma(1-\sigma)}cos(2kz) \tag{2.12}$$

where [] denotes discrete sampling. Taking the discrete Fourier transform yields

$$FT\{I_{BD}[k]\} = I_{BD}[z] = 2\frac{\eta q}{h\nu}\sqrt{r(z)\sigma(1-\sigma)}[FT\{S[k]\} * FT\{cos(2kz)\}] \tag{2.13}$$

The Fourier transform of a cosine function is a point in the positive and negative frequency located at z. The Fourier transform of $S[k]$ determines the spatial extent to which this point can be localized. For a monochromatic source, the Fourier transform results in a square function extending between $-\infty$ and ∞. This is the case of Eq 2.8 in TD-OCT. For a Gaussian source, the Fourier transform of $S[k]$ will be another Gaussian function with a spread that is the inverse of the bandwidth. This is a manifestation of the momentum-position uncertainty principle.

$I_{BD}(z)$ contains depth-resolved sample information. To generate a volumetric tomogram, the sample illumination beam is scanned in the lateral dimensions. In the low-NA regime, which is of interest in surgical OCT systems, the axial resolution is entirely determined by the source bandwidth, as discussed above, and the lateral resolution is entirely determined by the objective lens spot size [18]. The FWHM power computed from focused Gaussian beam yields

$$\delta x = 0.37\frac{\lambda_c}{NA} \tag{2.14}$$

with the depth of focus (DOF) given by $2z_R = 2\pi\frac{(\delta_x/2)^2}{\lambda_c}$, where NA is the objective numerical aperture, and z_R is the Rayleigh range [19]. This determines the number of lateral samples required to capture the complete information content. For example, imaging a 1 cm by 1 cm sample field at 10 μm resolution requires 2000 pixels by 2000 pixels to meet the Nyquist criteria. Depending on the size of the biological feature to image, however, this criteria can be loosened.

Optically, TD-OCT, and FD-OCT have identical image-forming principles. However, the mechanical and electronic requirements differ between the two. First, TD-OCT captures the

A-line by translating the reference mirror as a function of time

$$I_{BD}(t) \propto cos(2k_c z(t)) = cos(2k_c(z_0 + v_{mirror}t)) \tag{2.15}$$

where z_0 is the depth offset before scanning and v_{mirror} is the mirror translation speed. Thus, the A-line rate is limited by the mechanical translation speed. In SS-OCT, the A-line is captured by sweeping the laser source

$$I_{BD}(t) \propto cos(2k(t)z) = cos(2(k_0 + \kappa t)z) \tag{2.16}$$

where k_0 is the initial wavenumber and κ is the tuning rate. Since the source can be tuned much faster than mirror translation, $\kappa >> v_{mirror}$. Quantitatively, the RF bandwidth required to generate an A-line for TD-OCT and SS-OCT is

$$f_{RF}^{TD} = 2k_c v_{mirror} = 4\pi \frac{v_{mirror}}{\lambda_c} = 4\pi \frac{f_A z}{\lambda_c} \tag{2.17}$$

and

$$f_{RF}^{SS} = 2\kappa z = 4\pi \frac{\Delta\lambda}{\lambda_c} \frac{f_A z}{\lambda_c} = \frac{\Delta\lambda}{\lambda_c} f_{RF}^{TD} \tag{2.18}$$

respectively. **Therefore, for identical imaging conditions, the RF bandwidth requirement for SS-OCT is less than TD-OCT by the ratio of the source bandwidth to its center wavelength, which is usually less than 1/10. However, the advantage of TD-OCT is that each depth measurement is independent of the other, whereas SS-OCT requires phase stability during the source sweep time.** Again, meeting the Nyquist theorem requires sampling at twice this RF bandwidth.

2.2 OCT Sensitivity

In OCT, the sensitivity is defined as the sample reflectivity that gives a signal-to-noise ratio (SNR) of one. Consider SS-OCT with a dual-balanced detector. SS-OCT provides a few tens of dB sensitivity benefits compared to TD-OCT, but the definition and the physical

principle remain identical [20]. The signal is the mean-squared of Eq. 2.5

$$< I_{BD}^2(t) >_T = \left(\frac{\eta q}{h\nu}\right)^2 < 4\sqrt{p_s p_r} cos(k(t)z) >_T^2 = 8\left(\frac{\eta q}{h\nu}\right)^2 p_s p_r \tag{2.19}$$

where $p_s = \frac{1}{2} r P_0 = \frac{1}{2} r\sigma < S(k) >_T$ and $p_r = \frac{1}{2} P_r = \frac{1}{2}(1-\sigma) < S(k) >_T$, where r is the sample reflectivity and P_0 is the average power incident on the sample [21][22][23]. The noise power comprises electronic noise and optical noise

$$< I_N^2(t) >_T = \left(\frac{i_{qn}^2}{G^2} + \frac{i_{ex}^2}{G^2} + i_{th}^2 + 4\frac{\eta q^2}{h\nu}(p_r + p_s) + \left(\frac{\eta q}{h\nu}\right)^2 RIN\left(2\zeta(p_r^2 + p_s^2) + 4p_r p_s\right)\right) BW \tag{2.20}$$

where i_{qn} is the quantization noise, i_{ex} is the DAQ digitization noise, G is the op-amp gain, i_{th}^2 is the thermal noise, RIN is the source relative intensity noise, ζ is the balancing efficiency, and BW is the detector electronic bandwidth. The first two terms can be suppressed with sufficient gain. The third term can be made negligible with sufficient optical power. The fourth term is classically (as opposed to quantum mechanically, to be described in Chapter 3) determined shot noise, and the fifth term is the beat term due to the source RIN. By definition,

$$SNR = \frac{< I_{BD}^2(t) >_T}{< I_N^2(t) >_T} \tag{2.21}$$

The sensitivity advantage of OCT becomes obvious when we consider a shot-noise-limited SNR, where the fourth term dominates.

$$SNR_{shot} \approx \frac{2\eta p_s p_r}{h\nu(p_s + p_r)BW} \approx \frac{2\eta p_s}{h\nu BW} \tag{2.22}$$

The reference shot noise dominates over the much smaller sample shot noise and the coherent mixing of the sample field and the reference field improves SNR indefinitely (in theory) as a function of the sample illumination power at a fixed detector bandwidth. Then, the shot-noise-limited sensitivity is

$$\Sigma_{shot} = -10 log_{10}\left(\frac{\eta P_0}{h\nu BW}\right) \tag{2.23}$$

The dimensional analysis shows that this is simply an average photon number detected during the observation time. In practice, achieving this limit becomes challenging with

noisy sources since the RIN power grows quadratically and overtakes the shot noise power. Also, for fiber-based interferometers, Rayleigh scattering, and component reflections lead to unwanted backscattering, increasing shot noise. **If it is possible to achieve a true shot-noise limit, then the imaging system has a single-photon sensitivity. The SNR improves linearly with the number of sample photons.**

For surgical systems, the sensitivity is reduced due to (1) an increase in BW and (2) a quadratic decrease in P_0 per unit area. Suppose that a non-surgical system had a baseline sensitivity of -120 dB with a 10 kHz source and 10 μm spot size. Suppose that this same system is converted to a surgical system with a 10 MHz source and 80 μm spot size for increased depth of focus. According to Eq. 2.23, the new system suffers a 30 dB penalty from the speed and an 18 dB penalty from a 64-fold increase in the total area of the illumination beam. Thus, the surgical system will have -72 dB sensitivity. For clinical-grade systems, at least -90 dB sensitivity is desired. In Chapter 3, high-power amplification strategies are presented.

2.3 Polarization-sensitive (PS-) OCT

Section 2.1 showed that OCT contrast is based on the depth-dependent sample reflectivity. An additional contrast mechanism is possible for samples that exhibit macroscopic organization. The structural anisotropy leads to birefringence, which can be quantitatively measured by analyzing the change in the input beam polarization state. The two orthogonal polarization states see different sample refractive indices oriented parallel and perpendicular to the sample optic axis (OA), resulting in a differential delay proportional to $\Delta n = n_x - n_y$. OCT systems that measure this sample property are called polarization-sensitive (PS-) OCT. In general, there are three formalisms to PS-OCT: (1) Jones, (2) Stokes, and (3) Meuller. This dissertation omits the discussion of the last formalism, given the challenges of implementing the enabling hardware. Regardless of which formalism to use, PS-OCT aims to infer the depth-dependent sample birefringence and OA orientation.

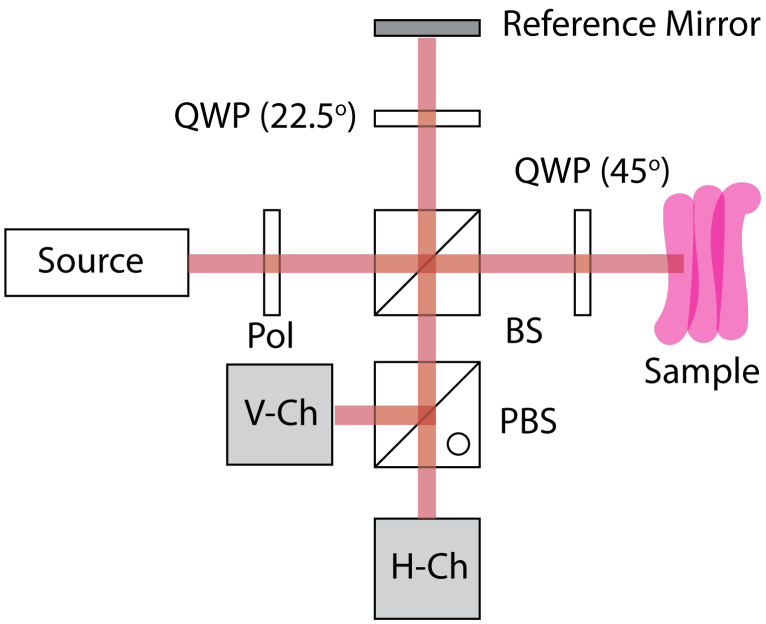

Figure 2.2: Bulk optics PS-OCT setup. Pol: Polarizer; QWP: Quarter-waveplate; BS; Beam splitter; PBS: Polarization Beam Splitter. .

The first implementation of PS-OCT was reported by Hee et al [24]. They used a bulk-optics TD-OCT setup based on the Michelson interferometer to measure sample birefringence. Later, Hitzenberger et al. used a phase-resolved TD-OCT setup to extract sample OA orientation [25]. Both groups employed Jones formalism, where the incident beam is described by a complex vector, and the optical components and the sample are described by complex Jones matrices. The general PS-OCT setup is shown in Fig. 2.2. The source beam is linearly polarized by the polarizer and is split between the reference and sample paths by the 50-50 beam splitter. The field at either path is

$$E_{inc} = \frac{E(k)e^{ikz}}{\sqrt{2}} \begin{bmatrix} 1 \\ 0 \end{bmatrix}. \tag{2.24}$$

A generalized Jones matrix to describe the action of a linear retarder with relative phase retardation δ and an arbitrary fast axis orientation θ with respect to the laboratory frame's x-axis is given by the similarity transformation of the retarding element

$$\overline{\mathbf{J}}(\delta, \theta) = \overline{\mathbf{R}}(-\theta)\overline{\mathbf{P}}(\delta)\overline{\mathbf{R}}(\theta) \tag{2.25}$$

which yields [26]

$$\overline{\mathbf{J}}(\delta,\theta) = \begin{bmatrix} e^{i\delta}cos^2\theta sin^2\theta & (e^{i\delta}-1)sin\theta cos\theta \\ (e^{i\delta}-1)sin\theta cos\theta & e^{i\delta}sin^2\theta + cos^2\theta \end{bmatrix}. \tag{2.26}$$

Eq. 2.26 also describes the quarter waveplates orientated at 22.5° and 45°. The Jones matrix of a sample located at z with optic axis oriented at θ is modeled as

$$\overline{\mathbf{J}}_s(\Delta n,\theta,z) = e^{ik\overline{n}z}\overline{\mathbf{R}}(-\theta)\begin{bmatrix} e^{ikz\Delta n} & 0 \\ 0 & 1 \end{bmatrix}\overline{\mathbf{R}}(\theta) \tag{2.27}$$

where $\overline{n}$ is the average of the two refractive indices and Δn is the differential phase delay as defined earlier. The sample and reference fields are modeled by cascading the Jones matrices for forward propagation and then cascading the transpose of the same matrices for backward propagation. The interference terms detected by the H- and V-channels are

$$A_H(z) = \frac{S(k)}{2\sqrt{2}}\sqrt{R_s}sin(kz\Delta n)cos[2k(z_R-(z_S+\overline{n}z))-kz\Delta n-2\theta] \tag{2.28}$$

and

$$A_V(z) = \frac{S(k)}{2\sqrt{2}}\sqrt{R_s}cos(kz\Delta n)cos[2k(z_R-(z_S+\overline{n}z))-kz\Delta n] \tag{2.29}$$

where the reference reflectivity is assumed to be unity, R_s is the real sample reflectivity, and $z_{R/S}$ is the reference and sample position, respectively. The depth-dependent phase retardation is obtained by

$$\delta(z) = tan^{-1}\left[\frac{A_H(z)}{A_V(z)}\right] \tag{2.30}$$

and the OA orientation is determined by

$$\theta = \frac{Arg(A_H(z)) - Arg(A_V(z))}{2} \tag{2.31}$$

where Arg stands for "extracting the argument of". Note that this method requires absolute phase and is ill-suited for applications where phase stability is not guaranteed. Stokes formalism can overcome this drawback. While Jones formalism requires measuring field quantities,

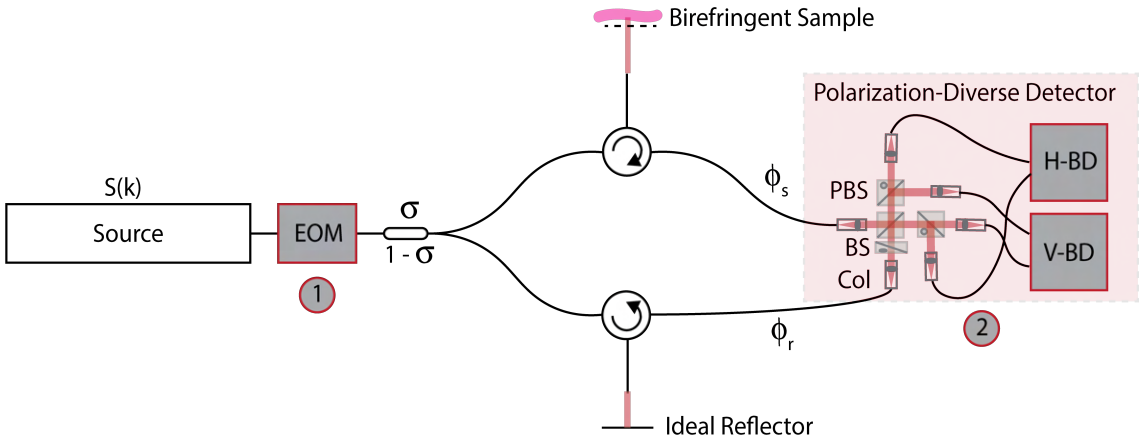

Figure 2.3: Converting an SS-OCT system to a PS-OCT system requires two alterations: (1) Addition of a polarization modulator and (2) Use of a polarization diverse detector. EOM: electro-optic modulator; PBS: polarization beam-splitter; BS: beam-splitter; Col: collimator. The two orthogonal polarization channels help reconstruct sample birefringence. .

Stokes formalism measures irradiance, which is much easier experimentally. Moreover, since all the components can be determined from the relative phase difference between the H- and V- channels, the source need not be phase stable. The Stokes formalism constitutes of four parameters

$$\begin{bmatrix} s_0 \\ s_1 \\ s_2 \\ s_3 \end{bmatrix} = \begin{bmatrix} I_0 \\ I_{0^\circ} - I_{90^\circ} \\ I_{45^\circ} - I_{-45^\circ} \\ I_{RC} - I_{LC} \end{bmatrix}. \tag{2.32}$$

where I_0 is the total irradiance and the subscripts denote irradiance measured with analyzers oriented at 0°, 45°, -45°, and 90° with respect to the laboratory frame. Similarly, the subscripts RC and LC denote the right- and left-circularly polarized irradiance. For a fully polarized light, Jones formalism can be recast to Stokes formalism. PS-OCT systems based on swept source employ Stokes formalism to reconstruct depth-resolve sample birefringence and OA orientation. Fig. 2.3 shows an example setup of such a system.

Compared to the conventional OCT setup (Fig. 2.1), it has two hardware changes. First, the electro-optic modulator (EOM) is added to toggle the input polarization state between linear polarization and circular polarization. This ensures birefringence is measured even if one of

the input states is aligned to the optic axis. Second, the polarization diverse detector is used instead of a single balanced detector. Optical fibers scramble the polarization state of the light propagating inside them. Therefore, a linear polarizer is placed in the reference arm to clean up the reference polarization before mixing with the sample field. The transformation of the source field through the birefringent sample is expressed as

$$\mathbf{E}^q_{\mathbf{out}}[k] = S[k] \cdot \overline{\mathbf{J}}_{\mathbf{B}}[k] \cdot \overline{\mathbf{J}}_{\mathbf{S}}[k] \cdot \overline{\mathbf{J}}_{\mathbf{A}}[k] \cdot \mathbf{E}^q_{\mathbf{in}} \tag{2.33}$$

where $\mathbf{E}^q_{\mathbf{in}}$ is the q-th source field and $\overline{\mathbf{J}}_{\mathbf{A}}$, $\overline{\mathbf{J}}_{\mathbf{S}}$, and $\overline{\mathbf{J}}_{\mathbf{B}}$ are Jones matrices from the source to the sample, double-pass through the sample, and from the sample to the detector, respectively. Vectors are bolded and Matrices are bolded with an overline. The two input states are $\mathbf{E}^1_{\mathbf{in}} = [1, 0]^T$ and $\mathbf{E}^2_{\mathbf{in}} = \frac{1}{\sqrt{2}}[1, -i]^T$. The q-th tomogram can be reconstructed as

$$\mathbf{T}^q[z] = FT\{W[k] \cdot \mathbf{E}^q_{\mathbf{out}}[k]\} \tag{2.34}$$

where $W[k]$ is a windowing function, typically Hanning or Hamming, to enforce periodicity. The Jones formalism can be recast to Stokes formalism with the complex tomogram. Specifically,

$$\mathbf{s}^q[z] = \begin{bmatrix} s^q_I[z] \\ s^q_Q[z] \\ s^q_U[z] \\ s^q_V[z] \end{bmatrix} = \begin{bmatrix} T_x T_x^* + T_y T_y^* \\ T_x T_x^* - T_y T_y^* \\ 2\mathcal{R}\{T_x T_y^*\} \\ -2\mathcal{I}\{T_x T_y^*\} \end{bmatrix} \tag{2.35}$$

where the asterisk denotes the complex conjugate, and $\mathcal{R}$ and $\mathcal{I}$ refer to the real part and the imaginary part, respectively. In practice, the local Stokes vectors are spatially averaged to decrease noise. The Stokes formalism has the advantage that depolarization can be quantified. The depth-resolved degree of polarization uniformity (DOPU) is computed as

$$DOPU[z] = \sum_{q=1}^{2} \frac{\sqrt{(\tilde{s_Q})^2 + (\tilde{s_U})^2 + (\tilde{s_V})^2}}{\tilde{s_I}} \tag{2.36}$$

where the averaged Stokes vectors, $\tilde{s_x} \equiv s_x(x, y, z) * h(x, y, z)$, where $x \in \{I, Q, U, V\}$ and

$h(x, y, z)$ is the average kernel.

The sample's local retardation and optic axis can be found also. For this, the Poincare sphere, a geometrical representation of Stokes parameters, helps visualize the rotation of the Stokes vectors as a function of depth. On the Poincare sphere, the local retardation is the magnitude of Stokes vector rotation between z and $z + \Delta z$, where Δz is the depth offset and the local optic axis is the axis of rotation about which the Stokes vector rotates in Δz. To compute cumulative optic axis, $\mathbf{A}[z]$, and retardation angle, δ, the Stokes vectors are normalized as

$$\mathbf{N}^q[z] = \begin{bmatrix} \frac{\bar{s}_Q^q[z]}{\bar{s}_I^q[z]} \\ \frac{\bar{s}_U^q[z]}{\bar{s}_I^q[z]} \\ \frac{\bar{s}_V^q[z]}{\bar{s}_I^q[z]} \end{bmatrix} \tag{2.37}$$

A unique (up to π) $\mathbf{A}[z]$ that simultaneously rotates the two input states in a single axis are determined from a pair of new orthonormal basis

$$\mathcal{N}^1[z] = \frac{\mathbf{N}^1 + \mathbf{N}^2}{|\mathbf{N}^1 + \mathbf{N}^2|} \tag{2.38}$$

$$\mathcal{N}^2[z] = \frac{\mathbf{N}^1 - 2 \cdot \mathbf{N}^2}{|\mathbf{N}^1 - 2 \cdot \mathbf{N}^2|} \tag{2.39}$$

The $\mathbf{A}[z]$ is computed as

$$\mathbf{A}[z] = \frac{\big(\mathcal{N}^1[z] - \mathcal{N}^1[z + \Delta z]\big) \times \big(\mathcal{N}^2[z] - \mathcal{N}^2[z + \Delta z]\big)}{|\big(\mathcal{N}^1[z] - \mathcal{N}^1[z + \Delta z]\big) \times \big(\mathcal{N}^2[z] - \mathcal{N}^2[z + \Delta z]\big)|} \tag{2.40}$$

The retardation angle is computed as

$$cos(\delta_q) = \frac{[\mathbf{N}^q[z] \times \mathbf{A}[z]] \cdot [\mathbf{N}^q[z + \Delta z] \times \mathbf{A}[z]]}{|\mathbf{N}^q[z] \times \mathbf{A}[z]||\mathbf{N}^q[z + \Delta z] \times \mathbf{A}[z]|} \tag{2.41}$$

The accuracy of the estimate can be increased by taking the intensity and the sines of δ_q. Before closure, it must be emphasized that the OA orientation determined by the PS-OCT method thus far is apparent and not the true OA orientation. Determining the true OA requires solving for the cumulative effect of preceding tissue layers on the measured OA [27].

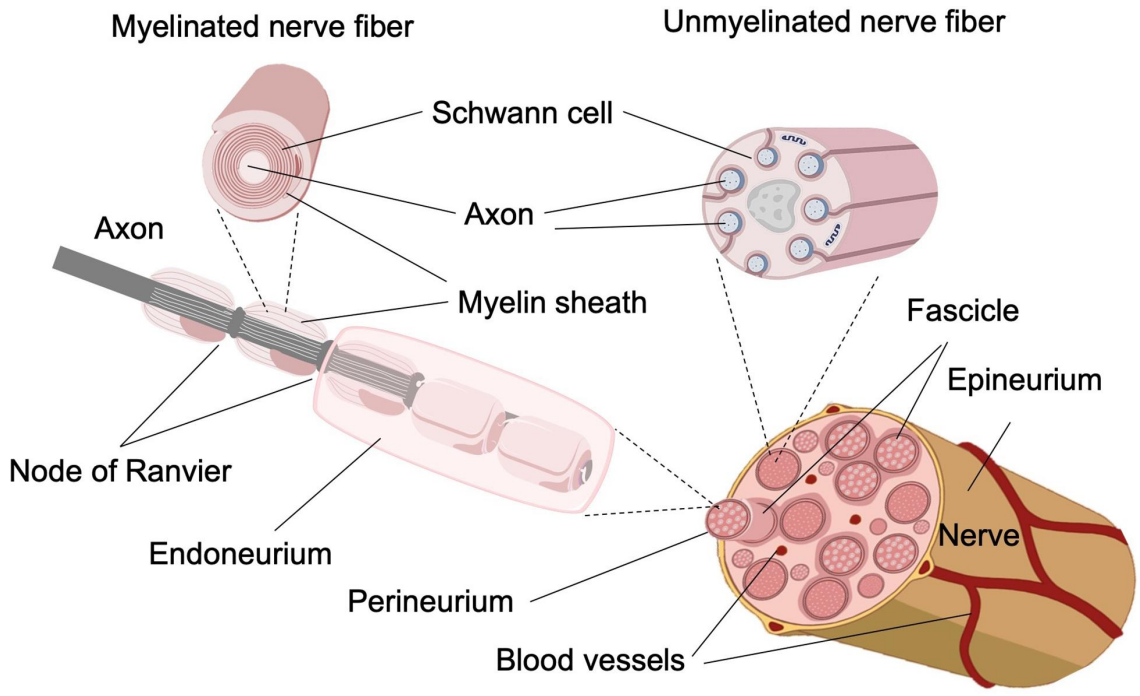

Figure 2.4: Schematic drawing of a peripheral nerve [28]. The myelinated nerve fibers are made of lipid bilayers that contribute to form birefringence, which can be observed with PS-OCT [29][30][31] .

Since the goal of the surgical OCT system is nerve identification and not quantitative nerve characterization, this technical distinction is not critical.

2.3.1 Imaging Nerves with PS-OCT

The myelinated nerves are important imaging targets for surgical OCT systems, which exhibit a unique polarimetric signature. A nerve is composed of four functional components: (1) the fascicle, (2) the perineurium sheath that surrounds and insulates the fascicle, (3) the epineurium, which is a collagenous structure separating fascicles, and (4) adipose tissue that allows fascicles to slide around as needed. The fascicles are composed of a bundle of axons. These structures are illustrated in Fig. 2.4 (adipose tissue not shown). Depending on the nerve type, the fascicles can contain many myelinated axons where a lipid bilayer surrounds the cell body in the radial direction to increase the conduction speed. In myelinated nerves, the macroscopic organization of the lipid leads to a form birefringence; A myelinated nerve acts like a negative uniaxial crystal with the slow axis orientated perpendicular to the

nerve fiber propagation. This means the polarization of light traveling along the slow axis experiences greater phase delay than that traveling along the orthogonal sample axis. The epineurium has an optic axis orientation that is orthogonal to the myelinated nerve, which gives the nerve a unique polarimetric signature different from other birefringent structures like the muscle or cartilage. Fig. 2.5 shows a representative PS-OCT image of a rat sciatic nerve.

2.4 Circular-Ranging (CR-) OCT

In Chapter 1, the prohibitive RF bandwidth requirement to realize a surgical OCT system was discussed. Modern electronics must operate more than an order of magnitude faster to accommodate the speed and long imaging range. CR-OCT method was developed around 2012 to address this problem [33][34]. The key insight was that conventional OCT spends the bandwidth on signal-void regions - it captures space before the sample or region within the sample where the illumination beam has been significantly attenuated. CR-OCT employed a time-stepped frequency comb to subsample the physical information optically. Therefore, the required sampling was preset by the number of combs ($\sim$ 100 sampling points) instead of the sampling set by the source axial resolution ($\sim$ 2000 sampling points). The sample information from the deeper tissue layer would alias into the preset baseband. Fig. 2.6 shows the fundamental working principle. To avoid image wrapping due to the aliased signal, an IQ, or phase diverse, receiver is used to reconstruct real fringe. The result is more than an order of magnitude reduction in the requisite data acquisition electronics bandwidth, enabling data-efficient imaging (see Fig. 2.7 (c) - (e) for sample images).

However, even with CR-OCT meeting the surgical OCT system specifications outlined in Chapter 1 is challenging. Wide-field video-rate imaging has not been achieved. It still captures volumetric sample information and is, therefore, incompatible with endoscopic cameras. Furthermore, CR-OCT requires state-of-the-art sources and capture electronics, making it hard to adopt without further system simplification.

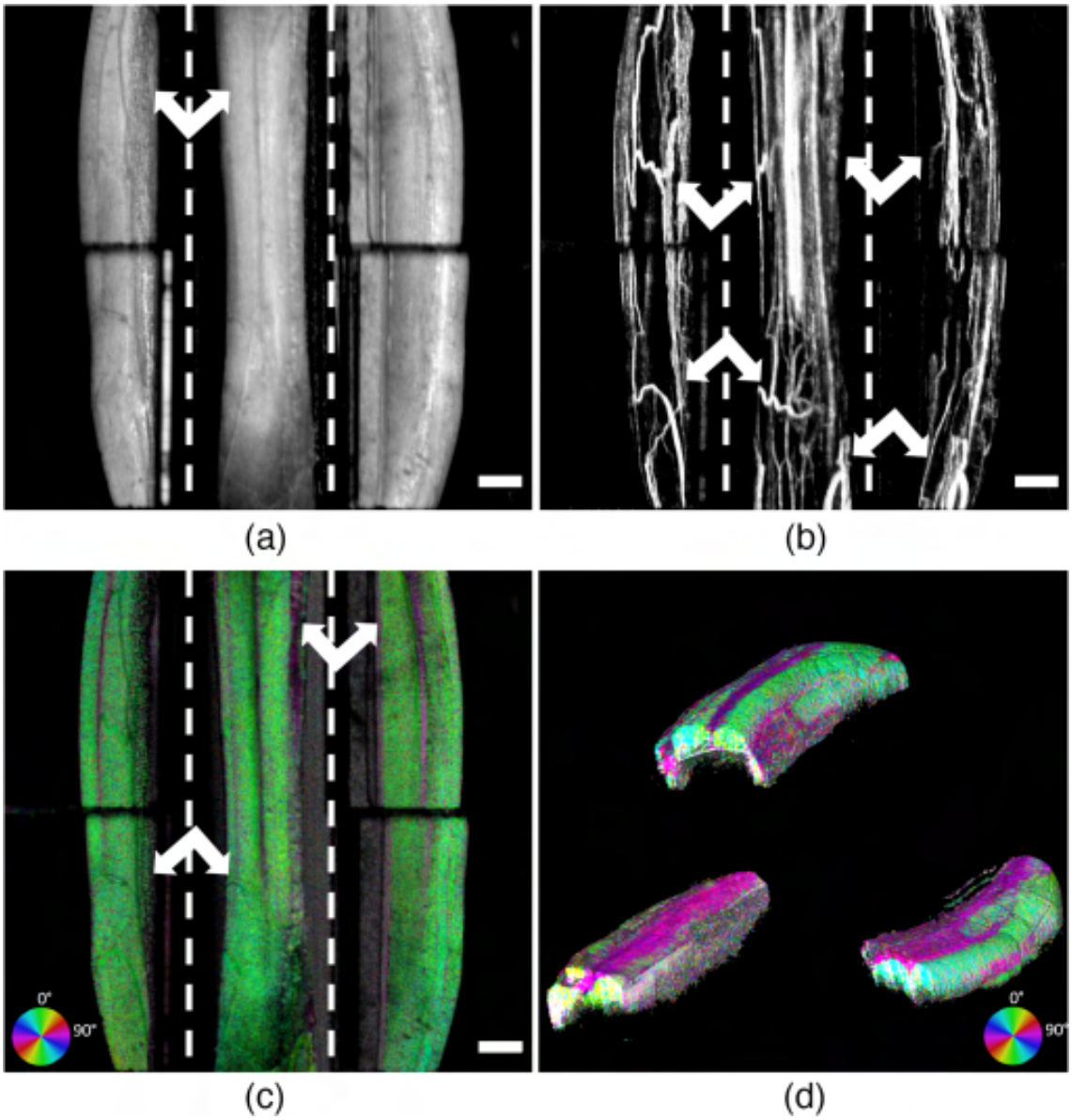

Figure 2.5: A representative PS-OCT image of a rat sciatic nerve in (c) and (d) [32]. (a) is an en-face averaged OCT projection, and (b) is angiographic processing of OCT data. Scale bars: 500 μm. .

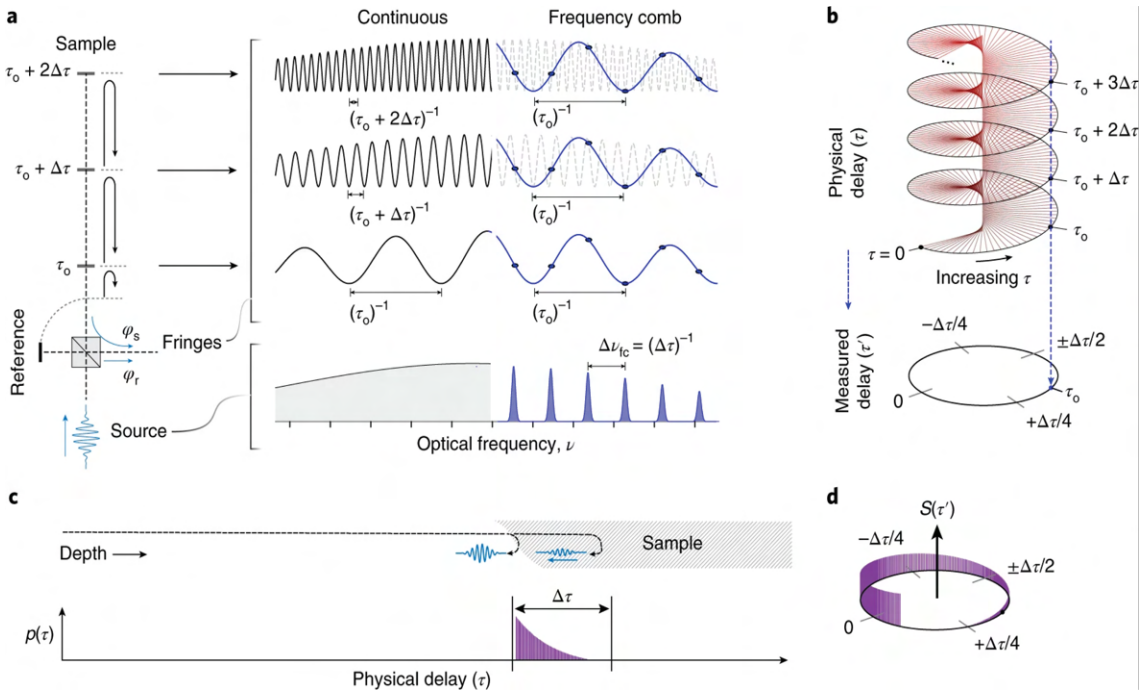

Figure 2.6: Working principle of CR-OCT [34]. (a) comparison between the conventional swept-source and time-stepped frequency comb source given three reflectors. In conventional data capture, the deeper signal information is encoded at a higher frequency. In CR-OCT, the higher frequency is aliased into the RF baseband set by the comb source, $\Delta\nu_{fc}$, corresponding to the delay $\Delta\tau$. (b) Mapping of physical delay to the measured delay demonstrates the principle of optical aliasing. (c) Bandwidth reduction by selective capture of sample space corresponding to $\Delta\tau$. (d) The sample information is mapped to one baseband.

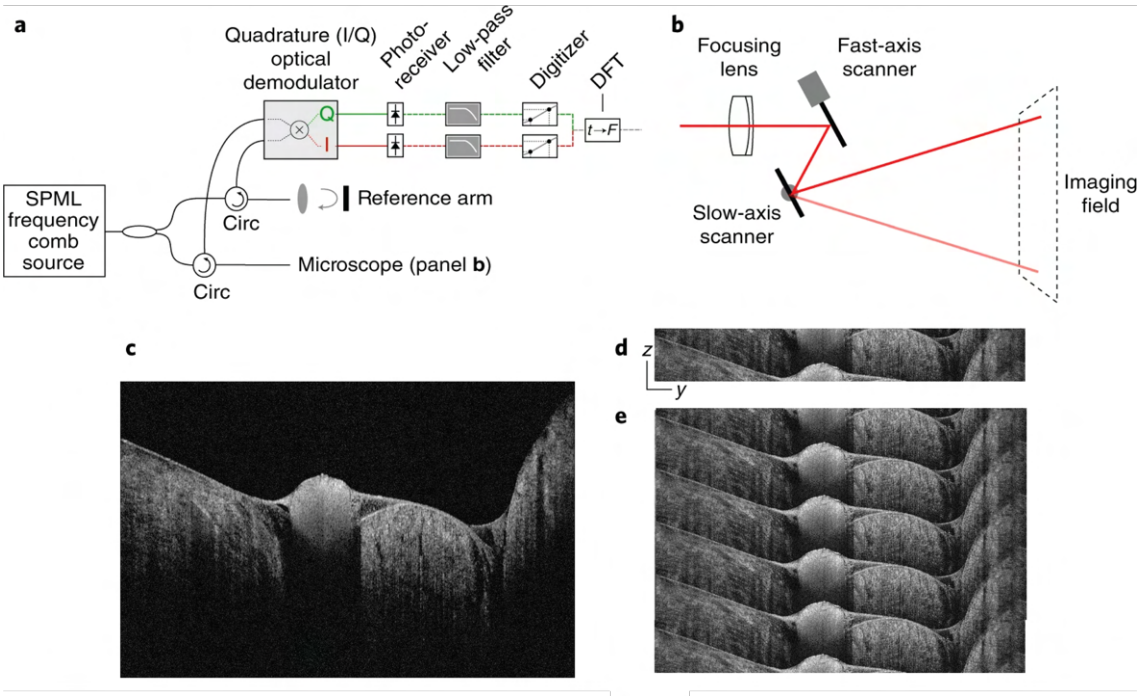

Figure 2.7: Imaging with CR-OCT [34]. CR-OCT system for wide-field imaging and comparison to conventional SS-OCT images. (a) The CR-OCT requires a phase-diverse receiver to demodulate IQ signals. (b) Scanning setup for wide-field imaging. (c) Conventional SS-OCT B-scan image of a chicken nerve embedded in a muscle bed. (d) a single CR-OCT B-scan image from the base band. Note the absence of void voxels. (e) The sample features are made obvious by repeating the baseband image.

Chapter 3

Optical Amplification in OCT

This Chapter provides a comprehensive solution to the system sensitivity challenge associated with a surgical OCT system outlined in section 1.3.1. As evidenced by Eq. 2.23, increasing OCT sensitivity requires consideration of both the sample power and the noise property of the measurement. The Chapter is organized into three compartments. In section 3.1, the basic principle behind optical amplification and amplifier noise is reviewed through a combination of existing literature and an original extension of the derivation given in the literature. In section 3.2, a rigorous yet intuitive OCT SNR model capable of predicting amplifier noise impact on the system sensitivity is developed. The consequence of the predictions given by the theory extends beyond the surgical OCT applications and is briefly discussed. Finally, section 3.3 presents experimental results, including the construction of high-power (>1 Watts average power) amplifiers for surgical OCT systems and interesting non-linear effects in unconventional amplifier placement, which have implications for integrated photonic OCT platforms.

3.1 Principle of Optical Amplification

An amplifier falls into one of two categories: Phase-sensitive amplifiers (PSAs) and phase-insensitive amplifiers (PIAs). An example of PSAs is parametric amplifiers that require precise phase matching to achieve gain. They are difficult to implement in practice, and experiments presented in this work were conducted with PIAs. Therefore, the term amplifiers

refers to PIAs henceforth.

3.1.1 Gain Mechanism of the Phase-insensitive Optical Amplifier

The gain medium is a special material that (1) has atomic energy levels whose transition energy matches with signal bandwidth and (2) can efficiently achieve population inversion. This section reviews the gain mechanism of two popular classes of optical amplifiers. The difference in the material property leads to different amplifier properties, which will be discussed in the context of implementation in OCT systems.

Semiconductor Optical Amplifiers (SOAs)

In SOAs, a semiconductor chip (typically group III-V) with μm (transverse) by mm (longitudinal) dimension is used as the gain medium. The population inversion is achieved by injecting carriers into the conduction band. The energy transition to the valence band corresponds to the optical frequency, increasing photon density. The mean lifetime of this transition is $\sim$ ps, which means SOAs are sensitive to the temporal dynamics of a typical OCT laser source (the fastest A-line rate is on the order of 10 MHz). Thus, field description of wave propagation and gain is necessary to completely describe SOAs' impact on OCT signal [35]:

$$\frac{\partial N}{\partial t} = D\nabla^2 N + \frac{I}{qV} - \frac{N}{\tau_c} - \frac{a(N - N_0)}{\hbar\omega_0}|\mathbf{E}|^2 \tag{3.1}$$

where N is the carrier density (electrons and holes), D is the diffusion coefficient, I is the injection current, q is the electron charge, V is the active volume, τ_c is the spontaneous carrier lifetime, N_0 is the carrier density required for transparency, $\hbar\omega_0$ is the photon energy, and a is the gain coefficient, and $\mathbf{E}$ is the source optical field. The second term is the injection current for population inversion, increasing the carrier density. The third term is the thermal decay leading to the spontaneous photon emission. This contributes to amplifier noise. The last term describes the amplifier gain. The field propagation inside the gain medium is described by the wave equation

$$\nabla^2\mathbf{E} - \frac{(n_b^2 + \chi)}{c^2}\frac{\partial^2\mathbf{E}}{\partial t^2} = 0 \tag{3.2}$$

where c is the speed of light, n_b is the background refractive index as function of the transverse coordinate and χ is the susceptibility that is an implicit function of the carrier density N. A simple model for χ is given as

$$\chi(N) = -\frac{\bar{n}c}{\omega_0}(\alpha + i)a(N - N_0) \tag{3.3}$$

where $\overline{n}$ is the effective mode index and α is the line-width enhancement factor. The Eqs. 3.1, 3.2, and 3.3 completely describe the gain mechanism of SOA.

In OCT, the effects of τ_c and α are observed as a wide gain bandwidth and coherence length reduction, respectively. The 3dB gain bandwidth can be as large as 80 nm, and the wide range of semiconductor choices make SOAs a versatile amplifier for wavelengths ranging from visible to near IR. However, the downside of small τ_c is a low saturation power. For this reason, even the most powerful SOAs can only achieve 100 mW average optical power (tapered SOAs can achieve Watts of power, but are not easily fiber-coupled). Therefore, a higher alternative is preferred for the surgical OCT system.

Erbium-doped Fiber Amplifiers (EDFAs)

EDFAs are one of the best-characterized DOFAs due to their high signal gain and low noise operating in the third telecom window (1500-1610 nm). The Erbium atom has a number of possible electronic energy transitions to access this window. Unlike SOAs, EDFAs are optically pumped to achieve population inversion. In particular, pumping at either 1480 nm or 980 nm enables high gain due to much slower gain dynamics, $\sim$ ms, than that of SOAs. Fig. 3.1 shows the energy diagram and absorption/emission spectra for two types of EDFAs with different network modifiers to isolate Erbium atoms from bunching together. In 3.1 (a), it can be seen that pumping at 980 nm results in a three-level system, whereas the direct, inband pumping at 1480 nm results in a two-level system. Although the latter provides a higher pump to signal conversion efficiency, the rapid ${}^4I_{11/2} - {}^4 I_{13/2}$ transition relative to the ${}^4I_{13/2} - {}^4 I_{15/2}$ transition means a fully inverted, and therefore a very low noise amplifier can be built with 980 nm pumping (noise figure (NF) quantifies the SNR reduction due

to amplifier noise. It is defined as the ratio of the output SNR to the input SNR and the next section explains why this is necessary). Since the state transition is much slower than an OCT A-line rate, the gain dynamics are not relevant, and the power-based propagation model ignoring the phase is sufficient. Assuming a two-state model, the population density equation can be written as

$$\frac{dN_2}{dt} = \sum_k \frac{P_k i_k \sigma_{ak}}{h\nu_k} N_1(r,\phi,z) - \sum_k \frac{P_k i_k \sigma_{ek}}{h\nu_k} N_2(r,\phi,z) - \frac{N_2(r,\phi,z)}{\tau} \tag{3.4}$$

$$N_T(r,\phi,z) = N_1(r,\phi,z) + N_2(r,\phi,z) \tag{3.5}$$

where $P_k(z)$ is the integrated light distribution of the beam over the radial and azimuthal coordinate of the fiber at k^{th} optical mode, i_k is the power normalized optical intensity, $\sigma_{e/(a)}$ is the emission (absoprtion) cross-section, $h\nu$ is the photon energy, and N_T is the total local Erbium ion density. The power propagation can be described by

$$\frac{dP_k}{dz} = u_k \sigma_{ek} \int_0^{2\pi} \int_0^{\infty} i_k(r,\phi) N_2(r,\phi,z) r dr d\phi (P_k(z) + m h\nu_k \Delta\nu_k) \tag{3.6}$$

$$- u_k \sigma_{ak} \int_0^{2\pi} \int_0^{\infty} i_k(r,\phi) N_1(r,\phi,z) r dr d\phi (P_k(z)) \tag{3.7}$$

where $u_k = +1$ for forward propagation and -1 for backward propagating beam and $mh\nu_k\Delta\nu_k$ is the spontaneous emission factor growing along the length of the fiber, corresponding to the thermal decay from N_2 state. $m = 2$ for the two orthogonal polarization modes. Compared to Eqs. 3.1 and 3.2, these equations are different in at least three ways: (1) the gain depends on both the wavelength and fiber length, (2) the fiber can be forward-pumped, backward-pumped, or bi-directionally-pumped, and (3) two cross-sections determine the amplifier conversion efficiency.

The manufacturing flexibility of EDFA is advantageous, especially for doping with other fiber types to achieve high gain. Single-mode EDFA can comfortably achieve $\sim$ 400 mW average power. Beyond this power, parasitic lasing becomes a concern. Dual-clad EDFA codoped with Ytterbium has been developed to increase pump power delivery and conversion by or-

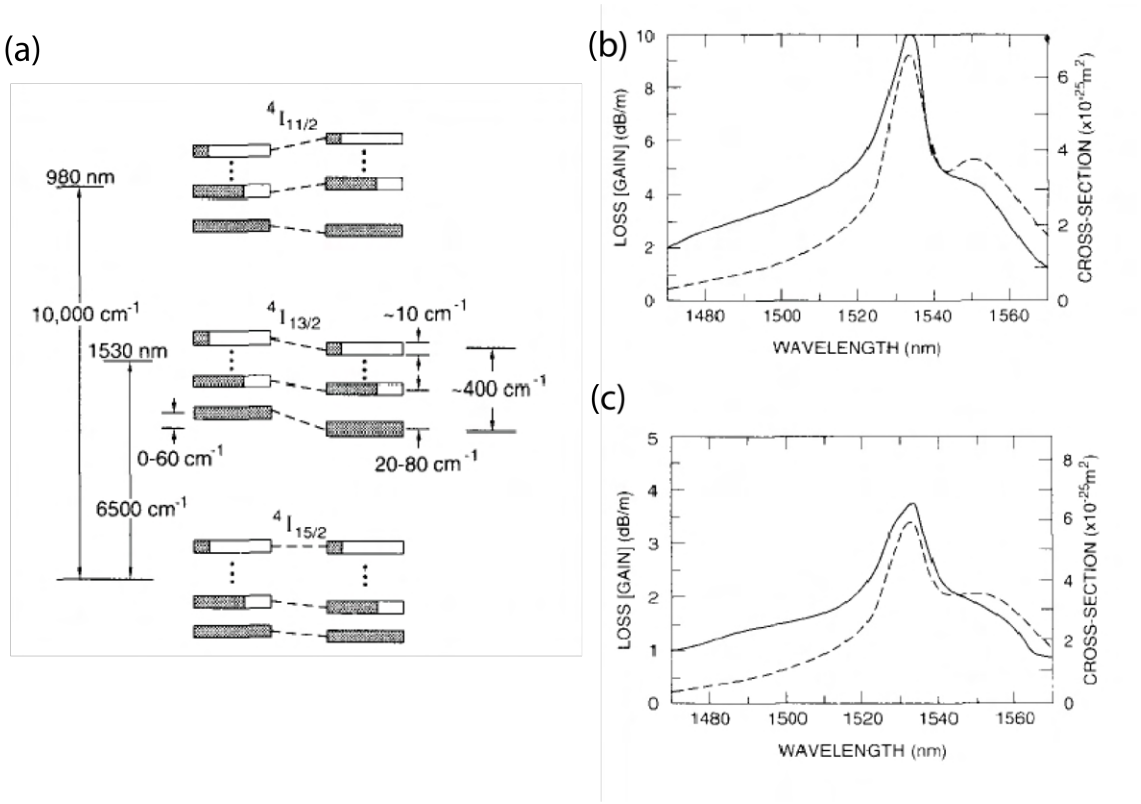

Figure 3.1: (a) Energy level diagram of Er^{3+} in silicate glasses showing homogeneous and inhomogeneous broadening of the Stark-split levels. Shading represents room-temperature Boltzmann-distributed population of each manifold. (b) and (c) are the absorption (solid) and gain (dashed) spectra of Ge:silicate and Al:Ge:silicate amplifier fibers, respectively. The cross-section on the right can be computed from the Ladenburg-Fuchbauer equation [37]. .

ders of magnitude [36]. Rather than the pump and signal co-propagating in the single-mode core, the fiber contains a cladding layer where a multi-moded pump can be coupled. The signal still travels in the core, while high pump power is delivered in the cladding layer. These dual-clad fiber amplifiers can achieve a Watt-level average power.

Table 3.1 summarizes key performance differences between SOAs and DOFAs.

3.1.2 Fundamental Noise Property of Linear Optical Amplifier

In describing gain, the concept of NF was introduced without justifying its need or origin. Can a noiseless amplifier exist? This is impossible; otherwise, any minuscule information

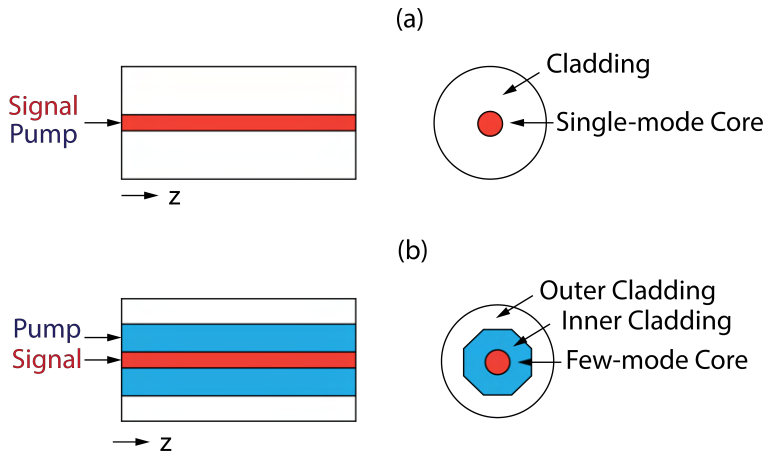

Figure 3.2: Two types of DOFAs. (a) SM-EDFA. The pump beam and the signal beam overlap in the single-mode core. (b) Dual-clad (DC)-EDFA. The multi-mode pump beam propagates in the inner cladding layer while the sample beam propagates in the single to few-mode core. Much higher gain can be realized. .

Table 3.1: Performance difference between SOAs and DOFAs.

Properties	SOA	DOFA	Effect on OCT
Gain Dynamics	$\sim$ ps	$\sim$ ms	Temporal Source Profile
Gain Bandwidth	$>$ 75 nm	$\sim$ 50 nm	Axial Resolution
Gain Saturation Level	Moderate (milli-Watts)	High (Watts)	Sensitivity
Gain Flatness	Moderately Flat	Can be Unflat	Sensitivity
α Factor	Large	Negligible	Coherence Length
Fiber-based	No	Yes	Dispersion
Noise Figure	High (7-10 dB)	Near Limit (3-7 dB)	Sensitivity

content can be retrieved out of noise, clearly not physical. This intuition can be rigorously verified with quantum mechanical principles without referencing the amplifier material properties [38]. Here, proof originally due to H. Heffner shows that an amplifier necessarily adds noise to satisfy Heisenberg's uncertainty principle [39]. An original extension of his proof also predicts how much minimum noise an ideal amplifier must supply to obey the uncertainty principle.

The position-momentum uncertainty relation of a particle can be recast to the photon

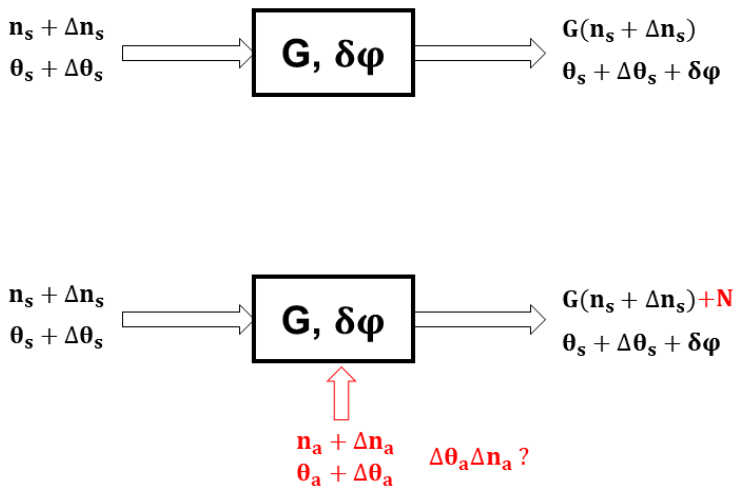

Figure 3.3: A hypothetical linear amplifier. The first row depicts an impossible scenario that violates Heisenberg's uncertainty principle. The second row depicts a physical, ideal amplifier which must have a certain amount of noise injected by the amplification process.

number-phase relation of a photon for all mode m (input mode, output mode, etc).

$$\Delta n_m \Delta\theta_m \geq \frac{1}{2} \tag{3.8}$$

Consider a hypothetical amplifier with gain $G \geq 1$ and path length $\delta\varphi$ as in Fig.3.3. Eq. 3.8 must satisfy both input and output modes. The output uncertainty after the pure signal gain is $\Delta n_{out}\Delta\theta_{out} = G\Delta n_s\Delta\theta_s$. However, this violates Eq. 3.8 since

$$\Delta n_s \Delta\phi_s \geq \frac{1}{2G} \tag{3.9}$$

There must be another mode intrinsic to the amplifier to satisfy Eq. 3.8 at the output.

How much noise should an ideal amplifier add to the shot-noise limited input, i.e., $\Delta n_s\Delta\theta_s = \frac{1}{2}$? The minimum uncertainty state of the output mode is

$$\Delta n_{out}\Delta\theta_{out} = (G\Delta n_s + \Delta n_a)(\Delta\theta_s + \Delta\theta_a) = \frac{1}{2} \tag{3.10}$$

Since the added mode is uncorrelated with the input mode, $G\Delta n_s\Delta\theta_a = \Delta n_a\Delta\theta_s = 0$. Then,

solving for the minimum error of the mode yields

$$\Delta n_a \Delta \theta_a = \frac{G-1}{2} \tag{3.11}$$

Substituting this into Eq. 3.10 yields.

$$\Delta n_{out} \Delta \theta_{out} = G(\frac{1}{2} + \frac{1-\frac{1}{G}}{2}) \tag{3.12}$$

The uncertainty of the output mode is the gain times the uncertainty of the total input modes. In addition to $\frac{1}{2}$ of the input shot-noise, the uncertainty principle demands an additional shot-noise at a sufficiently high gain. **Therefore, an ideal amplifier with high gain necessarily degrades the shot-noise-limited SNR by 3dB**. Quantum mechanics shows that the added noise is due to the vacuum fluctuation. The amplified spontaneous emission (ASE) statistically beats with the amplified signal, degrading the input SNR by the NF. At high gain, NF $= 2n_{sp}$, where $n_{sp} \geq 1$ is the spontaneous emission factor related to the population inversion. This explains why DOFAs can approach the theoretical 3dB NF with high inversion, while SOAs have higher NF due to coupling loss and relatively low inversion.

3.2 Noise Consequence of Optical Amplifier on OCT SNR

According to the theorem derived above, the amplifier must degrade the shot-noise-limited SNR by the NF. Yet, it has been used to improve OCT sensitivity. This paradox calls for revising the existing OCT SNR model to deal with amplifier noise. A rigorous model of noise requires quantum formalism. Fortunately, the quantum optics community has derived the key results relevant to the OCT community [40][41][42][43]. Rather than re-derive them, the essential physics and intuition were extracted to develop an intuitive model to predict the impact of amplifier NF on OCT SNR (rigorous derivations are included in the Appendix A). Throughout this section, the terms *SNR* and *sensitivity* are used interchangeably. To simplify the analysis, a swept source with infinite coherence length is assumed, though the concepts are generalizable to other OFDI and TD OCT systems with a PIA as long.

3.2.1 Revised OCT SNR Model

We start by stating the important quantum principles and operational definitions. The macroscopic light field typically modeled by a clean sinusoidal wave is, in reality, composed of many individual photons. The quantized field obeys the following quantum mechanical principles: (1) its noise statistic is determined by the state the light is in and the type of measurement performed on it, and (2) simultaneous, noise-free measurement of its conjugate variables is prohibited even with an ideal detector, i.e., zero-internal noise and perfect detector quantum efficiency, $\eta = 1$. For OCT, the swept source can be treated as coherent state light and the detection as a quadrature measurement where the optical path length difference between the sample field and the reference field is measured. The relevant conjugate variables for quadrature measurement are the two orthogonal quadrature phase operators, $\hat{X}$ and $\hat{Y}$. We can think of them as the real and the imaginary parts in phase space. For coherent state light, the minimum quadrature quantum noise is

$$(\Delta X)^2 = (\Delta Y)^2 = \frac{1}{4}, \tag{3.13}$$

equivalently called optical shot noise for our purpose. This is the absolute minimum value for the measured shot noise in classical OCT. The SNR limited by this noise is called the standard quantum-limited (SQL) SNR as opposed to the quantum-limited (QL) SNR, which is the SQL SNR degraded by the detector quantum efficiency, $\eta < 1$. The shot noise limited SNR in OCT typically refers to the QL SNR, not the SQL SNR. However, in this work, we will define the shot noise limited OCT SNR as the SQL OCT SNR.

Having covered the basics, we proceed to develop the model. Let us assume monochromatic, single-mode coherent state light for both the sample and reference light and examine five different OCT measurement configurations in order of increasing complexity (Fig. 3.4): OCT measurement with (1) a balanced detector (BD), (2) a BD after a loss medium, (3) a BD after a gain medium, (4) a BD after a loss medium followed by a gain medium, (5) a BD after a gain medium followed by a loss medium. Note that the fundamental assumption is that the noise analysis on a single wavelength SNR scales linearly to a spectrum of wavelength as

long as the noise property is identical across wavelengths.

Analyzing configuration 1 through a quantum lens - figuratively speaking - is the key to simplifying the existing OCT SNR model. The conventional model based on the semi-classical picture, where only the photodetection process is quantized, attributes the shot noise to the random photoelectron conversion of the dominant reference field. This gives the impression that the reference field determines the noise of the OCT SNR while the sample power sets the OCT signal. This model gives numerically correct answers but is physically incorrect. Due to principle (2), the optical shot noise is present independent of the measurement process. In fact, the measured noise is the sample optical shot noise coherently amplified by the large mean reference power. An ideal BD can cancel both the reference shot noise and the reference excess noise. This is because the reference optical noise is fully correlated between the two photodetectors of a BD. In contrast, the sample signal and noise coherently mixed with the mean reference field correlate with a π phase shift. *Thus, the OCT SNR is the sample SNR.* The sole purposes of the reference field are to bring the sample information above the detector's electronic noise and to measure the sample phase and amplitude.

That OCT SNR is the sample SNR dramatically simplifies the analysis of the rest of the configurations. We just need to know the NF of various optical elements with SQL sample SNR at the input. We start by examining the action of a loss element (configuration 2). Classical intuition suggests it should linearly reduce the sample signal and noise power by its transmissivity, L, satisfying the seemingly reasonable boundary condition of zero noise power when there is no photon. Again, this is a classical illusion. Quantum mechanics predicts an unexcited mode containing no photon on average is subject to principle (2) and, therefore, must carry the minimum quadrature quantum noise. That is, linear attenuation reduces the signal power but preserves the shot noise; as the sample light interacts with a loss element, an uncorrelated vacuum noise is necessarily added to satisfy

$$SNR_L = L \times SNR_{sample} \tag{3.14}$$

Thus, $NF_L = \frac{1}{L}$. We comment in passing that the detector quantum efficiency can be treated just like excess loss: $SNR_{QL} = \eta \times SNR_{SQL}$.

For a gain element (configuration 3), uncorrelated vacuum quantum noise must be similarly injected at the amplifier input. The intuition is that a noiseless amplifier is nonphysical because such a device would allow recovery of any minuscule sample information. The additive vacuum noise is amplified along with the sample light, detected as amplified spontaneous emission (ASE) shot noise. Functionally, the action of a PIA is

$$SNR_G = \frac{SNR_{sample}}{1 + \left(\frac{G-1}{G}\right)(2n_{sp} - 1)} \tag{3.15}$$

where G is the amplifier gain and $n_{sp} \geq 1$ is the spontaneous emission factor. The input sample shot noise is degraded by an additional vacuum quantum noise whose magnitude depends on n_{sp}. The denominator of Eq. 3.15 is the PIA NF. If $n_{sp} = 1$, then $NF_{PIA} =$ 3dB, consistent with the fundamental theorem of PIA.

Finally, let us examine a combination of gain and loss elements (configurations 4 and 5). Since the vacuum noise is additive and not multiplicative, the order matters. The sample SNR after a loss element followed by a gain element is simply

$$SNR_{L \to G} = NF_{PIA} \times NF_L \times SNR_{sample}. \tag{3.16}$$

This is consistent with the intuition that a PIA cannot recover lost sample information. The sample SNR after a gain element followed by the loss element is more nuanced because the amplifier gain affects the vacuum noise added by the loss element. For $G \gg 1$, the functional relation is

$$SNR_{G \to L} \approx \frac{G \times SNR_L}{1 + 2n_{sp}GL} \tag{3.17}$$

If $\frac{1}{L} \gg 2n_{sp}G$, then

$$SNR_{G \to L} \approx G \times SNR_L \tag{3.18}$$

That is if the transmissivity is low enough to eliminate the ASE shot noise, then placing a PIA before the loss element improves the SNR by G relative to without the PIA. If $\frac{1}{L} \ll 2n_{sp}G$, then

$$SNR_{G\to L} \approx \frac{SNR_{sample}}{2n_{sp}} \approx SNR_G \tag{3.19}$$

That is if the ASE shot noise remains despite attenuation, then inserting a PIA undoes the action of the loss element. Now, we are fully equipped to address the pertinent question.

3.2.2 Does the Amplifier NF Matter in OCT?

The answer is nuanced but simple. In developing the model, we assumed the input SNR to be the sample SNR. However, it makes no difference to let the input SNR be the source SNR and treat the sample as a high-loss element. Then, Eq. 3.18 tells us that the booster amplifier (amplifier placed before the splitting coupler) NF does not matter and that the OCT sensitivity is improved by G. In practice, G is slightly reduced, less than a dB, by the splitting coupler ratio after the source, and the reference arm must be attenuated by G + NF to eliminate amplifier quantum noise contribution. On the other hand, Eq. 3.19 tells us that the preamplifier (amplifier placed in the sample arm after the sample but before the receiver) NF matters, and the OCT SNR is degraded by the NF_{PIA}. Concisely, amplification before (after) the sample improves (degrades) the SQL OCT SNR by G (NF).

3.2.3 OCT SNR Improvement with a Preamplifier

At first glance, implementing a preamplifier in an OCT system is a terrible idea. However, the assumed SQL OCT SNR is impossible even with the best engineering. For starters, the OCT SNR measured with a classical detector is QL, not SQL. Some systems can operate more than 10 dB away from the SQL SNR due to (1) insufficient detector electronic noise suppression, (2) residual reference noise from imperfect balancing, and (3) excess loss in the sample return arm. We show that such systems significantly benefit from implementing a preamplifier.

The small sample power guarantees the linear operation of the preamplifier; our model is

directly applicable. Since the three discrete SNR degrading mechanisms are uncorrelated, each effect can be considered separately (strictly, the mixing gain can couple the reference RIN with the sample power, which is neglected). Concretely,

$$SNR_{OCT} = \frac{SNR_{sample}}{\rho + \epsilon + \lambda} \tag{3.20}$$

where ρ, ϵ, and λ are defined as follows:

1. ρ: The NF due to residual reference noise in the absence of ϵ and λ. Operationally, it is the measured noise floor increase relative to the SQL sample SNR.

2. ϵ: The NF due to under-suppressed electronic noise in the absence of ρ and λ. Operationally, it is the measured noise floor increase relative to the SQL sample SNR.

3. λ: The NF due to excess sample return arm loss in the absence of ρ and ϵ. This term includes $\eta < 1$ but excludes the mixing coupler used for BD. Operationally, it is the measured signal power reduction relative to $\lambda = 0$. Note that $\lambda = NF_L$ recovers SNR_L.

In introducing realistic system considerations, we note that imperfect balancing results in partial suppression of ASE-ASE beat noise and signal-ASE beat noise, which were absent in our model. Fortunately, these noise terms can be made irrelevant with appropriate amplifier design under typical operating conditions (for more details, see Appendix B). Suppose λ can be partitioned into $\lambda_{pre} \equiv 0$ and $\lambda_{post} \neq 0$ where the subscript means the total excess loss between the sample and the preamplifier input and the total excess loss between the preamplifier output and the BD including $\eta < 1$, respectively. Then, the effect of a high-gain preamplifier on these additive noises can be modeled with Eq. 3.17 with unity replaced with the sum of ρ, ϵ, and λ_{post} and letting $L = 1$,

$$SNR_{OCT}|_G \approx \frac{SNR_{sample}}{2n_{sp} + \frac{1}{G}(\rho + \epsilon + \lambda_{post})} \tag{3.21}$$

Evidently, Eq. 3.21 reduces to Eq. 3.19 with $\rho = \epsilon = \lambda_{post} = 0$. That is, the PIA simultaneously suppresses all noise processes that do not interact with the amplifier. The

expected SNR improvement relative to SNR_{OCT} in dB unit is

$$\Gamma_{PIA} = 10log_{10}[\rho + \epsilon + \lambda_{post}] - 10log_{10}[NF_{PIA} + \delta] \tag{3.22}$$

where δ can be thought of as a noise buffer for reasons discussed later, $\frac{1}{G}(\rho + \epsilon + \lambda_{post})$.

Before discussing in detail the practical implication of Eq. 3.22, we briefly analyze a unique class of receiver. The balanced IQ receiver used to reconstruct complex OCT fringe can achieve SQL SNR with an ideal preamplifier (fig. B). For simplicity, let $\rho = \epsilon = \lambda_{post} = 0$. Due to the 50:50 coupler used to split the sample light into I and Q channels, the SNR that each BD sees is SNR_L with $L = \frac{1}{2}$. When the I and Q channels are coherently combined to reconstruct a complex fringe, the signal is quadrupled while the shot noise is doubled. Therefore, the OCT SNR in configuration 1 is identical to the OCT SNR with a balanced IQ receiver. Now, suppose an ideal high-gain preamplifier is inserted before the receiver. Eq. 3.17 with $L = \frac{1}{2}$ yields $\frac{SNR_L}{n_{sp}}$. Thus, the SNR measured by respective BD with and without an ideal preamplifier is identical. The SQL sample SNR is recovered exactly after complex fringe reconstruction. For the IQ receiver considered here, Eq. 3.22 can be written as

$$\Gamma_{PIA}|_{BD} = 3dB + 10log_{10}[\rho + \epsilon + \lambda_{post}] - 10log_{10}[NF_{PIA} + \delta] \tag{3.23}$$

We comment that complex OCT fringe reconstruction with temporally-encoded IQ takes the full NF_{PIA} penalty unlike the IQ receiver considered here.

3.2.4 Practical Implications and Applications for Integrated Photonics

The results above have important practical implications. First, an OCT system with a preamplifier and a balanced IQ receiver can perform better than the QL OCT system. Depending on the operating wavelength, η for even the best-optimized detector can be as low as 1dB. Erbium-doped fiber amplifiers (EDFA) have been experimentally shown to achieve sub-4dB NFs. Therefore, for EDFA with 3.6 dB NF and $\eta = 1$ dB, the sensitivity with a

preamplifier would be 0.4 dB better than the expected QL OCT sensitivity. Some SOAs can achieve NF as low as 5 dB, which only suffers a net 1 dB sensitivity penalty.

Second, an OCT system with a preamplifier offers a significantly increased tolerance to the source and detector specs. For demonstration, let us examine a scenario where $\epsilon = \lambda_{post} = 0$ and $\rho = 10$. The source RIN is so high that even with balancing the SQL OCT SNR is degraded by 10 dB. Now, insert a preamplifier with G = 23 dB and NF = 6 dB. Then, $\Gamma_{PIA} = 3.93$ dB with 0.07 dB perturbation from δ. Suppose one designs a cheaper swept source that can tolerate various imaging conditions but comes at a cost of 10 dB increased RIN. Now, SQL OCT SNR is degraded by 20 dB. But, with the same amplifier, $\Gamma_{PIA} = 13.47$ dB with 0.53 dB perturbation from δ. This means a massive 10 dB degradation in source quality leads to a trivial 0.46 dB change in the buffer contribution. This benefit extends to ϵ as well. A preamplifier allows OCT systems with faster or cheaper detectors with increased noise equivalent power. As OCT community continues to expand the application fields, the increased flexibility on the source and detector specs is welcome.

Finally, a system with a preamplifier becomes immune to λ_{post} insofar as the condition on Eq. 3.19 is satisfied. This opens up an exciting opportunity to build somewhat luxurious receivers with high excess loss in mind. One application is photonic integrated OCT platforms that suffer significant loss from high coupling loss (> 5 dB) and waveguide loss [44]. SOA chips can be integrated on the photonic chip to overcome the high excess loss. Combined with a phase-diverse receiver, a near shot-noise limited sensitivity can be realized. This enables implementing complex analog processing and computations steps on chip prior to digitization.

3.2.5 The SNR Benefit of an Asymmetric Spectral Shape

Section 3.2 showed that amplifier placement inside of an interferometer is not a crazy idea - in fact, it can have a sensitivity advantage. However, in that analysis, the gain unflatness of the amplifier was not considered, and this also affects OCT sensitivity. For the inline (amplifier in the sample arm before the sample) amplifiers or preamplifiers, the reference arm

and the sample arm will have different spectra. The first question is, is this bad? Typically, the OCT fringe is windowed before reconstruction to obtain the desired psf. The commercial source typically has a flat power spectral density, but based on the revised OCT SNR model, an ideal reference spectrum is flat while the ideal sample spectrum is the square root of the desired psf (this makes intuitive sense because all sample photons contribute to the signal - no sample photon is digitally windowed). In this way, each wavelength has sufficient reference power to overcome the electronic noise limit, and RIN will be wavelength-independent. This suggests that spectral unflatness is, in fact, desired. For a photonic integrated circuit, tailoring the spectrum for each arm can be as trivial as adding a gain medium in the sample arm. The second question is then, how much better?

To answer this, an analytical solution is derived. Assume (1) the target psf is known, (2) the average sample power is constant for arbitrary spectral shape, and (3) the reference arm is spectrally flat and is shot noise limited. Suppose a sample field with a slowly varying envelope with a certain amplitude $S(t)$ and source carrier field $E_{laser}(t)$ with unit power

$$E_s(t) = S(t)E_{laser}(t) \tag{3.24}$$

The only constrain on $E_s(t)$ is that the time-averaged power is unity prior to attenuation. Assuming perfect mixing with the reference field, the detected fringe with perfect balancing with the digital windowing function $D[n]$, $n \in [\![0, N]\!]$, is

$$F[n] = \alpha D[n]S[n]cos[\phi[n]] + D[n]\mathcal{N}[n] \tag{3.25}$$

where α combines scaling factors from electronic mixing of reference and sample fields, and the additive Gaussian photodetection noise $\mathcal{N}[n] \sim (0, \sigma^2)$. Suppose the desired window shape is $H[n] \leq 1 \forall n$. This yields the constraint

$$S[n]D[n] = cH[n] \tag{3.26}$$

where c is the scaling factor to be determined and would depend on $S[n]$. In general, the

signal power is

$$P_S = \frac{\alpha^2 c^2}{N} \sum_{n=1}^{N} H[n]^2 cos[\phi[n]]^2 \tag{3.27}$$

And the noise power is

$$P_N = \frac{1}{N} \sum_{n=1}^{N} (D[n]^2 \mathcal{N}[n]^2 - \frac{1}{N} \sum_{n=1}^{N} (D[n] \mathcal{N}[n])) \tag{3.28}$$

Given the zero-mean additive noise with variance σ^2, this simplifies to

$$P_N = \frac{\sigma^2}{N} \sum_{n=1}^{N} D[n]^2 = \frac{\sigma^2 c^2}{N} \sum_{n=1}^{N} \frac{H[n]^2}{S[n]^2} \tag{3.29}$$

Then the detected SNR is

$$SNR = \frac{\alpha^2 \sum_{n=1}^{N} H[n]^2 cos[\phi[n]]^2}{\sigma^2 \sum_{n=1}^{N} \frac{H[n]^2}{S[n]^2}} \tag{3.30}$$

This equation is already telling. Given a constant α^2 and σ^2, the SNR will change as a function of $S[n]$. But the amplitude of $S[n]$ is unknown for this general expression. A ratiometric expression is helpful to cancel the implicit field strength. To that end, consider the case $S(t) = 1$, which is the case of a symmetric sample and reference field profile. Rearranging Eq. 3.26 with the unity power constraint yields

$$\frac{1}{N} \sum_{n=0}^{N} S[n]^2 = c^2 \frac{1}{N} \sum_{n=0}^{N} \frac{H[n]^2}{D[n]^2} = 1 \tag{3.31}$$

Thus,

$$c^2 = \frac{1}{\frac{1}{N} \sum_{n=0}^{N} \frac{H[n]^2}{D[n]^2}} \tag{3.32}$$

Eq. 3.26 gives another trivial relation,

$$c^2 = \frac{D[n]^2}{H[n]^2} \tag{3.33}$$

The only nontrivial case for which Eq. 3.32 and Eq. 3.33 coincide $\forall n$ is

$$H[n] = D[n] \tag{3.34}$$

From Eq. 3.31,

$$c^2 = \frac{1}{N}\sum_{n=0}^{N} S[n]^2 \tag{3.35}$$

The SNR can be computed similarly to the baseline case. The signal power is

$$P_S|_{S(t)=1} = \frac{\alpha^2 c^2}{N}\sum_{n=1}^{N} H[n]^2 cos[\phi[n]]^2 \tag{3.36}$$

and the noise power is

$$P_N|_{S(t)=1} = \frac{\sigma^2}{N}\sum_{n=1}^{N} D[n]^2 = \frac{\sigma^2}{N}\sum_{n=1}^{N} H[n]^2 \tag{3.37}$$

The resulting SNR is

$$SNR_{S(t)=1} = \frac{\alpha^2 \frac{1}{N}\sum_{n=0}^{N} S[n]^2 \sum_{n=1}^{N} H[n]^2 cos[\phi[n]]^2}{\sigma^2 \sum_{n=1}^{N} H[n]^2} \tag{3.38}$$

Let us define the rationmetric quantity as

$$\Gamma[S[n]; H[n]] = \frac{SNR}{SNR_{S(t)=1}} \tag{3.39}$$

which yields

$$\Gamma[S[n]; H[n]] = \frac{\sum_{n=1}^{N} H[n]^2}{\frac{1}{N}\sum_{n=0}^{N} S[n]^2 \sum_{n=1}^{N} \frac{H[n]^2}{S[n]^2}} \tag{3.40}$$

This expression can accept any general envelope profile without *a priori* knowledge of the $S[n]$ amplitude - any common factors will cancel - and is independent of the electronic noise. For the target psf of Hanning, the 1.75 dB gain is expected when $S[n]^2 = H[n]$. For Gaussian window shape, which is often assumed in theoretical derivation, the SNR gain of the asymmetric spectrum can be as high as 6.7 dB (see Fig. 3.5).

3.3 Practical Implementation of Optical Amplifier

3.3.1 High-power Booster Amplifier

Erbium/Ytterbium-Co-Doped Fiber Amplifier (EYDFA) at 1590 nm

The first CR-OCT surgical system prototype capable of multi-centimeter FOV, real-time, volumetric nerve imaging was built in the Vakoc lab. The system multiplexed 32 channels of illumination and collection fiber for wide-field, real-time, volumetric nerve imaging. Since the conventional, single-channel OCT system operates at $\sim$ 10 mW average power, the multi-beam system required at least 32-fold higher power to maintain equivalent sensitivity. For this application, a high-power EYDFA with 50 nm bandwidth and $>$ 1W average power was built and validated.

Fig. 3.6 (a) shows the EYDFA schematic. Besides achieving the wide-band and high-gain, the PMD needed to be minimized for PS-imaging. In the first stage, a 7 m L-band EDFA (M12-980-125, Fibercore, USA) was pumped with a 976 nm single-mode pump diode (BL976-PAG90, Thorlabs, USA) through a fused wavelength-division multiplexor (WDM) (WP9850, Thorlabs, USA) in a double-pass configuration. This design was simulated (GainMaster, Fibercore, USA) to ensure high population inversion and pump saturation were achieved throughout the length of the fiber. The Faraday rotator mirror (FRM) (ACphotonics, USA) was implemented to cancel the PMD induced by the Erbium fiber. A 13 dB gain was achieved in the first stage (output power $\sim$ 110 mW). Any higher pump power led to parasitic lasing from high small signal gain. The preamplifier stage was connected to and isolated from the booster stage with a high-power circulator (ACphotonics). In the booster stage, PMD was minimize by using a 25 m PM-EYDFA (PM-EYDF-6/125-HE, Coherent, USA). A double-pass configuration was obviated to ensure no parasitic lasing occurs in the high-power stage. The EYDFA was pumped with a 10 W mluti-mode laser diode (PDL-10-975, IPG Photonics, USA) through a pump-signal combiner (PSC) (500-91812-01-1, Lightel, USA). The polarization controller before the PSC was manipulated to align the signal polarization to the fiber optic axis. A high-power isolator (Agiltron) was placed at

the second stage output for stability. The average power measured at this point was 1.38 W (total 24.4 dB gain), meeting the power requirement. The residual PMD was cleaned up by a polarization delay circuit, where the delay length is determined by the comb pulse width. Besides the component loss and PMD loss, this circuit should not affect the power and spectral performance of the amplifier. The source spectrum before and after the amplifier are shown in Fig. 3.6 (a) and (b), respectively. The degree of spectral unflatness would only lead to a slight SNR degradation according to the theory developed in Section 3.2.5, and therefore is not a major concern. The amplifier module was packaged and secured for imaging experiments (Fig. 3.7).

Ytterbium-Doped Optical Fiber Amplifier at 1060 nm

A high-power solution at 1.0 μm wavelength was experimentally demonstrated with YDFA. Fig. 3.8 shows the amplifier schematics. Due to a high gain property of Ytterbium, a single-stage was sufficient to achieve $>$ 1W average output power. It comprises a high-power isolator (Model BI-06-C8-20-NN-LL-1-10/125, DPM Photonics, USA) and a 6 m PM-YDFA (LIEKKI® Yb1200-10/125DC-PM Optical fiber, nLight, Finland). Since the HI1060 fiber and the amplifier mode size is different, the PM-mode field adaptor (MFA) (43939 MFA-980/1064-6/125-10/125-0.11-0.08-S-LMA-XX-1-1, OzOptics, Canada) was used. Since YDFA can be pumped efficiently at 976 nm, the same pump LD as the one used in EYDFA could achieve high population inversion. The amplifier was characterized by a commercial 1.0 μm swept source (Excelitas Technologies Corp., USA). The average source power was 20 mW, and the spectrum is shown in Fig. 3.8 (b). The output spectrum at the amplifier output is shown in Fig. 3.8 (c). Since the input source spectrum was wider ($>$ 110 nm) than the amplifier bandwidth ($\sim$ 75 nm), not all wavelengths were amplified. The amplifier center wavelength could be shortened by reducing the fiber length and increasing the pump power to compensate for the reduced cumulative gain. Compared to EYDFA, YDFA has a flat gain spectrum, which is advantageous for ophthalmic applications where tissue safety limits total sample arm power.

3.3.2 SOA Nonlinearity in In-line Amplifiers

SOAs have a ps-scale gain dynamics. Thus, they can respond to any RIN up to at least a few GHz. Due to the low saturation power, nonlinear effects are much more accessible for SOAs than DOFAs. In this regime, phase noise and amplitude noise become highly coupled. The amplitude noise results in time-dependent refractive index changes, leading to phase noise with a magnitude determined by the degree of amplifier saturation. Shin et al. experimentally showed that SOAs operating in a deeply saturated regime reduce source RIN, which is advantageous for achieving a shot-noise-limited system [45]. On the other hand, Al-Qadi et al. showed that saturated SOAs lead to phase noise enhancement. The effect was measurable in a coherent detection system [46]. Together, SOAs result in reductions in RIN (good) and coherence coherence length (bad). However, there has not been a study of what happens if SOAs are used as in-line amplifiers, where saturated operation is almost guaranteed for high-power applications. What is the effect of having the sample arm light and the reference arm light with different coherence lengths? A preliminary experimental result and an important observation are presented.

Methods

The experimental setup is shown in Fig. 3.9. The psfs obtained from the booster configuration (Fig. 3.9 (a)) and the in-line amplifier configuration (Fig. 3.9 (b)) were compared. A commercial source (HSL-200-50LC, Santec Corp., Japan) at 1310 nm center wavelength with a 6 mm coherence length was used. The variable attenuator (VA) was used to control the input power to the SOA to ensure saturated operation. The polarization controller (PC) (FPC030, Thorlabs, USA) was manipulated to align the polarization state to maximize input to the high-power SOA (BOA1130S, Thorlabs, USA). The source power was 3.1 mW at the amplifier input and was amplified to 108 mW, resulting in a deeply saturated 15.4 dB gain. This beam was then split between the reference and the sample arm. To eliminate other potential noise sources from backreflection, a single-pass MZ setup was used. The free-space polarization beam splitter ensured that any PMD effect was cleaned up prior to mixing. An ND filter attenuated the sample power down to 2.95 nW and reference power sufficient to

achieve optical shot noise. The interference fringe was balanced-detected (DB460, Thorlabs, USA) and low-pass filtered to reduce aliased electronic noise. The fringe was then digitized (TS9350, AlazarTech, USA) for signal processing and psf reconstruction. Multiple fringes were acquired at different sample arm displacements covering the source coherence length, and at least 100 A-lines were acquired per displacement for averaging.

The configuration of interest is shown in Fig. 3.9, where the saturated SOA is placed inside of the interferometer before the attenuator. The input power was 2.3 mW, and the output power was 101 mW, resulting in a 16 dB gain. An identical reference power was used to ensure that its fringe and noise contribution is the same as in Fig. 3.9 (a). The sample power was attenuated to 3.39 nW. Besides the delay line necessary to path-match the two arms, the rest of the setup and measurement protocol remained identical.

The fringe data was processed with a custom MATLAB script. Background subtraction, Hanning windowing, and numerical dispersion compensation were applied. The fringes were coherently averaged, and the pdfs were plotted as a function of distance.

Results

The results are shown in Fig. 3.10. The booster configuration had a 6 dB roll-off at 7 MHz, while the in-line amplifier configuration had a 6 dB roll-off at 20 MHz. For the booster measurement, the measured psf past 15 MHz becomes unreliable due to low signal power. This is not the case for the inline amplifier configuration, in which a reliable SNR is maintained past the 6 dB roll-off. However, the signal peal was lower by 8 dB for in-line amplifier. The reason for this is explained in the discussion section below. A slight rise in the noise floor was observed between 0 and 20 MH, though it does not significantly affect the SNR.

To determine whether the asymmetric phase noise property results in an asymmetric envelope about the true path-match, the measurements were repeated with both the positive and the negative path mismatch as a function of SOA gain saturation. Fig. 3.11 shows the result of this experiment. The top row shows the psfs when SOA is not saturated. The last row

shows the psfs when SOA is deeply saturated (more than 8 dB gain clamping). There is a clear shift toward one side of the path mismatch.

Discussion

At high gain, the expectation was to observe an SNR reduction from the noise floor rise due to the phase noise that is not effectively balanced. Although a slight rise in the noise floor was seen, the biggest source of the SNR reduction was the 8dB signal reduction, where none is expected in theory. There are several possible explanations for this, which need to be verified for future experiments. The first is the different reference arm spectrums for the two experimental configurations. Keeping the average reference power is not the best control of the experiment. In the booster configuration, the amplifier spectral shape applies to both the reference and the sample arm. Therefore, all the reference power contributes to the signal. However, in the in-line amplifier configurations, wavelengths outside the amplifier bandwidth do not contribute to the fringe signal, though they contribute to the measured average power. In future experiments, the reference peak power must be controlled, not the average reference power.

An interesting result not originally hypothesized was the saturation-dependent envelope peak shift. This is effectively a saturation-dependent frequency shift. The simplified SOA model (orignially Eq. 3.1) used by Al-Qadi et al. offers an insight [46]. The effective model for the field before and after the amplifier is given as

$$E_{out}(t) = E_{in}(t)exp[(1 - i\alpha)h(t)/2] \tag{3.41}$$

where α is the linewidth enhancement factor and $h(t)$ is the effective gain parameter obtained by solving

$$\left(1 + \tau_c \frac{d}{dt}\right) h(t) = h_0 - \frac{|E_{in}(t)|^2}{P_{sat}}[exp[h(t)] - 1] \tag{3.42}$$

where $h(t) = \int_0^L g(z,t)dz$ is the gain integrated along the active length, $h_0 = lnG_0$ with G_0 being the small signal gain, and P_{sat} is the saturation power. The exponent in Eq. 3.41

can be separated into amplitude and phase effect. This is particularly useful since the phase effect can be lumped into the argument of ϕ_s in Eq. 2.3. Thus, the SS-OCT fringe for in-line amplifier is simply

$$I_{BD} \propto cos(2k(t)\Delta z + \frac{\alpha h(t)}{2}) = cos(2k_0\Delta z + 2\kappa\Delta z t + \frac{\alpha h(t)}{2}) \tag{3.43}$$

The last term explains the origin of the observed frequency shift. When the SOA is unsaturated, $h(t)$ is constant. The fringe is unaltered. When the SOA is saturated, then $h(t)$ will have a shape that is the inverse of the source waveform for the wavelength that saturates the amplifier. The $h(t)$ will have up to second-order terms for a Gaussian spectrum. This results in the observed frequency shift and other higher-order frequency effects resulting in the asymmetric envelope.

In the context of spectral shaping and integrated photonics OCT applications, this result is meaningful. An in-line SOA provides an electro-optical means to control the fringe property without degrading the coherence length. A potential application is analog speckle reduction by rapidly jittering the phase at the ps time scale. It could also be used to equalize the SNR as a function of depth, which is important for long-range imaging applications like surgical OCT.

3.4 Summary

This Chapter reported a comprehensive study of amplifier properties affecting OCT sensitivity. The revised SNR model supports using an optical amplifier for power-hungry surgical OCT applications. Two high-power amplifiers with >1 Watt average power were built for use in 1.0 μm and 1.5 μm systems. Moreover, interesting futuristic applications of amplifiers were presented, which may address the system complexity issue outlined in section 1.3.5 as photonic integrated circuit technology matures.

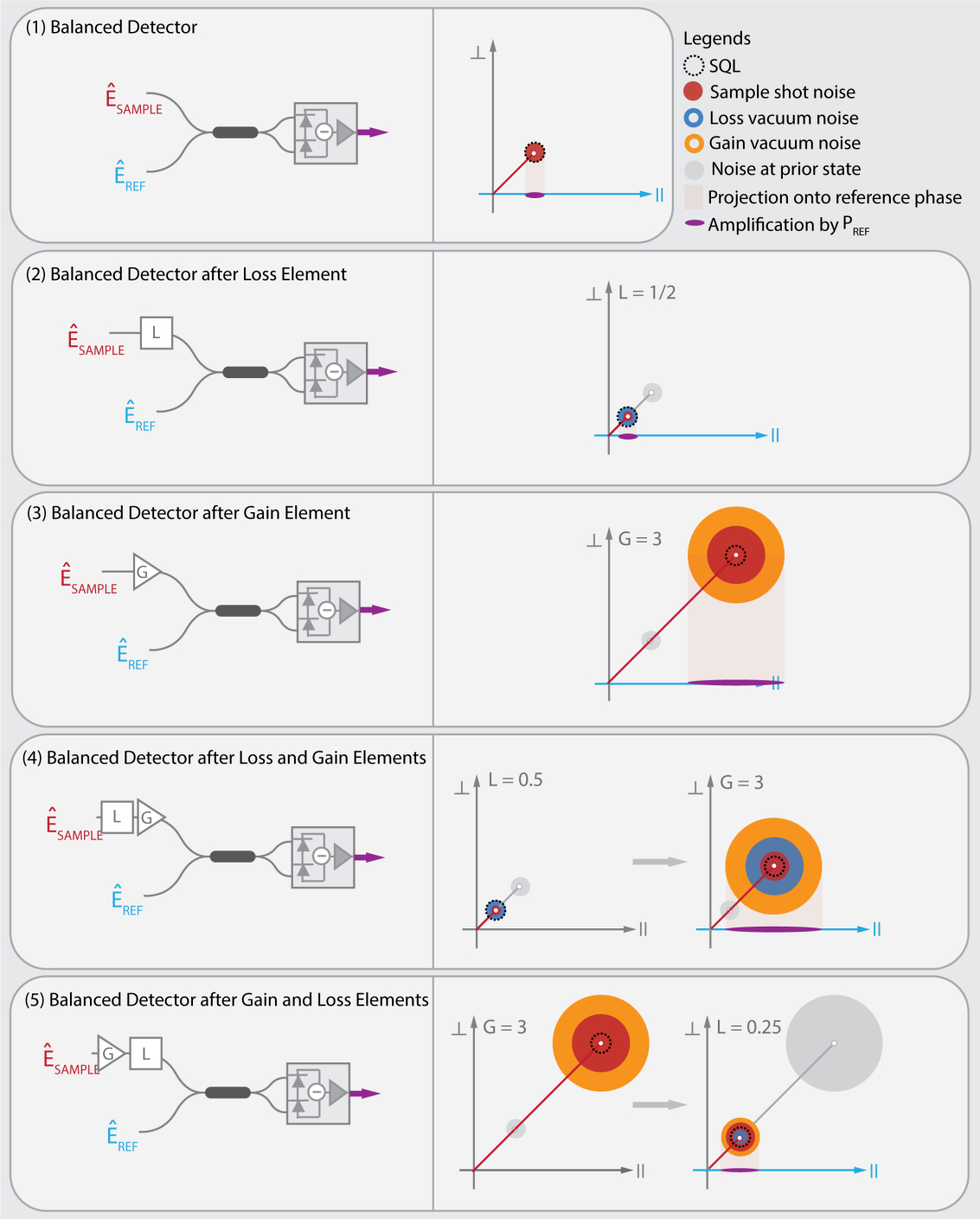

Figure 3.4: Five configurations under considerations. The left panel shows the physical detection setup. The right panel shows a phasor representation of the measured SNR. The sample field is projected onto the reference field angle and then amplified by the reference mean field power.

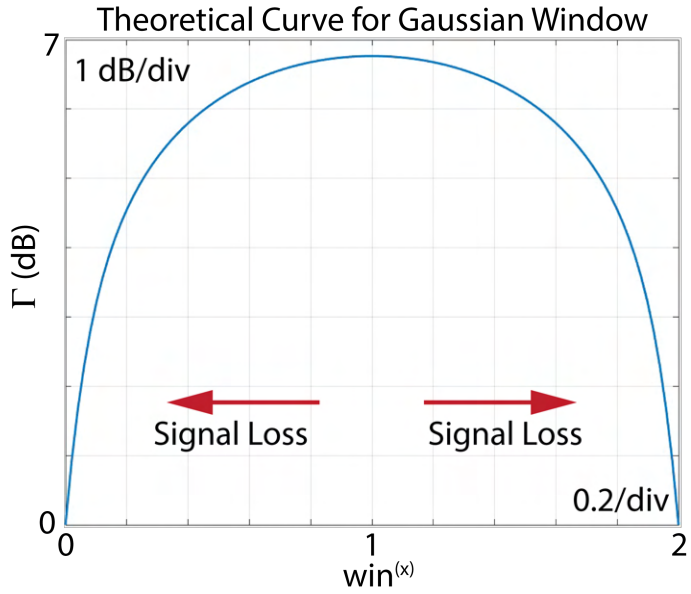

Figure 3.5: Γ when $H[n]$ is Gaussian window. The SNR gain is plotted as a function of the sample arm spectral shape. For simplicity, the Gaussian function is used as the basis function, and different shapes were generated by varying the power of the basis function.

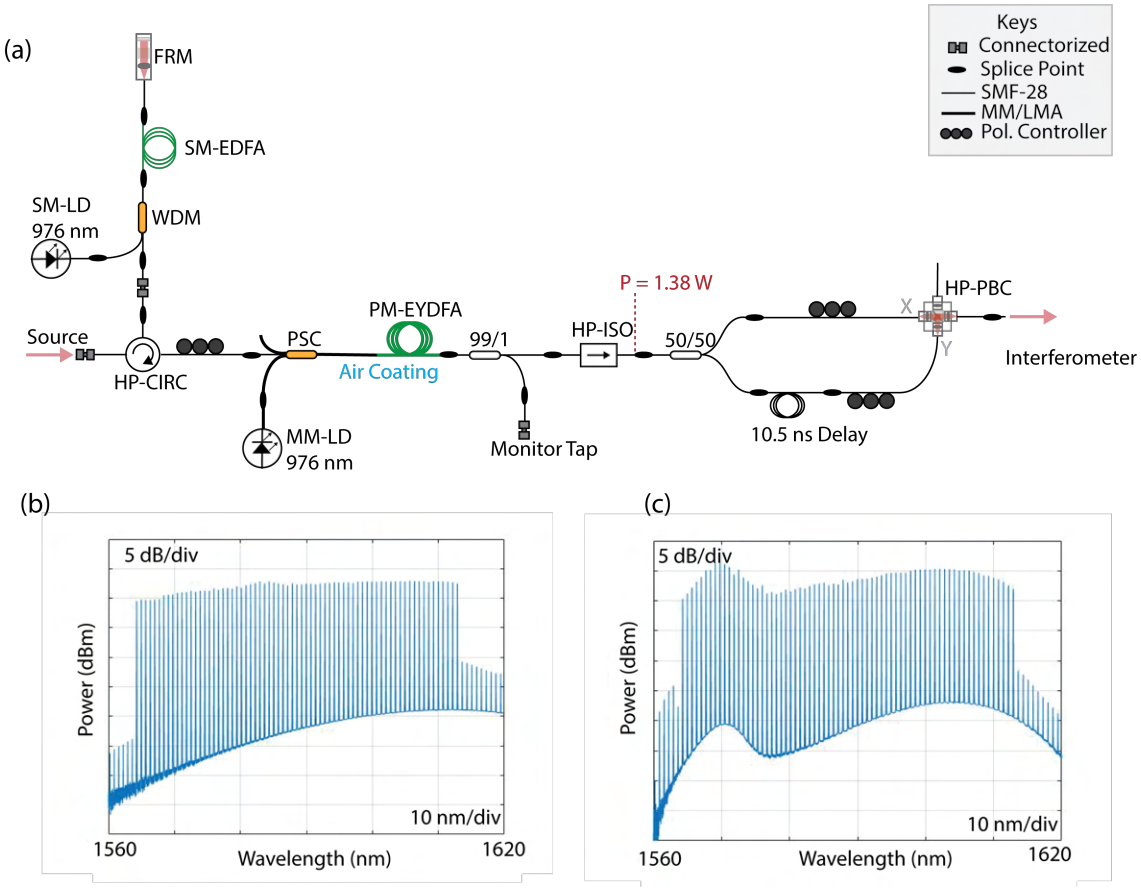

Figure 3.6: High-power amplifier design and performance for 1590 μm band. (a) EYDFA schematics. HP-CIRC: High-power circulator; SM-LD: Single-mode laser diode; WDM: Wavelength-division-multiplexor; SM-EDFA: single-mode EDFA; FRM: Faraday rotator mirror; PSC: pump-signal combiner; MM-LD: multi-mode laser diode; PM-EYDFA: polarization maintaining EYDFA; HP-ISO: High-power optical isolator; HP-PBS: high-power polarization beams splitter. (b) L-band frequency comb spectrum for the multi-beam system. (c) the same source spectrum at the amplifier output. .

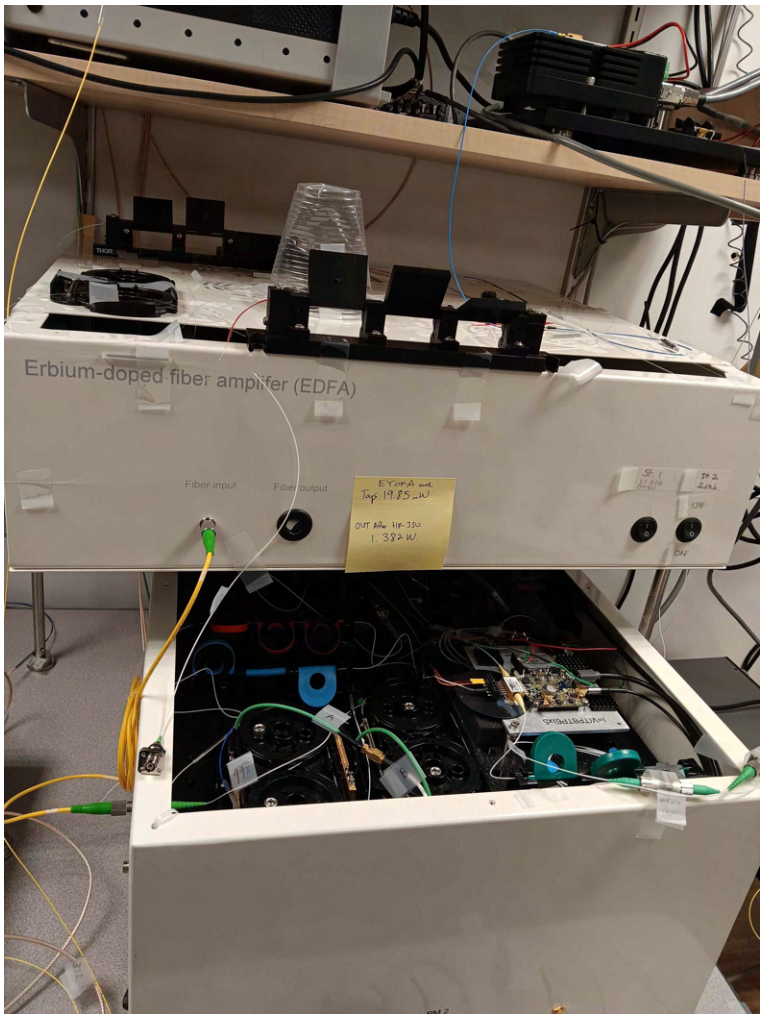

Figure 3.7: Packed EYDFA module. The output fiber was temporarily taken out for testing. The module was placed right on top of the time-stepped frequency comb source box on the bottom.

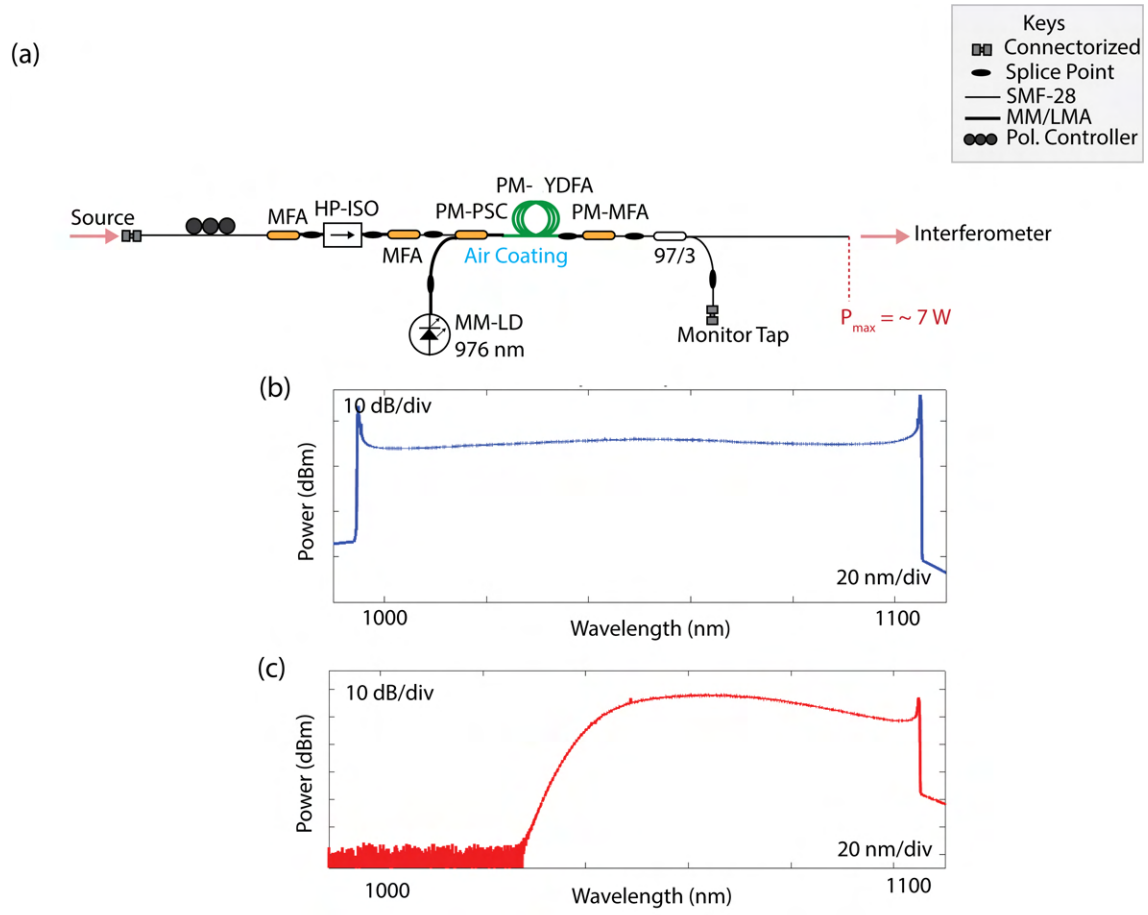

Figure 3.8: (a)High-power amplifier design for 1.0 μm system. The high gain efficiency of the Ytterbium atom allows much higher average output power in a shorter fiber length than the EDFAs. (b) The input source spectrum of the commercial source. (c) The output source spectrum. Note the shorter wavelength is cut-off since the gain bandwidth is narrower than the source bandwidth .

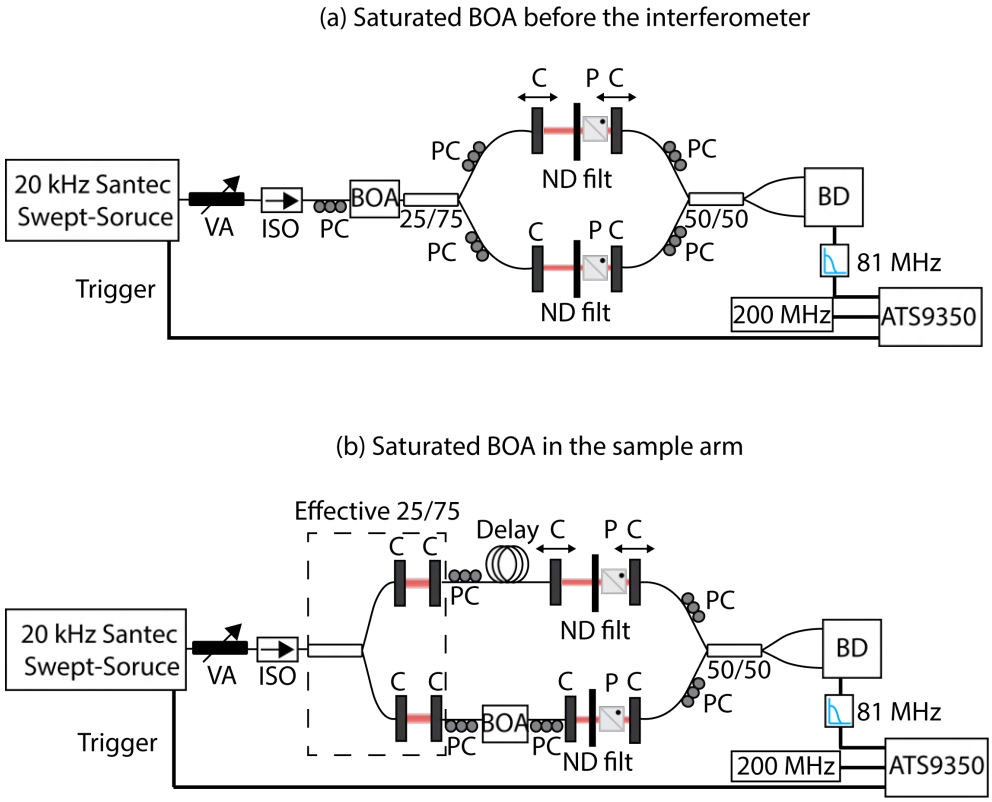

Figure 3.9: Experimental setup for SOA nonlinearity experiment. (a) Baseline system where the SOA is placed in the booster configuration: BOA: Booster optical amplifier; VA: Variable optical attenuator; PC: polarization controller; NDfilt: Neutral density filter;C: Collimator; P: Polarization-beam splitter; BD: Balanced detector. (b) Experimental setup for testing SOA nonlinearity in the sample arm before the sample.

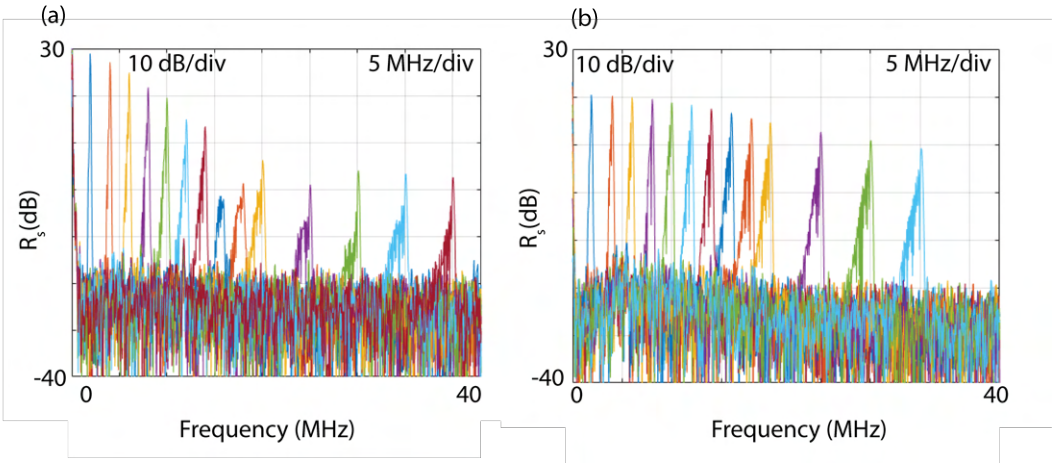

Figure 3.10: PSF measuremt as function of mirror translation. (a) Baseline booster configuration. (b) In-line amplifier configuration.

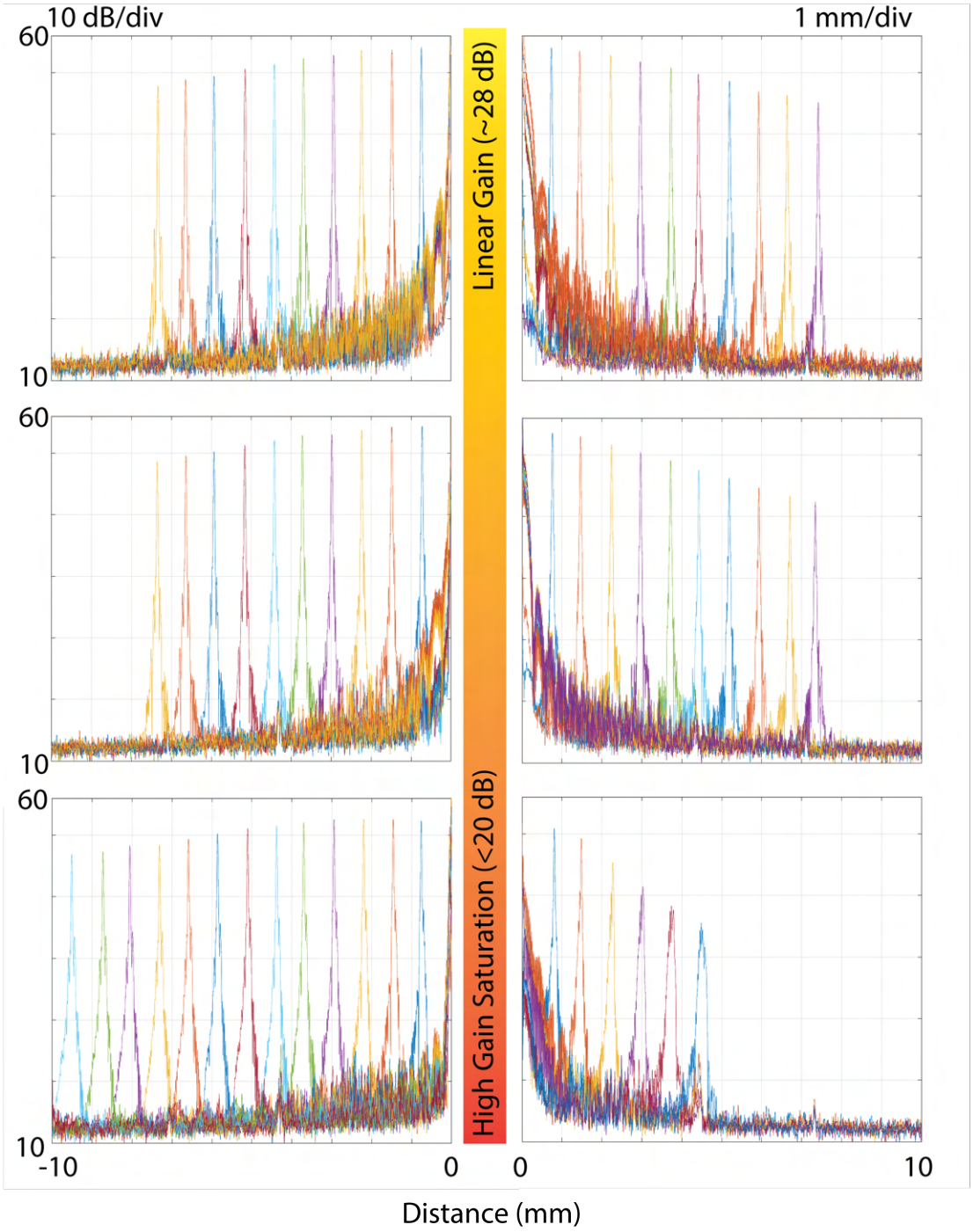

Figure 3.11: PSF measuremt as function of mirror translation. As the input power to the SOA was increased, the non-linear phase effect became more prominent. At high gain saturation, the signal's peak was shifted with asymmetric coherence length about the absolute zero point.

Chapter 4

Contour-Looping (CL-) OCT

Chapters 1 and 2 presented technical challenges of building a volumetric surgical OCT system. In Chapter 3, strategies to overcome the sensitivity problem of high-speed, long-range OCT systems were demonstrated. In this Chapter, a novel OCT architecture, CL-OCT (pronounced cloaked), that simultaneously addresses the data bandwidth bottleneck (section 1.3.2) and system complexity (section 1.3.5) is presented. It achieves an aggressive data reduction while preserving sufficient long-range depth information to identify the unique nerve signature. It forgoes simultaneous volumetric image capture, making it compatible with endoscopic cameras. The source is also dramatically simplified compared to the time-stepped frequency comb used in CR-OCT, which helps reduce system complexity.

4.1 Theory

The data acquisition electronics bottleneck in the conventional OCT architecture stems from the one-to-one mapping of depth to RF frequency at a given A-line rate. Each frequency bin corresponds to a physical space whether it contains the sample of interest or not. For surgical applications where the goal is to quickly identify a tissue of interest, this approach is highly inefficient. This is akin to a search algorithm that looks through every element of the list to find the entry of interest. CR-OCT, based on a time-stepped freqeuncy comb source, enabled partial decoupling of depth and RF bandwidth. The number of comb lines determined the number of samples while the comb linewidth set the imaging depth range. In the search

algorithm analogy, CR-OCT allowed simultaneously looking at a subset of the physical space spanning all possible search space. By picking the right size of the subset, all search attempt contains tissue signal. However, it still required multiple sampling to reconstruct a resolved depth slice. For high-speed imaging, the volumetric data throughput is incompatible with any imaging sensors. CL-OCT achieves much more aggressive data compression by looking at a single slice of the physical space instead of a subset of physical space, where the source determines the slice separation. As a result, it can acquire multiple-depth information in a single measurement.

CL-OCT realizes the above functionality by combining the TD-OCT with a frequency comb source. Therefore, Eq. 2.5 can fully describe its working principle. A general equation to describe the frequency comb source is

$$S(k) = G(k)\big[L(k) * \sum_{n=-M}^{M} \delta(k - nk_0)\big] \tag{4.1}$$

where $L(k)$ is the linewidth function, $A(k)$ is the spectral power at k, k_0 is the frequency spacing or the free spectral range (FSR), and M relates to the total number of comb lines, N, via $N = 2M + 1$. A simple analytical expression for I_{BD} can be derived assuming the Gaussian function for $G(k)$ and $L(k)$ (see Appendix B for the complete derivation). The resultant photocurrent is

$$I_{BD}(z) = 2\frac{\eta q}{h\nu\sigma_s}\sqrt{\frac{r(z)\sigma(1-\sigma)}{2\pi}}e^{-2z^2\sigma_l^2}\sum_{n=-M}^{M} exp\left[\frac{k_0 n + k_c}{\sigma_l}\right]^2 cos[2z(k_0 n + k_c)] \tag{4.2}$$

where σ_s is the source bandwidth, σ_l is the comb linewidth, and k_c is the center frequency of the source. In Eq. 2.11 only the term $exp(-z^2\sigma_k^2)$ gives spatial localization at z. Sampling other depth points required physically translating the reference mirror. In Eq. 4.2, two factors determine the spatial localization. The first exponent in Eq. 4.2 gives a spatial localization at z with the decay rate determined by the source linewidth instead of the source bandwidth. This factor sets the imaging depth range or the search distance. The

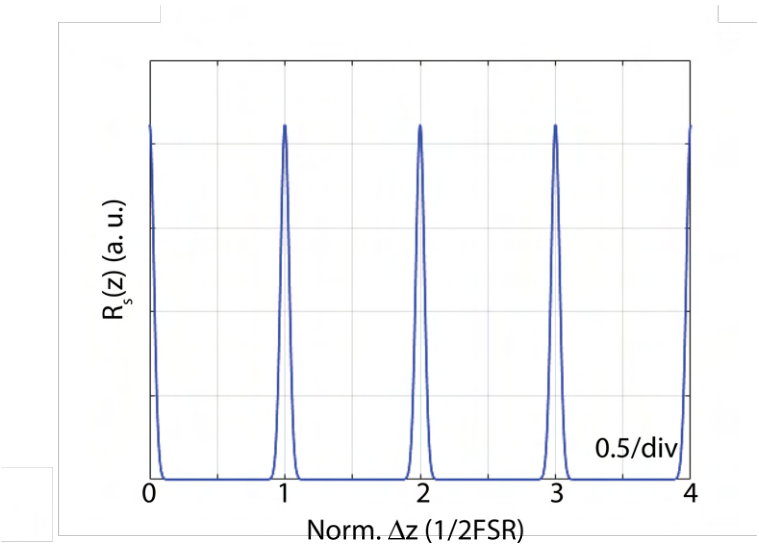

Figure 4.1: A field-based Python simulation code was written to perform a mirror translation experiment. CL-OCT allows multiple spatial localizations.

second factor of the discrete finite sum describes a pulse train with the spatial resolution determined by the FWHM of the source bandwidth and the depth separation determined by the FSR, $z_0 = \frac{\pi}{k_0}$. Thus, in CL-OCT a single measurement contains the coherent sum of all spatial information localized by the discrete pulse train within the imaging depth range without moving the reference mirror. Fig. 4.1 is a simulated mirror translation experiment where the sample mirror was fixed and the reference mirror was moved for 4 normalized distance units. When the path-mismatch is an integer multiple of the inverse of the FSR, interference occurs. For tissue imaging, the FSR can be selected such that the signal coming from z_n dominates that coming from the subsequent layer, z_{n+1}, where the probe beam experiences substantial tissue attenuation or scattering. In theory, the minimum necessary RF bandwidth is determined by the maximum sample speed, 10 kHz at most. In practice, the signal is modulated at a carrier frequency for lock-in detection, which sets the required RF bandwidth at approximately 10 MHz.

4.2 Proof of Principle CL-OCT System

Fig. 4.2 shows the schematics of the proof of principle CL-OCT system. It comprises four parts: the source, the interferometer, the microscope, and the detector.

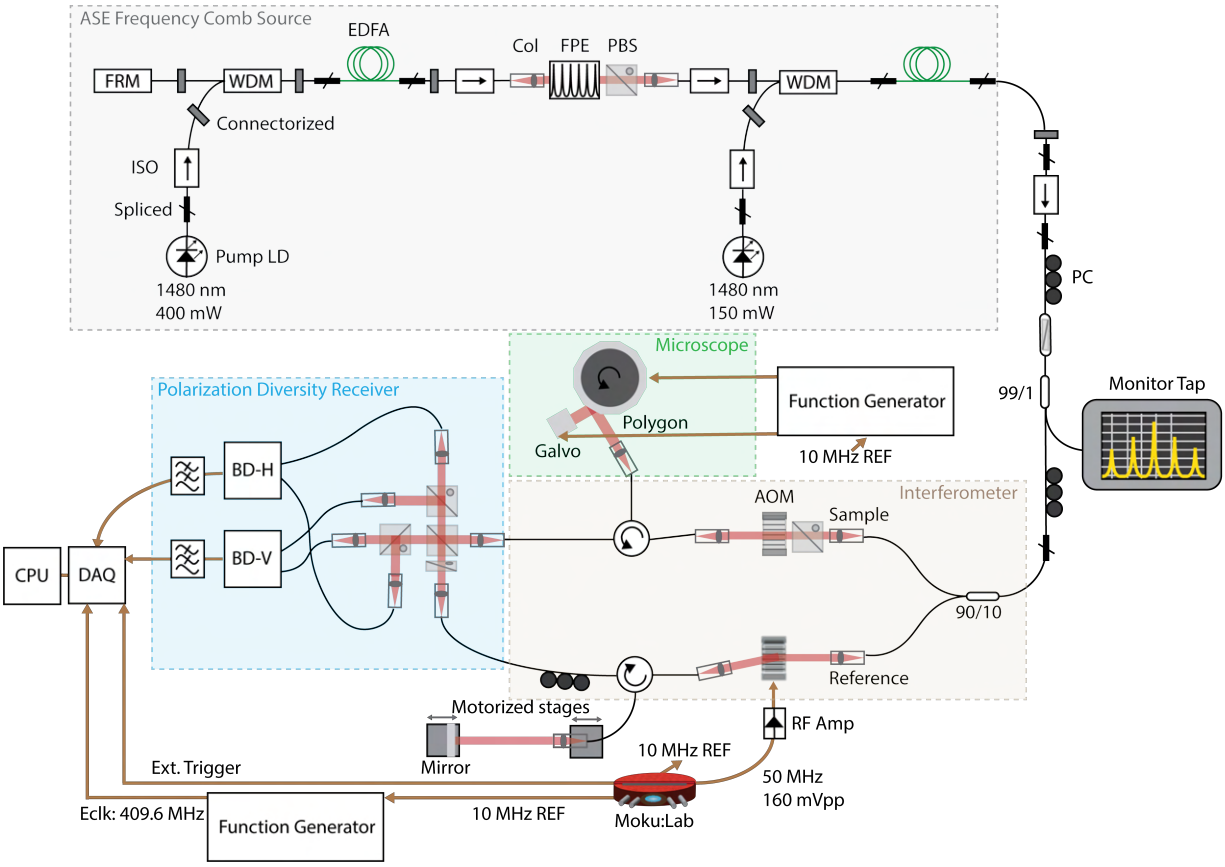

Figure 4.2: Proof of principle CL-OCT system schematics. FRM: Faraday Rotator Mirror; ISO: Isolator; WDM: Wavelength-division Multiplexing; EDFA: Erbium-doped Fiber Amplifier; Col: Collimator; FPE: Fabry-Perot Etalon; LD: Laser Diode; PC: Polarization Controller; AOM: Acousto-optic Modulator. The details of each component are described in subsections.

4.2.1 Frequency Comb Source

CL-OCT only requires a continuous frequency source. Thus, the source complexity can be greatly reduced. For proof of principle demonstration, a simple ASE-filtered frequency combs source was built. Erbium-doped fiber amplifier (EDFA) was chosen as the gain medium for its high gain characteristic compared to semiconductor optical amplifiers (SOAs). In the first stage, a 7 m EDFA (M12-980-125, Fibercore, USA) was pumped by a high-power single-mode pump laser diode (LD) centered at 1480 nm (QFBGLD-1480-500, Qphotonics, USA) through the wavelength-division multiplexor (WDM) (1480-1550nm Micro-Optic Wavelength Division Multiplexer, AC Photonics Inc, USA). The Faraday rotator mirror (FRM) (AC Photonics, USA) was used to recycle counter-propagating ASE light and to

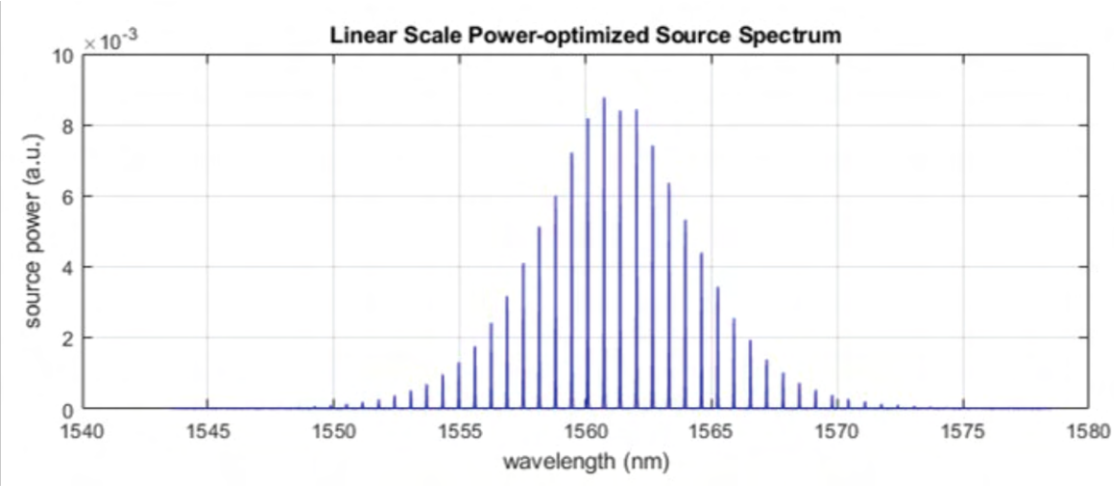

Figure 4.3: Output spectrum of the ASE-filtered frequency comb source.

shape the spectrum to be more Gaussian. The ASE light from the first EDFA is coupled into a free-space Fabry-Perot Etalon (FPE) (LightMachinery, Canada) with 100 finesse and 80 GHz FSR. This corresponds to the double-pass coherence length of 6 cm and FSR of approximately 1.9 mm in air. The output from the first amplifier stage is linearly polarized with a free-space polarization beam splitter (PBS) (PBS124, Thorlabs, USA) before coupling into the booster amplifier stage with a 14 m EDFA pumped by another 1480 nm pump LD. The two stages and pump LDs were optically isolated to eliminate parasitic lasing. An in-line polarizer (ACphotonics, USA) and a polarization controller (PC) (FPC030, Thorlabs, USA) were placed at the output of the booster stage to eliminate polarization mode dispersion (PMD). The output spectrum of the source is shown in Fig. 4.3, and the optimized average output power was 43 mW. The FWHM optical bandwidth of the source is 6.5 nm, corresponding to the axial resolution of 165 μm in air with 1561 nm center wavelength. The lateral resolution is more critical than the axial resolution for camera-like, single-depth imaging. Furthermore, the SNR for low axial resolution is higher than the SNR for high axial resolution in tissue. [47].

4.2.2 Interferometer and Microscope

The source was coupled to an MZI via a 90/10 directional coupler (Gould Fiber Optics, USA). In the reference arm, the beam was modulated at a 50 MHz frequency shift with the acousto-optic modulator (AOM) (Brimrose, USA). The interference fringe would be demodulated at this frequency, and the maximum frame rate was set to 50 fps assuming a 1000 px by 1000 px image. Reducing the image resolution could increase the framerate. The free-space motorized stage controlled the reference beam path. The beam was polarized at the input to the polarization diverse detector to eliminate PMD. In the sample arm, an identical AOM and PBS were inserted to minimize dispersion. The sample arm fiber length was also matched to the reference arm fiber length up to a 1 cm accuracy. The beam was delivered to the sample via a dual-axis scanning system composed of a fast-scanning 28-facet polygon mirror (Novanta Photonics, USA) and a slow-scanning galvanometer mirror (Thorlabs, USA). The backscattered sample light was coupled back in the illumination fiber. All of the electronics were synched with a 10 MHz reference clock from the master waveform generator (Moku:Lab, Liquid Instruments, USA).

A custom microscope capable of wide-field, video-rate imaging was built. Multiple designs were simulated with Zemax software (ZEMAX, USA) optimizing the FOV and the lateral resolution. One of the designs is shown in Fig. 4.4 (a). The working distance of the microscope was 12.8 cm with 4 cm by 4 cm FOV and 62 μm diffraction-limited spot size at the beam focus. The depth of focus defined by the twice Rayleigh range was approximately 4 mm in air. The fast-axis scan pivot was located at the back focal plane of the objective, resulting in a telecentric configuration, while the slow-axis pivot point was placed halfway between the back focal plane and the objective, resulting in an expanding beam as a function of depth. The slow-axis scan angle could be adjusted by altering the driver voltage. The microscope was built and experimentally validated, showing good agreement with the theory (see Fig. 4.4 (b)).

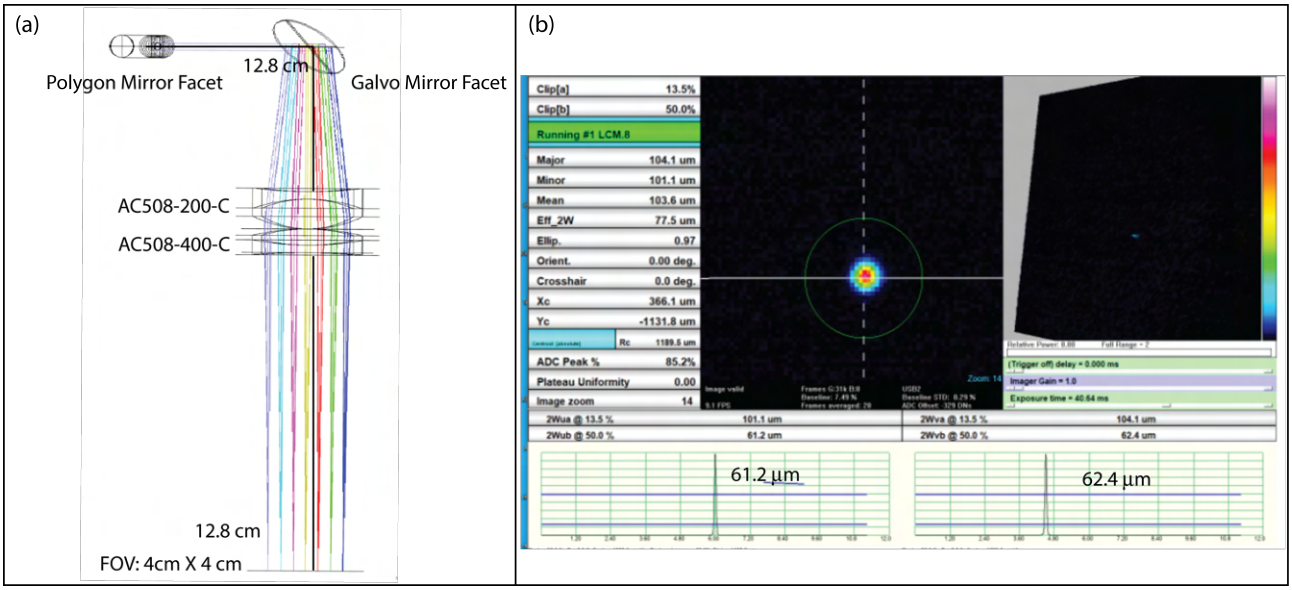

Figure 4.4: Characterizing microscope. (a) Zemax software simulation. The predicted field of view (FOV) at the focus was 4 cm by 4 cm with diffraction-limited resolution of 62 μm. (b) Experimental validation. The measured FWHM beam spot size was 62 μm in agreement with the prediction.

4.2.3 Signal Detection and Processing

A dual-balanced polarization diverse detector configuration was employed for measurement. Two balanced detectors (PDB460, Thorlabs, USA) with 200 MHz RF bandwidth were used. Even though the carrier frequency was 50 MHz, the signal was linearly chirped due to the polygon scanner. At the operational speed, the signal was chirped by about $\pm$ 25 MHz. To reject electronic noise between 80 MHz and 200 MHz, identical low-pass filters with 90 MHz cutoff (BLP-90+, Mini-Circuits, USA) frequency were inserted at the detectors. The digitizer (ATS9350, AlazarTech, USA) sampled the waveform at 409.6 MHz (integer multiple of the polygon drive frequency) and was triggered at the slow-axis scan rate.

Signal processing and data analysis were performed with custom MATLAB scripts. Let $f_H[n]$ and $f_V[n]$ be digitized fringe, containing the sample reflectivity information, from the H-BD and V-BD. For digital lock-in, the demodulation waveform was estimated from a fast-axis

scan. The in-phase and quadrature waveforms were generated and applied

$$C_{H/V} = h_{lpf} * f_{H/V}[n] cos[f_{mod}[n]] \tag{4.3}$$

$$S_{H/V} = h_{lpf} * f_{H/V}[n] sin[f_{mod}[n]] \tag{4.4}$$

where h_{lpf} is the digital low-pass filter for lock-in amplifier. The optimum filter cutoff frequency is the function of the system resolution and was determined experimentally to maximize SNR. The Stokes vectors were reconstructed as

$$I = |E_H|^2 + |E_V|^2 \tag{4.5}$$

$$Q = |E_H|^2 - |E_V|^2 \tag{4.6}$$

$$U = 2\mathcal{R}(E_H \tilde{E_V}) \tag{4.7}$$

$$V = -2\mathcal{I}(E_H \tilde{E_V}) \tag{4.8}$$

where

$$E_{H/V} = C_{H/V} + iS_{H/V} \tag{4.9}$$

One of the assumptions is that a single Stokes vector contains sufficient nerve information, which could be extracted by a machine learning algorithm (see future works).

4.3 System Characterization

4.3.1 Sensitivity Measurement

The system sensitivity was measured prior to imaging. First, the optimum reference arm power was determined by measuring the total noise power as a function of the reference arm power while blocking the sample arm. The result is shown in Fig. 4.5 (a). At low reference arm power, the electronic noise from the detector and the digitizer board dominated. As the reference power was increased, the noise power started to be optically dominated. Around -18 dBm, the total noise showed linear behavior consistent with the shot-noise curve, an ideal

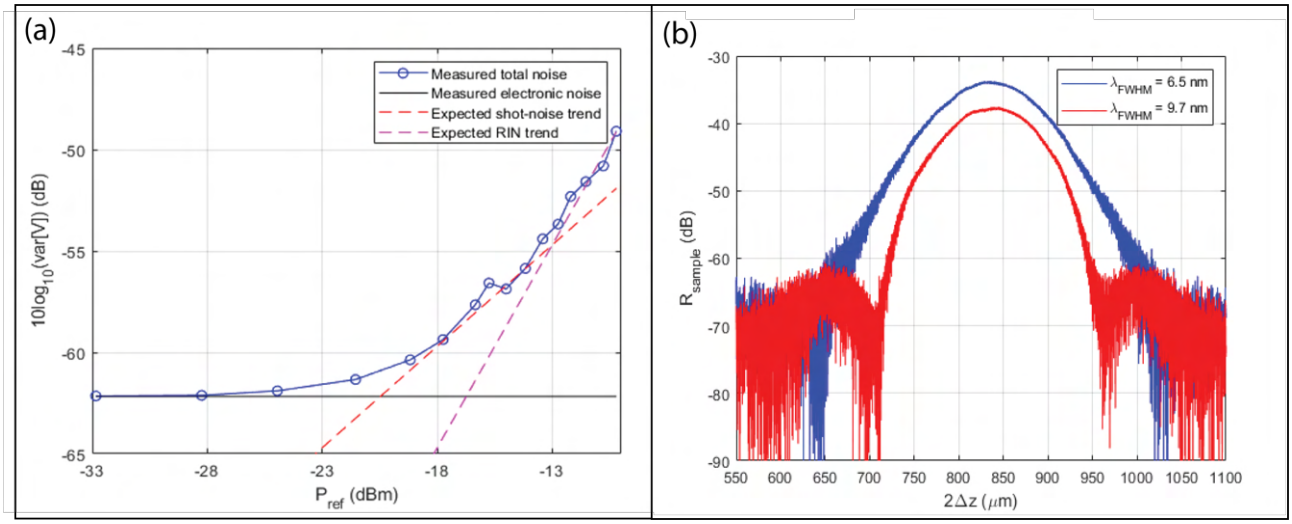

Figure 4.5: System sensitivity measurement. The optimum reference arm noise power is found to be about -18 dBm, or 20 μW from (a). (b) shows the source point spread function (PSF). Blue PSF shows the optimum PSF for imaging. Changing the polarization state after the source, the red PSF can be realized where higher resolution imaging is possible if the side-lobe is acceptable.

behavior. Past -15 dBm, the total noise started to follow the RIN curve. Therefore, the optimum reference power was approximately -17 dBm, or 20 μW. Then, the sample arm was opened, and a flat gold mirror was placed at the focal plane (PF10-03-M01, Thorlabs, USA). NF filters with -67.7 dB total attenuation were inserted between the mirror and the focusing optics. The data was acquired while the reference mirror was slowly being translated. Finally, the sample reflectivity was plotted as a function of distance. The reconstructed PSF is shown in Fig. 4.5 (b) as the blue curve (with digital low-pass filter cutoff set at 500 kHz). The SNR of the blue curve was approximately 35 dB. Thus, the system sensitivity was -102.7 dB. The double-pass resolution in air of the blue PSF was 165 μm. The red PSF shows another possible source state that achieves higher resolution (111 μm in the air) at the expense of the side lobe and 10 dB sensitivity penalty.

4.3.2 System Tolerance to Material Dispersion

The system's tolerance to material dispersion was characterized. The PSF was measured as a function of the number of 75 mm (length) by 25 mm (width) by 1 mm (depth) glass slides (S8902-1PAK, Millipore Sigma, USA) placed on top of the sample mirror. The slides were

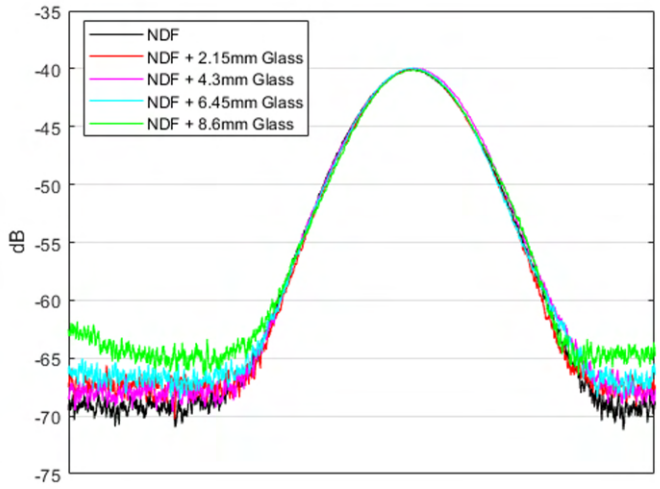

Figure 4.6: System tolerance to sample material dispersion. Glass slides of increasing thickness were added in the sample arm and psf measurements were performed. Psf remains unaltered even for 8.6 mm glass slides.

tilted to prevent strong specular reflection from saturating the detector. Fig. 4.6 shows the incoherently averaged PSF at varying glass slide thickness. No noticeable PSF change was observed, even at 8.6 mm. The side lobes are likely from the reflections from multiple glass boundaries. The narrow spectral bandwidth of the source leads to a high system tolerance for material dispersion.

4.3.3 System PMD

The degree of system PMD was qualitatively assessed by measuring the Stokes vector as the function of depth. If the system had a large amount of PMD, the Stokes vector would rotate, and the magnitude of the QUV would vary. To test, a set of mirror translation measurements was performed, each time varying the sample input polarization state. Fig. 4.7 shows the experimental data. In State 2, a slight sloping of the Q and V components was seen. However, this small amount of PMD would likely be inconsequential. Some states exhibited more obvious PMD effects than others, but none were concerning.

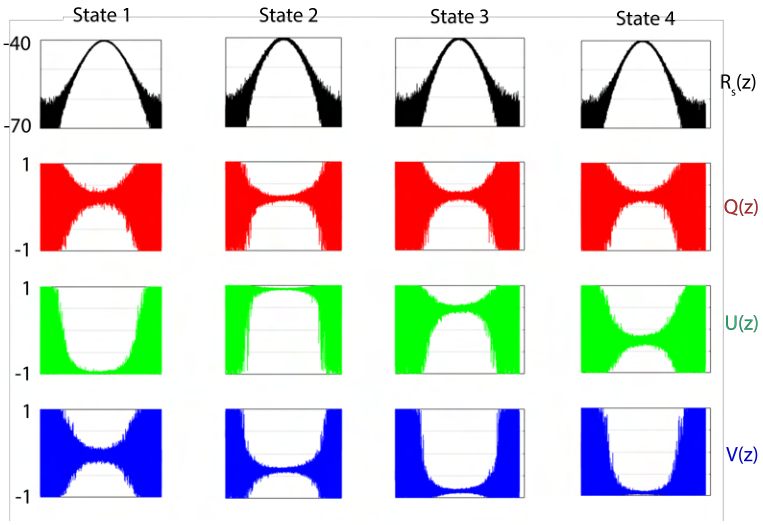

Figure 4.7: Assessing system PMD. Normalized Stokes vector components were plotted as a function of depth. Evidence of a minor PMD was observed as a slight sloping of the QUV. Likely, this amount of PMD is inconsequential.

4.4 Imaging

Video-rate, multi-cubic centimeter CL-OCT imaging was demonstrated with three different samples: an engineered structural phantom, a two-layer tape phantom, and an ex-vivo chicken nerve sample. The sample details are given in Fig. 4.8.

4.4.1 Spiral Phantom Imaging

The 3D-printed spiral phantom was imaged as a 3.1 mm diameter ceramic ball (McMaster-Carr, USA) rolled down the ramp. This imaging aimed to test whether the theoretical principle described in section 4.1 was sufficient to describe the acquired images. A select number of scan-frames are shown in Fig. 4.9. The frame size was 504 pixels by 504 pixels, and the data was acquired at 47 fps. The top row shows structural CL-OCT images. The green arrow points at the ceramic ball as it rolls down the ramp. The second and third rows show simulated images showing the ball's location in each frame. In frame 1, the CL-OCT image shows a concentric ring (green arrow). This corresponds to an optical sectioning of the ceramic ball shown in the third row. Even though the ball is larger than the separation between two adjacent depth slices, the second depth slice does not contribute to the image

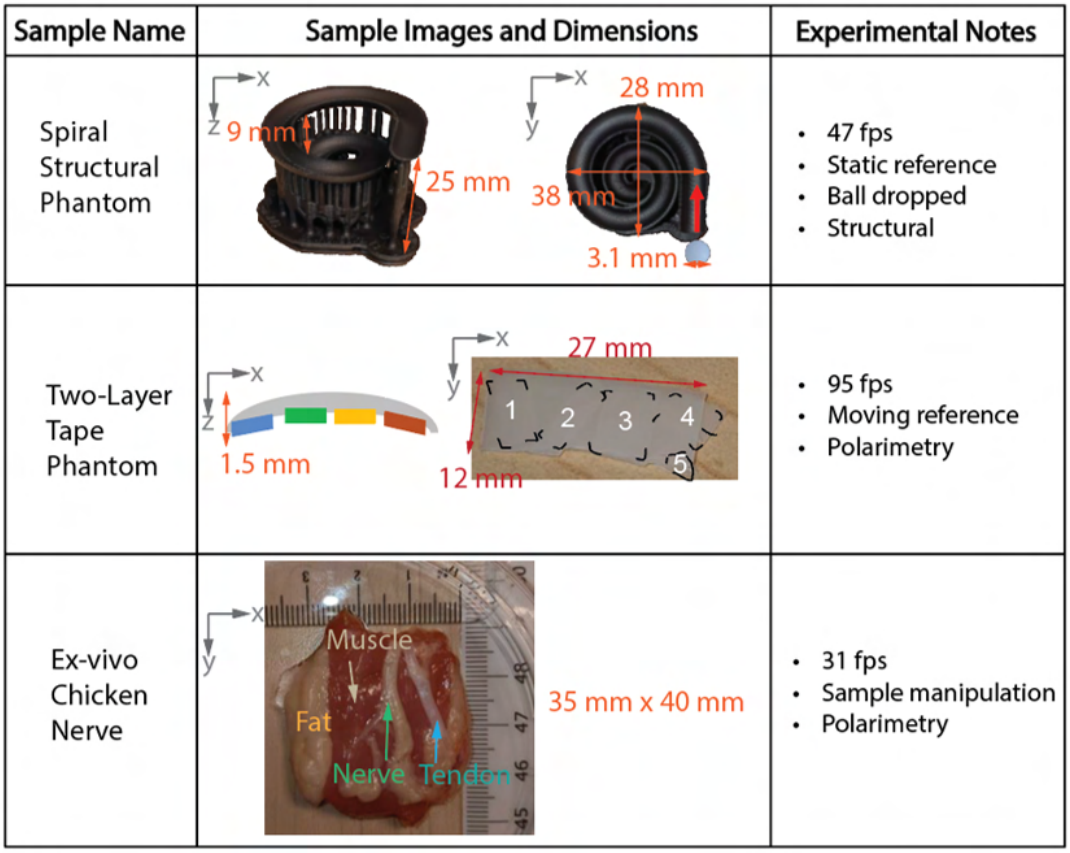

Figure 4.8: Samples used for CL-OCT imaging. The sample dimensions are given in the middle column and important experimental notes are provided in the last column. All of these samples meet the wide-field criteria set in Chapter 1.

due to attenuation and scattering. As the ball rolls down the ramp, a different depth slice of the ball is imaged. Frames 2 and 8 captured the same depth slice of the ball, though it had dropped by 1 FSR apart (1.9 mm), and the ball had traversed $\frac{\pi}{2}$ radians arc length. This is consistent with the expectation that full 2π radians arc length corresponds to a 9 mm drop. Thus, the theory was able to predict the system's behavior correctly. It is important to note that these CL-OCT images are fundamentally different from conventional camera images. In CL-OCT, the captured images are depth-resolved and have 3D tomographic information. In camera, however, the images contain only the surface information. For example, solid and hollow balls would appear identical in camera images, while they would appear distinguishable in CL-OCT images.

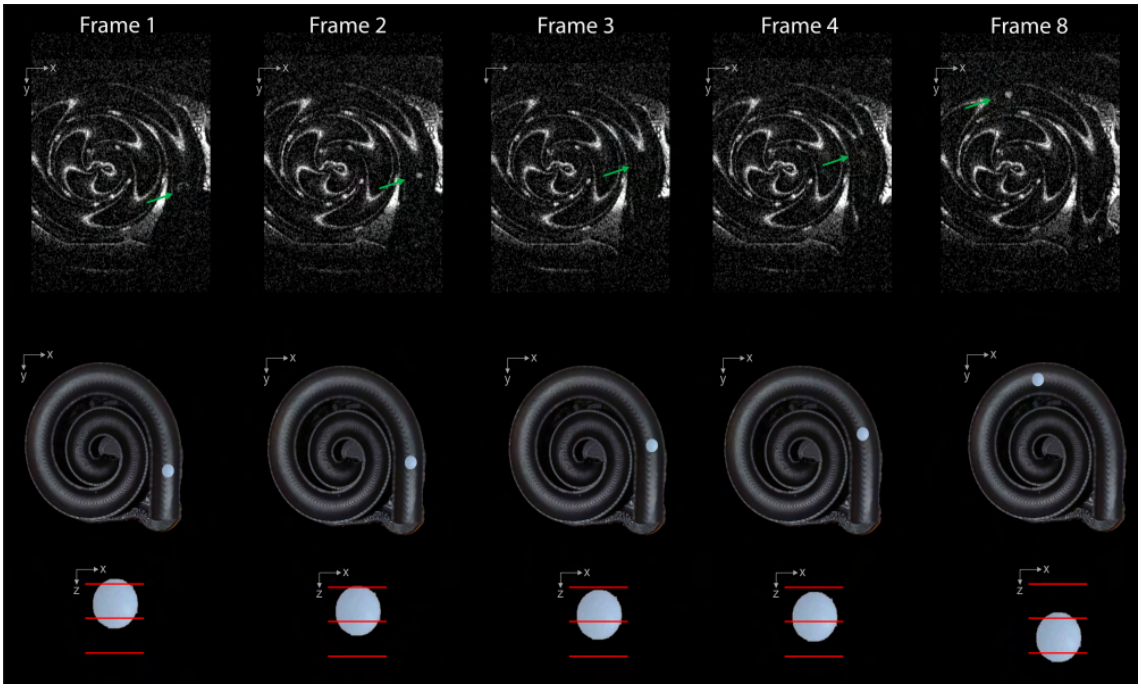

Figure 4.9: Snapshot of two-layer tape phantom imaging. (a) structural image, (b) corresponding colorized QUV image, and (c) colorized QUV images summed across 19 frames.

4.4.2 Two-layer Tape Phantom Imaging

Scotch tapes are birefringent and are ideal for testing polarimetric imaging systems. A 1.2 mm-thick two-layer tape phantom was made; each tape layer was 500 μm-thick but was slightly curved to reduce specular reflection. The first layer was made from a single strip of tape, so the Stokes vector rotates uniformly. On the other hand, the second layer was made from five different tape fragments with random orientation. Therefore, the Stokes vector rotates differently for each tape fragment. The phantom was imaged at 95 fps at 168 pixels by 504 pixels. To capture depth information, the reference mirror was translated at 9.5 mm/s (the full depth was covered in 19 frames). The imaging results are shown in Fig. 4.10. The imaging field included a half-inch ball to show the sample's relative scale and serve as a non-birefringent sample. Fig. 4.10 (a) shows the structural image of the phantom at a single frame. The corresponding polarimetric image is shown in (b). The QUV components were converted to RGB channels to generate the colorized map. The polarimetric image provides excellent contrast between different tissue fragments underneath the first tape layer. In particular, fragment 4 makes the contribution of the first layer on the Stokes vector rotation

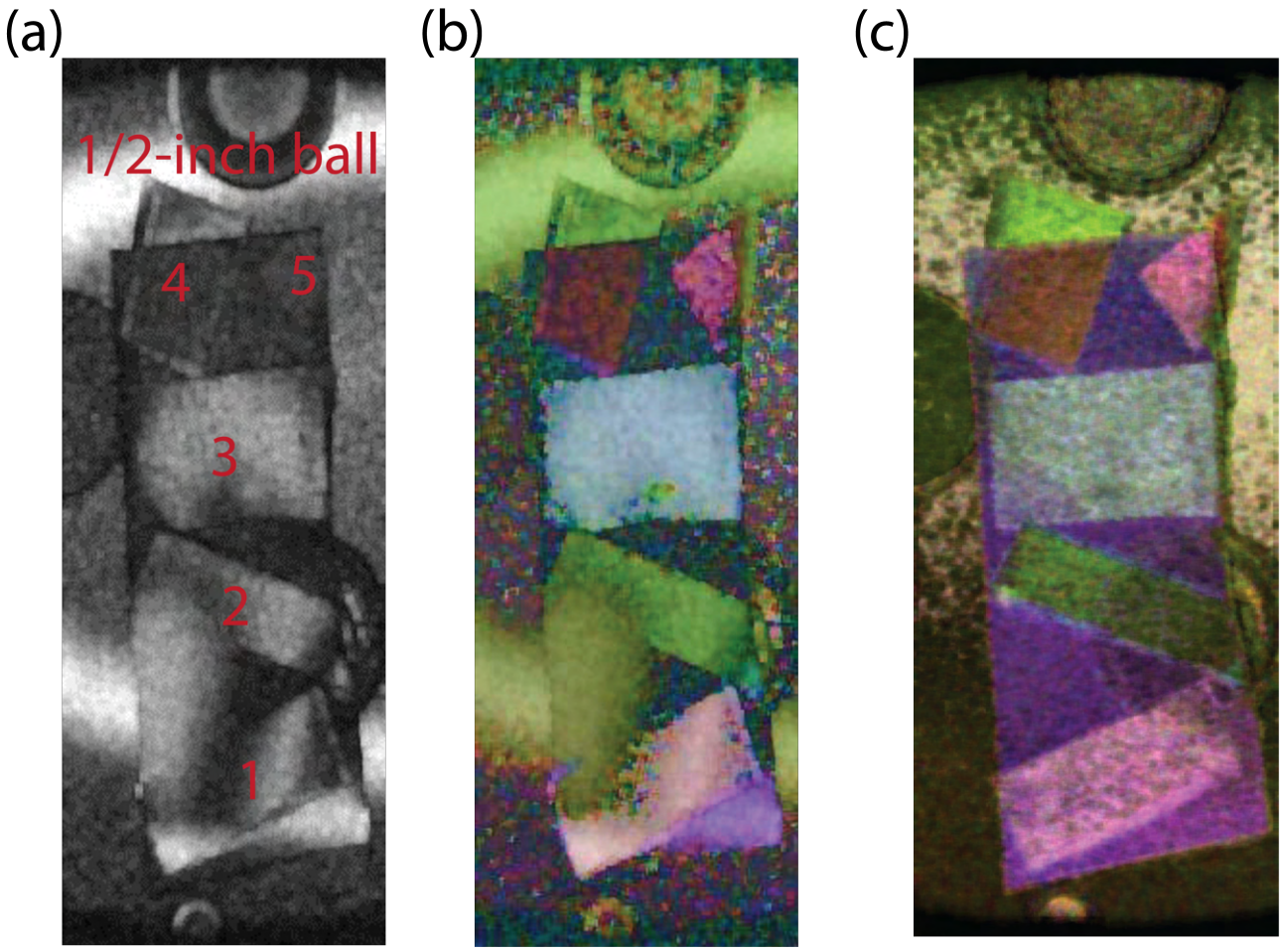

Figure 4.10: Snapshots of the spiral phantom imaging video. The first row shows the structural images, and the second shows simulated images corresponding to the CL-OCT image. The third row shows the relative height of the ceramic ball with respect to the optical sectioning.

obvious. All five fragments exhibited a unique color. The severity of PMD was assessed by summing 19 frames across depth (Fig. 4.10 (c)). All fragments showed consistent color without any abrupt changes. The results suggest that the polarimetric measurement is clean, and the system PMD is indeed inconsequential.

4.4.3 Ex-vivo Chicken Nerve Imaging

A test imaging with ex-vivo chicken nerve imaging was performed. A chicken thigh (Savenor's Butcher Shop and Market, USA) was dissected, and the neurovascular bundle (NVB) was exposed. The nerve was placed at the center of the FOV, and data was acquired as the

reference mirror translated at 3.1 mm/s (19 frames contained the full-depth information). During the acquisition, the nerve was manipulated with a surgical tweezer (TZ). Representative frames from the imaging are shown in Fig. 4.11. Multi-centimeter FOV was acquired even though the vertical field was limited by the lens aperture. The residual galvanometer mirror trace was also noted. In frame 43, the ST approached the nerve from the bottom of the image. The nerve was pinched (frame 61) and pulled (frame 85). The unique nerve feature is visible in the colorized Stokes vector images. The band of Fontana was slightly blurred, but still visible at this resolution. Similar to the two-layer phantom, 19 frames were summed, as shown in the figure. This image was much more rich in contrast compared to a single frame Stokes vector.

4.5 Summary

In this Chapter, CL-OCT was presented as a promising solution to overcome the data capture bandwidth and system complexity problems. This approach is compatible with endoscopic cameras. Combined with the high-power amplifier strategy in Chapter 3, a scanning-less system can be developed for full-field imaging, overcoming the beam scanning problem detrimental to endoscopic probe applications (section 1.3.3). The future works involve training a custom, machine learning model for real-time nerve identification. Since CL-OCT outputs streams of camera-like images, surgeons do not have to relearn a novel imaging tool, which also helps with the volumetric data visualization problem and clinical translation (section 1.3.4). This technology, if successfully translated, may lead to a lower incidence of iatrogenic nerve injury.

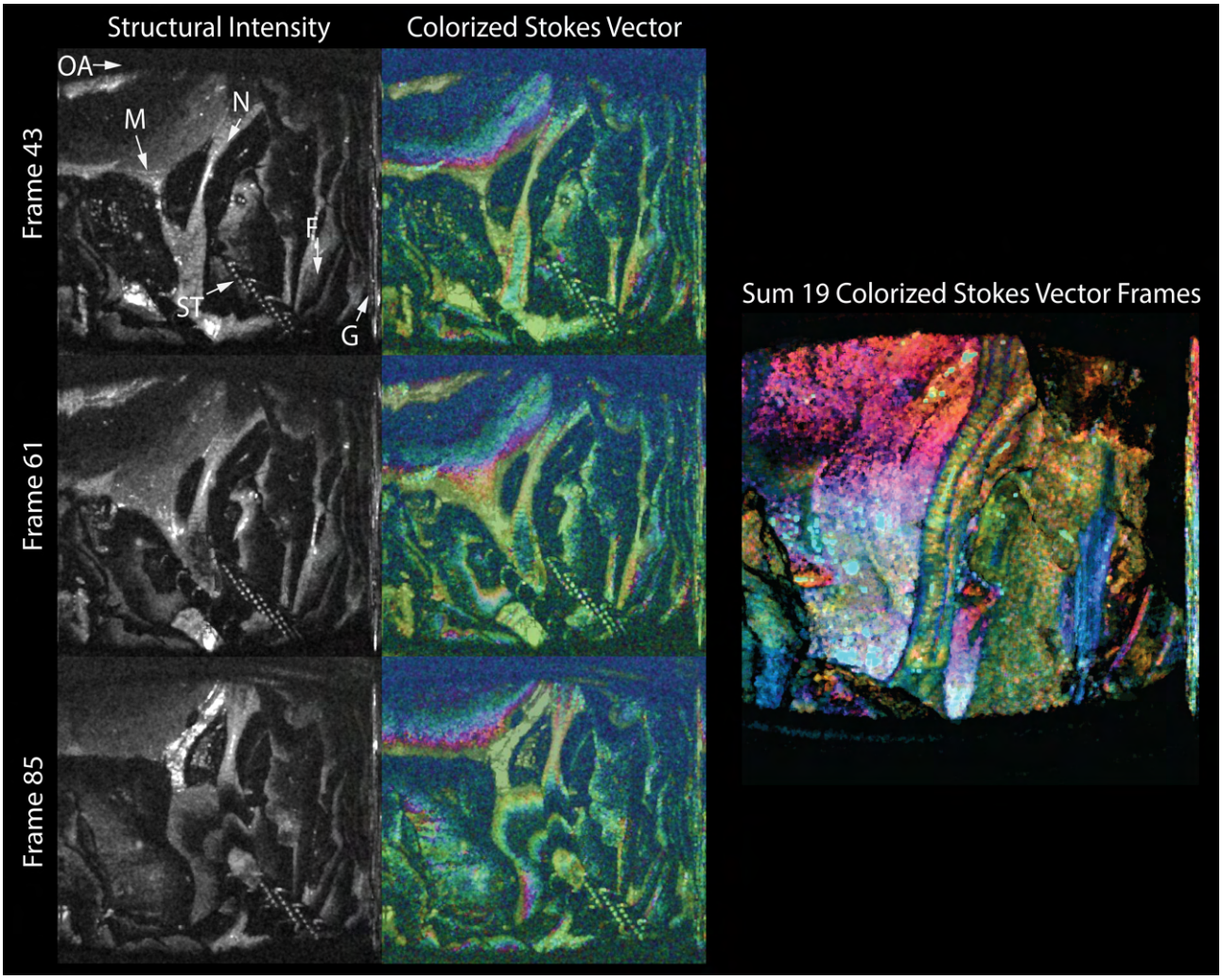

Figure 4.11: Snapshots of the ex-vivo chicken nerve imaging. The exposed nerve was manipulated during the data acquisition. OA: Regions of clipping due to the objective aperture; N: Nerve; M: Muscle; F: Fascia; ST: Surgical Tweezer; G: Galvanometer mirror. The structural and colorized Stokes vector images are from the same frame number. Summed colorized Stokes vector image was even more rich in contrast.

Chapter 5

Ex-vivo Vagus Nerve (VN) Fascicle Imaging

This Chapter provides a rationale for developing a surgical OCT system for imaging the Vagus nerve (VN). The preliminary study was conducted with a conventional PS-OCT system to establish OCT as a useful tool for this particular imaging sample. The clinical significance of the Vagus nerve imaging was introduced and a custom PS-OCT system for imaging ex-vivo VN samples was developed. The results presented here suggest that a surgical OCT system to image in-vivo VN will have clinical value.

5.1 Introduction

Vagus nerve stimulation (VNS) therapy is an FDA-approved therapy for refractory and focal epilepsy, and its scope of application has expanded to include treatment for depression and stroke rehabilitation [48][49][50]. However, the vagus nerve (VN) contains motor, parasympathetic efferent, and sensory afferent nerve fibers, and existing vagus nerve stimulation (VNS) devices tend to activate them all. As such, it can be challenging to achieve a therapeutic result without excessive side effects [51]. This has motivated efforts to develop novel stimulators capable of selective excitation, often by delivering a localized rather than wide-area stimulation field [52][53]. To design these stimulators, it is essential that we un-

derstand vagus nerve (VN) anatomy, including population variations [54][55][56]. Ex vivo imaging is an obvious strategy to investigate VN anatomy, but few imaging tools can provide micrometer-scale resolution and high fascicle contrast. Conventional imaging tools are also restricted to short nerve segments, which limits their capability to trace nerves through their natural contours and connections, an important requirement of peripheral nerve imaging [55].

Histology is the gold standard for VN imaging. It offers high-resolution and strong fascicle contrast. However, it does not scale favorably to large tissue specimens, and it is time-consuming and resource intensive. Alternatively, Chaitanya et al. applied slide-free microscopy with ultraviolet surface excitation (MUSE) to image fascicles with a resolution and contrast sufficient to see individual axons [57]. However, MUSE requires fluorescence labeling, and the imaging time is not significantly reduced compared to histology since it is a surface sectioning method. Thompson et al. optimized a micro-CT protocol by replacing toxic osmium staining with Lugol's iodine. They imaged a 4-cm segment of a porcine cervical VN with 1-13 days of staining. The protocol considerably reduced imaging time at the expense of degraded contrast compared to histology and MUSE [58]. However, the protocol was hindered by motion artifacts and contrast agent-induced tissue degradations. Finally, Settell et al. demonstrated real-time in vivo ultrasound imaging of porcine VN, showing cross-sectional videos of the coarse fascicular groupings [59]. While this label-free method rapidly scanned the VN with an on-demand approach, it resolved only larger fascicular groups with limited contrast and resolution.

Optical coherence tomography (OCT) has been applied to peripheral nerve imaging in a small number of studies. Early studies used conventional OCT, which derives contrast from light backscattered from tissue [60]. This conventional approach offered modest contrast for fascicles. More recently, polarization-sensitive (PS) OCT techniques that measure tissue optical birefringence have been applied to nerve imaging [61][62]. Nam et al. demonstrated high contrast between fascicles and epineurium in PS-OCT due to the orthogonality of the birefringent axes of myelinated fascicles and epineurium. In addition, the magnitude of retardance helps to differentiate between myelinated and unmyelinated fascicles [30]

[63][31][64][65]. However, while PS-OCT has only begun to be applied to large animal VNs, it has not yet been used as a tool for mapping fascicular anatomy, nor has it been used in human peripheral nerve imaging [32].

Here, we demonstrate a customized PS-OCT system and microscope designed for full-thickness, multi-centimeter-long VN fascicle imaging. The PS-OCT system included a dual-sided microscope to allow nearly simultaneous imaging from opposing sides of a nerve sample, thereby doubling imaging penetration depth relative to single-sided imaging. In addition, nerve-specific polarimetric processing algorithms were developed to enhance fascicle contrast relative to that achieved using generic PS processing algorithms. In addition to acquiring information on fascicular organization, we also provide preliminary evidence suggesting that the tool can be used to discriminate between highly myelinated and minimally myelinated fascicles, a capability micro-CT or ultrasound cannot provide. This could help track fascicles destined for abdominal branches as they have low to no myelination [66]. Because PS-OCT requires no contrast agents, lengthy sample preparation and staining times are obviated. The high speed of PS-OCT allows volumetric imaging of these multi-centimeter lengths in minutes, orders of magnitude faster than any existing high-resolution imaging modalities. Our approach enables VN imaging with spatial resolution and contrast sufficient for revealing the full nerve cross-sectional fascicular organization. The results suggest the potential for PS-OCT to complement existing imaging tools in the study of nerve anatomy and support neurostimulation research and translation.

5.2 Materials and Methods

5.2.1 PS-OCT Imaging System

A custom-designed PS-OCT system was built and optimized for multi-centimeter imaging (Fig. 5.1). A near-infrared (1310 nm) swept-source laser with 110 nm bandwidth (HSL-200-50LC, Santec Corp., Japan) was used for illumination. The axial resolution was estimated

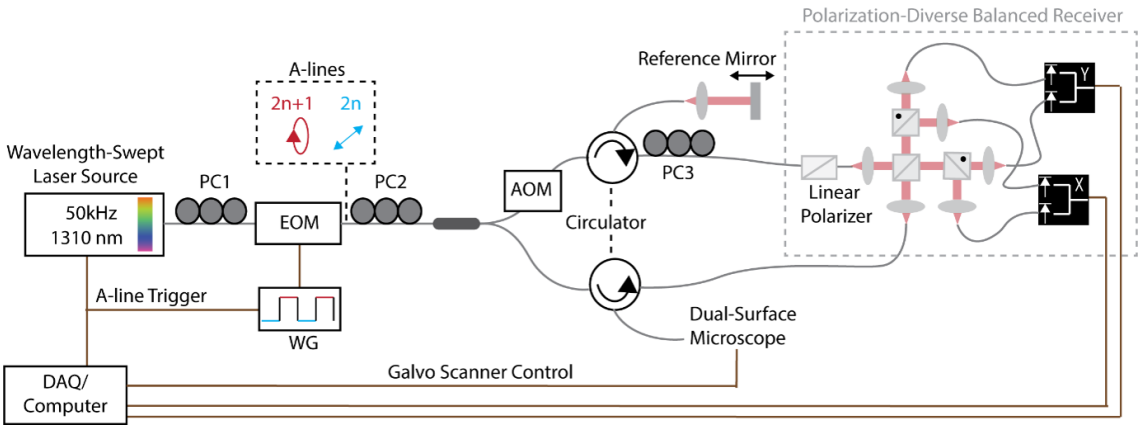

Figure 5.1: The custom PS-OCT system used for VN imaging. PC: polarization controller; EOM: electro-optic modulator; WG: waveform generator; AOM; acousto-optic modulator. The details of the sample microscope are shown in Fig. 2. The sample intensity, birefringence, and optic axis orientation were reconstructed from the volumetric image acquisition.

based on the spectral bandwidth to be 7 µm (in air). To ensure a robust polarimetry measurement, an electro-optical modulator (Boston Applied Technologies, United States) was used to rotate the source output polarization state between vertical and left-hand circular. This switching was performed between successive A-lines following previously described techniques [67]. The polarization-diverse receiver separated the backscattered light into orthogonal (Vertical and Horizontal) receiver channels. A linear polarizer was placed at the end of the reference arm to remove wavelength-dependent polarization rotations induced by polarization-mode dispersion (PMD).

A three-dimensional tomogram was generated by simultaneously scanning the galvanometric mirror across the nerve and translating the linear motorized stage along the longitudinal axis of the nerve (See 2.3 and 2.4 below for more details). Henceforth, the depth, lateral, and longitudinal directions are defined as the z, x, and y axes, respectively.

5.2.2 VN Sample Collection and Preparation

Cervical VN samples were dissected from a female adult Yorkshire swine weighing 50 kg (n = 2) following euthanasia. The samples were imaged fresh and after fixation. Fixation was performed by placing the compressed nerve in neutral buffered formalin (NBF) (10%) with

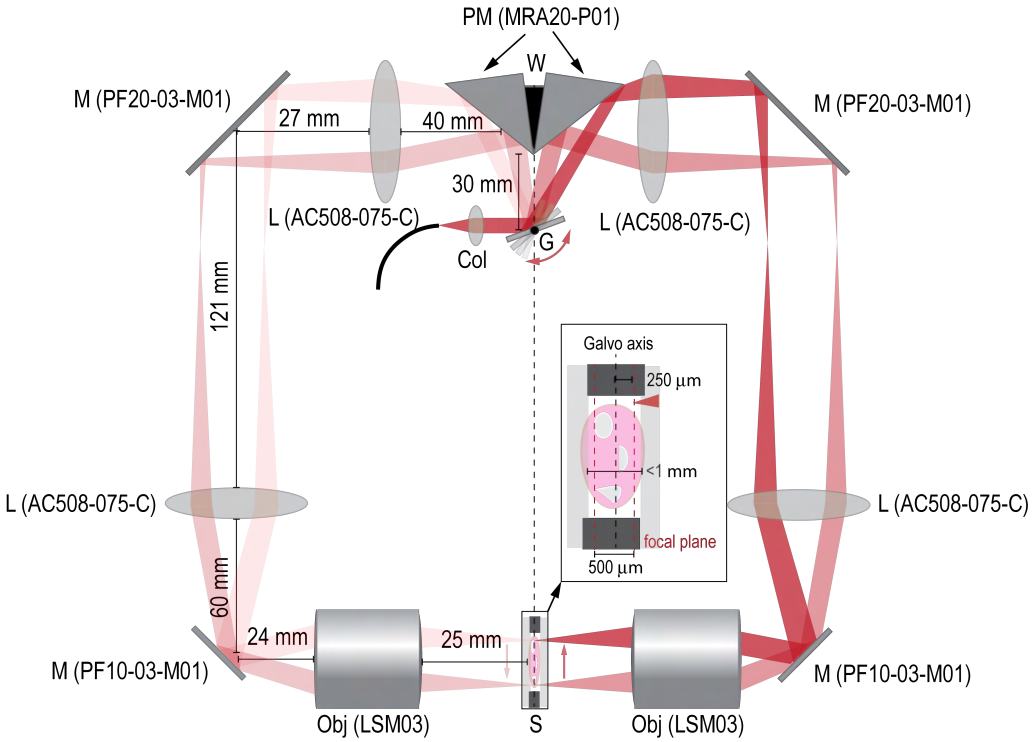

Figure 5.2: A dual-surface scanning microscope for full-depth VN imaging. The dotted line shows the plane of symmetry of the microscope: Col: collimator, G: Galvanometer mirror; W: 3D-printed wedge; PM: prism mirror; L: achromatic lens; M: mirror; MO; microscope objective; S: the sample specimen. Two sample cross-section images were acquired for each ramp scan.

the glass slides. Once fixed, the samples could be repeatedly imaged.

5.2.3 Dual-surface Scanning Microscope

The imaging penetration depth for highly scattering nerves is $\sim$ 1 mm. A dual-surface scanning microscope was built to support deeper imaging in these ex vivo samples (Fig. 5.2). The telescope was designed using Zemax software (ZEMAX LLC, USA) to optimize imaging resolution. The objective lens (LSM03 Scan Lens, Thorlabs, USA) yielded a diffraction-limited focal spot size between 15 and 30 µm, depending on the collimated beam diameter.

The beam remained focused across a 5 mm field of view (by Zemax simulation). To minimize aberrations, a pair of 2" achromatic doublet lenses (AC508-075-C, Thorlabs, USA) and a 2-inch mirror (PF20-03-M01, Thorlabs, USA) were used to relay the collimated beam to the sample with unity magnification (f-f arrangement). The focal plane of each objective lens was set to have an offset of 250 µm relative to the galvanometer mirror's pivot point. This ensured the contralateral focal planes were offset by 500 µm, approximately twice the computed Rayleigh range in tissue. A custom wedge (W) was 3D-printed to tilt the right-angle prism mirror (MRA20-P01, Thorlabs, USA) by an additional 1.8 degrees, ensuring the beam's principal ray passed through the telescope's optical axis. With continuous scanning by the galvanometer mirror, the microscope acquired images of the VN from both surfaces (i.e., each surface on one side of the B-scan image).

5.2.4 Experimental Design and Imaging Protocol

The experimental imaging setup is shown in Fig. 5.3. The gently compressed porcine VN was placed between two 75 mm by 25 mm by 1 mm glass slides to create a 650- µm thick enclosure with a 7-mm wide channel. The nerve was then compressed with a second glass slide to force the nerve to lie within the 650 µm x 7 mm channel. An aqueous solution with 98% glycerol (Sigma Aldrich, USA) was added before nerve compression for index-matching. The confined nerve sample was secured by a 3D-printed custom holder for imaging.

Once secured, the sample was placed on the linear motorized stage and aligned to minimize focal plane walk-off during translation. The entire microscope head was mounted with a slight tilt to reduce specular reflection from the glass-air interface. For all the experiments, the motorized translation speed was set to 0.1 mm/s. The galvanometer was driven such that 2048 A-lines were acquired in a single linear ramp scan, which constitutes an image frame (B-scan) containing sub-images from both opposing surfaces. The protocol used ∼4x over-sampling of the optical resolution in the longitudinal (slow-axis) direction for a ∼4 µm/frame step size. The nerves were sampled along the fast-axis with a step of ∼7 µm/A-line. A total of 16384 frames (6.8 cm) were imaged, which took ∼12 minutes.

5.2.5 Data Processing and Visualization

The processing workflow is outlined in Fig. 5.4. Four algorithms (denoted by a red dotted box) were used to generate the merged, fascicle-enhanced images.

1: Core PS-OCT Processing Algorithm

The core algorithm takes the raw spectral data as input and performs background subtraction and numerical dispersion compensation. The processed fringes are fed to the spectral binning algorithm for PMD mitigation, whose details are described elsewhere [68]. For both samples, the number of spectral bins (N), dz offset, and degree of polarization uniformity (DOPU) threshold were set to 5, 2 pixels, and 0.75, respectively. The Stokes averaging filter was set to preferentially average along the nerve longitudinal axis (slowly scanned axis) to take advantage of the slowly changing fascicle geometry along this axis and to preserve lateral and axial resolution. The spectral binning algorithm outputs volumetric images of structural intensity, retardance (in degrees/µm), and optic axis (OA) orientation with respect to a reference angle ($\in [-90^o, 90^o]$) mapped to hue-saturation-value (HSV) color space). Since the absolute retardance and OA orientation were not critical for this study, an arbitrary reference angle was chosen, and the retardance was scaled to increase contrast without loss of information. The Python code of this algorithm is publicly available from our group's GitHub repository [25]. The nerve images were then input to the application-specific processing pipeline, which includes the Geometric Correction Algorithm, the Fascicle Segmentation Algorithm, and the Surface Merging Algorithm. Custom MATLAB scripts were written for those algorithms.

2: Surface Registration Algorithm

The set of transformations to register to the two surfaces in preparation for merging was determined following the seven steps outlined in Fig. 5.5. The input images for this process were generated by applying a median filter to the structural images along the longitudinal axis (15 frames).

1. **Find curvature correction vector**: A vector was found to correct the lens-induced group phase delay. The filtered structural images were split into two surfaces of equal size (nominally denoted as surface A in red and surface B in blue). For each surface, a test image was chosen. We selected seven arbitrary points along the curved glass slide-sample boundary. These points were interpolated to generate the curvature correction vector.

2. **Apply the curvature correction vector**: The correction vector was applied to the rest of the frames.

3. **Find the first transformation parameters from depth-summed images**: The transformation necessary to register the two surfaces in the en-face view was determined. Two en-face images were generated by summing the curvature-corrected images (from Step 2) across depth. One of the images was fixed, while the other underwent user-specified 2D transformations. This process was repeated until the fused image showed qualitatively good registration. For one sample, the optimum x- and y- translations were 570 pixels and 5 pixels, respectively.

4. **Apply the first transformation**: The first transformation was applied to the curvature-corrected structural images.

5. **Find the second transformation parameters from width-summed images**: The transformation necessary to register the two surfaces in the parasagittal view was determined. Two sagittal images were generated by summing the transformed images across the width. The optimum transformation was determined in Step 3. For one sample, the z-translation of 17 pixels and the rotation of 0.07 degrees about the center of the image yielded the best result.

6. **Apply the second transformation**: The second transformation was applied to the curvature-corrected transformed structural images.

7. **Find the final transformation parameters for each cross-sectional image**: Every 500th cross-sectional image from each surface was fused together to assess the registration quality. Fig. 5.5 shows an example frame. Some images required no corrective transformation, while others required a small amount of additional x-translation, less than 1% of the image width. These values were interpolated between the sample's initial and end frames.

3: Fascicle Segmentation Algorithm

The algorithm sought to maximize the fascicle signal and minimize the background signal from other tissue types in the OA images. For simplicity, only three tissue types were assumed to exist in the image: fascicle, epineurium, and adipose tissue. The distribution of optic axis data for these three tissues is shown in Fig. 5.6, along with a region-of-interest (ROI) containing a mixture of epineurium and fascicle. While the HSV color wheel range is between 0 to 2π radians, the physical OA orientation spans from 0 to π radians. Here, the physical angle is used; thus, the 2π radians is mapped to π radians. The first quadrant corresponds to 0 to $\pi/4$ radians, the second quadrant corresponds to $\pi/4$ to $\pi/2$ and so forth. The OA orientation distribution was calculated over an ROI of 7 (transverse) by 7 (axial) by 51 (longitudinal) voxels. Note the orthogonality between the epineurium and the fascicle. However, adipose tissue was observed to be a potent OA scrambler. The fascicle and adipose tissue histograms overlapped, making a simple segmentation algorithm prohibitive. To circumvent this problem, we developed a two-step segmentation algorithm.

1. **Adipose Removal Algorithm**: Fig. 5.6 shows that the epineurium OA orientation and the fascicle OA orientation were $\pi/2$ radians apart to a good approximation, while adipose tissue OA orientation was distributed more randomly between 0 and π radians. These statistical differences between tissue types could be exploited to preferentially mask voxels with high adipose tissue contents. First, the mean fascicle OA orientation was calculated from the fascicle ROI. Then, the mean fascicle OA orientation was rotated to be at $\pi/8$. The histogram from other mixtures of tissue types was also rotated by the same amount. Next, a dot product between the x and y components

of vectors comprising the polar histogram was computed. Since the epineurium and the fascicles were orthogonal and lie in either the first quadrant (from 0 to $\pi/4$) or the third quadrant (from $\pi/2$ to 3 $\pi/4$) the dot product would yield a large positive number. Conversely, an adipose-laden histogram would yield a very small or negative number. This operation was performed on each OA voxel. The result was input to a logistic function with an arbitrary scaling factor such that the output values range between 0 and 1, where 1 means a high chance of adipose signal. Conceptually, this can be thought of as the likelihood that the voxel contains adipose tissue. Voxels with a greater than 10% chance were thresholded. A hole-filling algorithm was applied to the binary mask to increase the robustness of the thresholding. The intermediate images are shown in rows 1-3 in Fig. 5.7.

2. **Fascicle Contrast Enhancement Algorithm** : In step 2 (fascicle contrast enhancement), all voxels are passed through a scaled cosine function such that the output yields a number between 0 and 255, where the maximum value corresponds to the fascicle signal (see Appendix C for more details). The resulting images can be considered a fascicle likelihood map. Sample images are shown in Fig. 5.7, row 4. A threshold was applied to segment epineurium voxels, yielding images containing fascicles only. The residual epineurium voxels and adipose tissue voxels were suppressed by applying a 2 (axial) $\times$ 2 (transverse) $\times$ 12 (longitudinal) median filter before merging surface A and surface B.

4: Surface Merging Algorithm

Surfaces A and B were registered with the geometric transformation parameters found previously. To merge and blend the transformed images, the following operations were performed for each frame: (1) set up a zero matrix with a size equal to the frame. (2) copy the upper (lower) half of the surface image A (B) to the corresponding element of the zero matrix. (3) Smoothen the image boundary with a blending function. A monotonically decreasing linear function was used to blend the boundary. Five pixels above and below the boundary line were replaced by the weighted average of the contrast-enhanced image values.

5.3 Results

5.3.1 Multi-centimeter Volumetric VN Fascicle PS-OCT Imaging

We imaged porcine cervical VN (Fig. 5.8, where orange boxes denote sample A and red boxes denote sample B). The total imaging time was less than 30 minutes for each sample, including the time needed to align the sample to the direction of the linear translation axis. The acquired data were processed and merged following the pipeline in Fig. 5.4.

Cross-sectional images of the merged fascicle are shown in Fig. 5.8 (b). The images did not show any noticeable fascicle discontinuity, shearing, or scaling between the two stitched surfaces, validating the performance of the registration algorithm. The fascicle morphology and size for the gently compressed PS-OCT images approximately matched the representative cervical VN histology in Fig. 5.8 (a). Sample A and sample B contained approximately 52 and 39 resolvable fascicles, respectively. In sample A, a group of fascicles appeared to have split off from the main trunk and were surrounded by a dense layer of adipose tissue.

Enface images extracted from the fully segmented PS-OCT volumes are shown in Fig. 5.8 (c). Two images were generated for each sample, one with the maximum decay curve applied to the nominal top surface (dotted horizontal line in the cross-sectional image) and the other with a reversed decay profile. Fascicles in sample A appeared less distinct compared to sample B due to higher fascicle density and reduced field of view. Correct focus is indicated by the relative diameter of the fascicles and their appearance in cross-section. The fascicles demonstrated varying degrees of contortion, convergence (merging and splitting). Both samples contained a 1-centimeter segment of increased contortion denoted by S in Fig. 5.8 (c). A fascicle traversing the entire width of the VN was denoted by a double star. These fascicles tended to have small diameters (20-40 µm) compared to others that did not have many contortions. The merging and splitting of fascicles was seen at various positions throughout the sample. To illustrate, one fascicle denoted by '*' in sample B merged and split over a length of $\sim$ 8 mm.

5.3.2 VN Fascicle Myelination Assessment with PS-OCT

A typical cervical porcine VN contains fascicles with varying numbers and sizes of myelinated axons (Fig. 5.9). Settel et al. have shown clear bimodal groupings of fascicles with lesser and greater degrees of myelination, corresponding to the bimodal organization of the afferent and efferent fibers. Directional or fascicle OA orientation-weighted retardance images were evaluated for their proximate resemblance to the observed bimodal distribution of the density of myelinated fibers. To preserve all relevant features, adipose tissue masks were not applied before merging. Even without the adipose mask, sufficient suppression of adipose tissue noise was achieved due to the quasi-random OA orientation.

A 1.8 cm segment of sample B was interrogated to determine if evidence of myelination changes could be detected (Fig. 5.10). The cross-sectional images of directional retardance demonstrated a qualitative correspondence to the expected distribution of myelinated axons. Furthermore, the PS-OCT system allowed volumetric fascicle tracking of the highly myelinated fascicle (orange arrow). Noteworthy morphological features besides the axonal propagation of the fascicle were denoted by the yellow feature arrow(s) in each frame. Resolvable merging and splitting features occurred approximately at 5 mm intervals between (a) and (f) and at approximately 1 mm intervals towards the distal part of the segment between (f) and (j). In particular, a local increase in the directional retardance was observed between (d) and (e) as a highly retarding group of axons branched and merged with a fascicle with a low level of myelination. Interestingly, as the adipose tissue on the left of the main trunk in (e) decreased, the relative degree of myelination of fascicles adjacent to the adipose tissue increased (f). The full-length cross-sectional fly-through movie is also available, though not included in the thesis.

5.4 Discussion and Conclusion

VNS therapy development can benefit greatly from a detailed anatomical and functional map of fascicular organization. The NIH SPARC (Stimulating Peripheral Activity to Relieve Con-

ditions) program drove this initiative, including a concerted effort to map 100 human VN samples from end-organ to mandible to capture the variability from subject to subject that may impact the therapeutic window (this work was supported by SPARC2 focused on technologies to understand the control of organ function by the peripheral nervous system). A high-resolution ex vivo imaging modality with fascicle-specific contrast is critical to achieving this goal. Ideally, the imaging time should be reasonably short to enable the interrogation of a large number of nerve samples in a reasonable time frame (i.e., withmoderate throughput). This work (i) demonstrates a method to overcome the limited penetration depth of PS-OCT through a dual-scanning microscope and application-specific processing, (ii) demonstrates that PS-OCT provides sufficient resolution, fascicle contrast, and imaging speed to visualize fascicular anatomy for nerve segments >1 cm, and (iii) suggests that PS-OCT can differentiate fascicle myelination based upon unique polarimetry contrast. These capabilities are achieved without labels or stains, a significant advantage over micro-CT, given that the toxic osmium stain requires a dedicated infrastructure for chemical management.

The final merged fascicle images and directional birefringence showed features consistent with reports from existing literature. The coarse fascicle morphology and organization, such as the size, shape, and distribution, matched with representative histology in the cervical porcine VN (Fig. 5.8). The approximate number of fascicles observed was within the range reported by Stakenborg et al., 46±10 fascicles for cervical porcine VN [69]. An observation relevant to the clinical end goal is that the fascicles naturally run in a moderately tortuous trajectory and frequently merge and split, as quantified previously by Upadhye et al. [55]. To estimate which nerve fibers have been activated, the conduction velocity is typically calculated based on the interpretation of evoked compound action potential recordings during VNS. This model assumes that fibers run in a straight line [63][53]. Thus, the estimation may be inaccurate when fascicles exhibit a high level of tortuosity. Finally, the directional retardance images show coarse features that approximate the bimodal organization of fascicle groups in terms of a high and low degree of myelination, previously reported by Settell et al. [54][59] based on histological and ultrasound studies (myelination was only visible in histology, not on ultrasound). The ability to quantify the degree of myelination without

labeling has not been reported by micro-CT and MUSE-based imaging.

Despite these promising results, PS-OCT has several limitations. Scattering fundamentally limits this approach to a few mm, even with our dual-sided microscope design. The technique required gentle compression of the VN to limit physical thickness. This, however, may cause fascicles to reorganize relative to their in vivo state. The influence of mechanical compression on the VN imaging properties, such as retardance, is unknown and should be characterized to further advance the tool toward an absolute measurement of myelination. Finally, the method relies on the orthogonality between the epineurium OA orientation and the fascicle OA orientation to achieve label-free fascicle contrast. Since the lipids in the myelinated axon are the dominant source of form birefringence, the unmyelinated axons would have inverted optic axes relative to the myelinated axons [29][70][71]. It is possible that this could diminish the fascicle contrast or entirely miss fascicles in the abdominal VN containing many unmyelinated fascicles [69].

Future studies should include quantifying the correlation between the directional birefringence and the degree of myelination. The entire VN, including the abdominal segment, should be imaged with matched histology slides to determine whether sufficient fascicle contrast exists for unmyelinated fascicles. Imaging longer VN samples requires a longer sample chamber, extended translation stages, and a more effective means of centering the sample along the focal plane. In the future, a hardware solution like a custom phase mask could be implemented to homogenize the beam diameter across depth to maintain uniform lateral resolution [72]. Because human VNs have a smaller number of fascicles and reduced adipose tissue content compared to the porcine VN [69][73], it is likely that image quality of PS-OCT applied ot human samples will be higher than that of porcine samples. Finally, since this is a label-free imaging technique, a high-speed PS-OCT system could be combined with multi-surface imaging used for in vivo imaging. Saytashev et al. demonstrated increased imaging depth by using side-view prism mirrors [32]. Ultimately, this approach could be extended to achieve a CT-like cross-sectional imaging for in vivo monitoring during VNS implantation and stimulation field optimization [74].

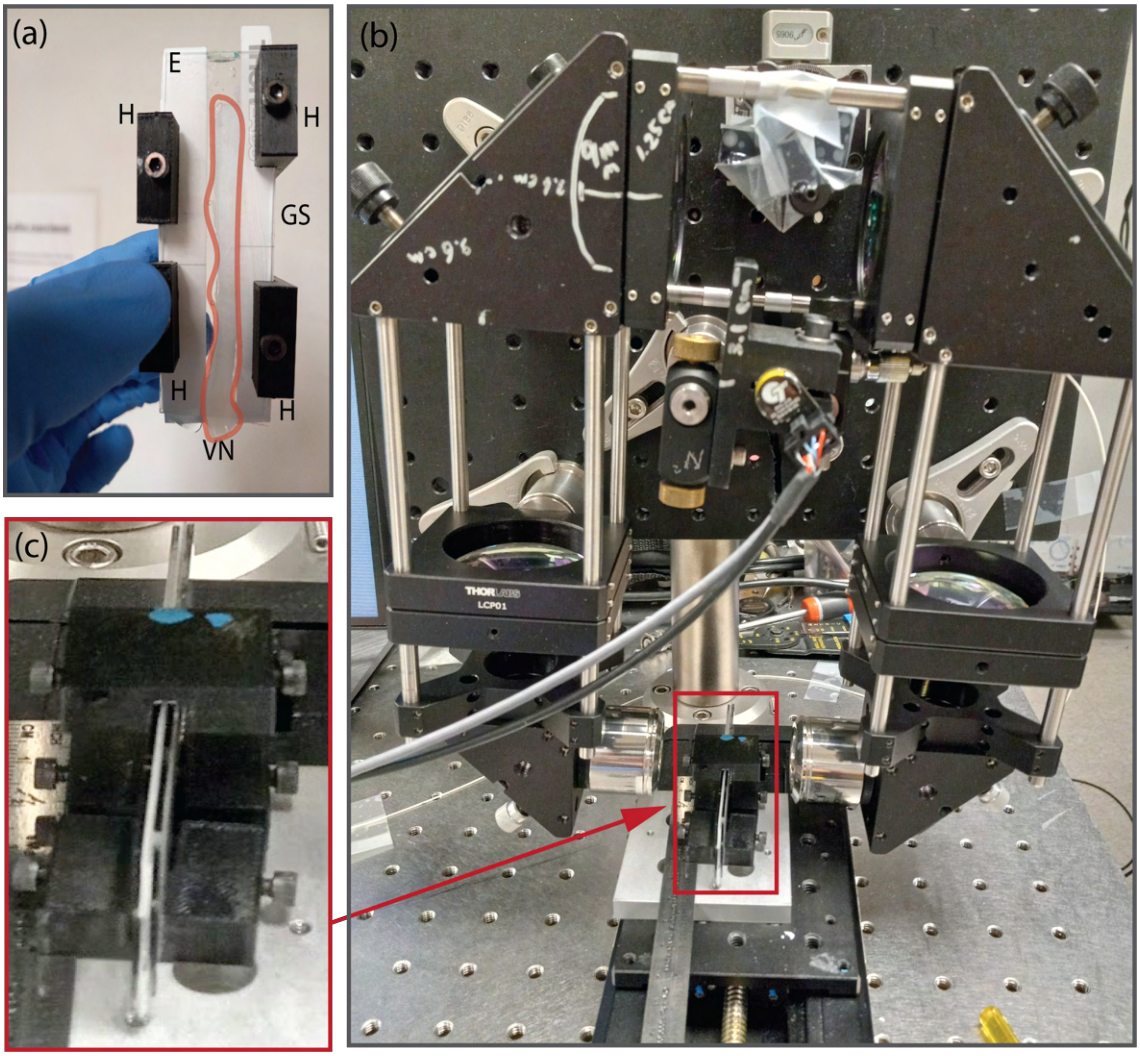

Figure 5.3: PS-OCT VN Imaging setup (microscope and sample details). (a) A sample prepared for imaging. The orange boundary highlights the sample edges: E: enclosure; H: custom Holder; GS: Glass slide; VN: Vagus Nerve. (b) Dual-surface scanning microscope. The sample was translated on the linear motorized stage. (c) Magnified image of the sample. The sample was compressed to $\sim$ 650 µm.

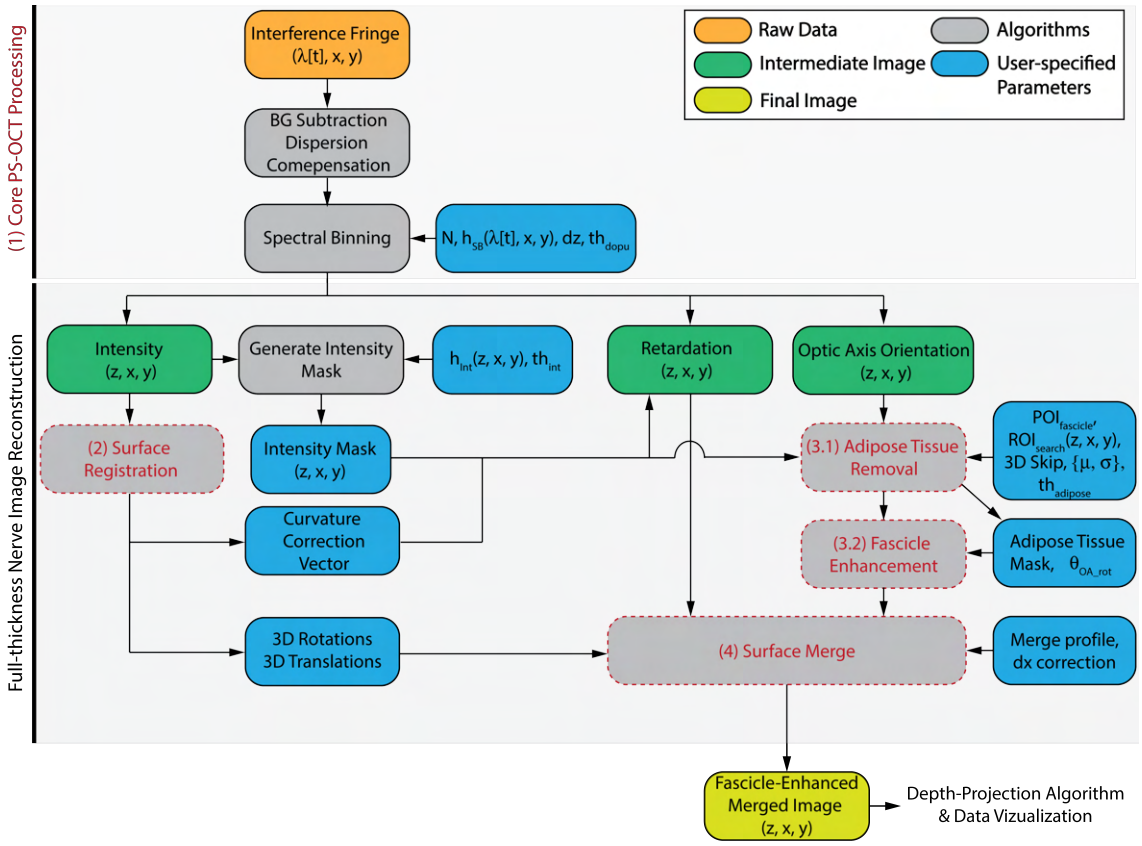

Figure 5.4: Processing pipeline workflow from spectral raw data to nerve image. The pipeline can be separated into the established OCT processing step and a tailored processing step for the fascicle-tracing application. Key algorithms are denoted by red-dotted box, and are discussed below.

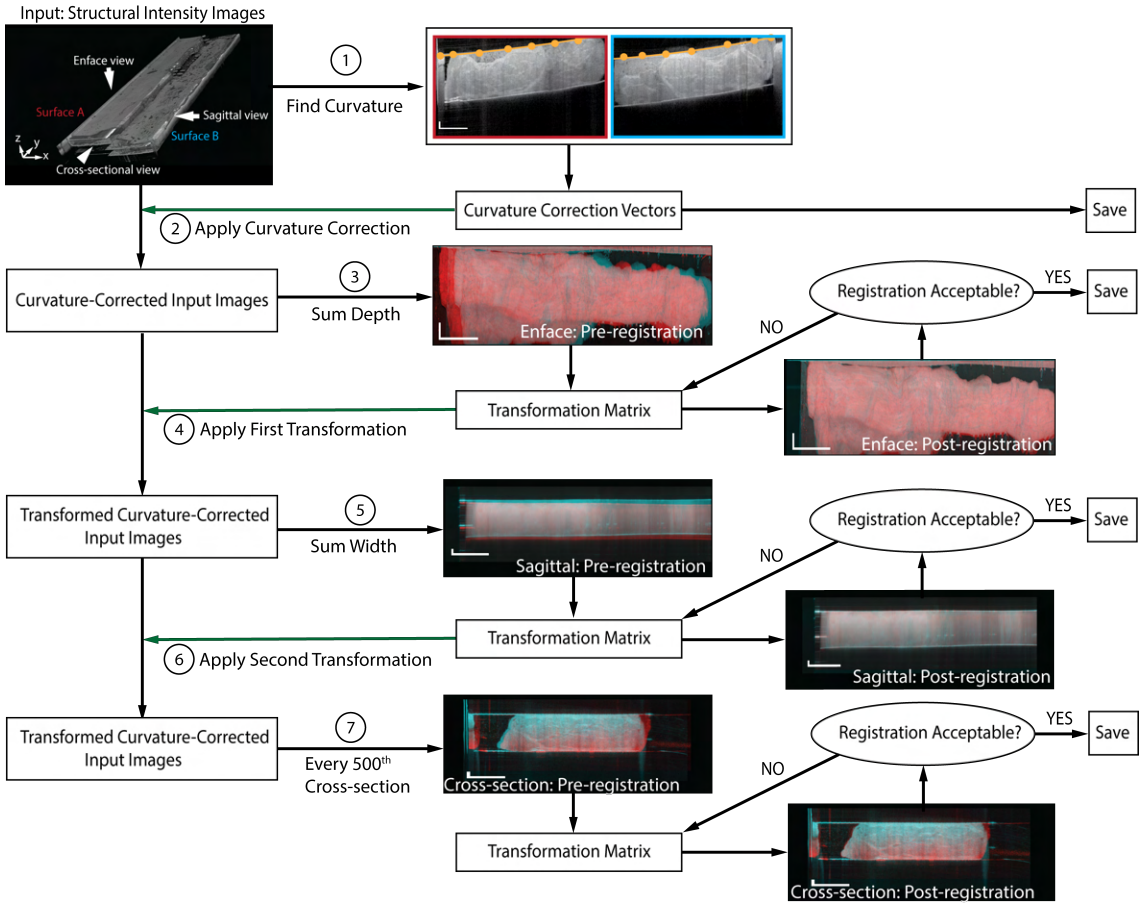

Figure 5.5: Nerve-specific processing pipeline. The algorithm followed seven key steps to determine the optimum geometrical transformations necessary to merge surfaces A and B together. The structural intensity images were used as the input to the algorithm from which a curvature correction vector was determined. The vector was applied to each respective surface and the resultant images underwent three sets of 3D transformation, which were sequentially applied to the original structural intensity images (green arrows). Pre-registration and post-registration images of the registration are shown for sample 2. The scale bars are: x-axis: 1 mm; y-axis: 1 cm; z-axis; 1 mm.

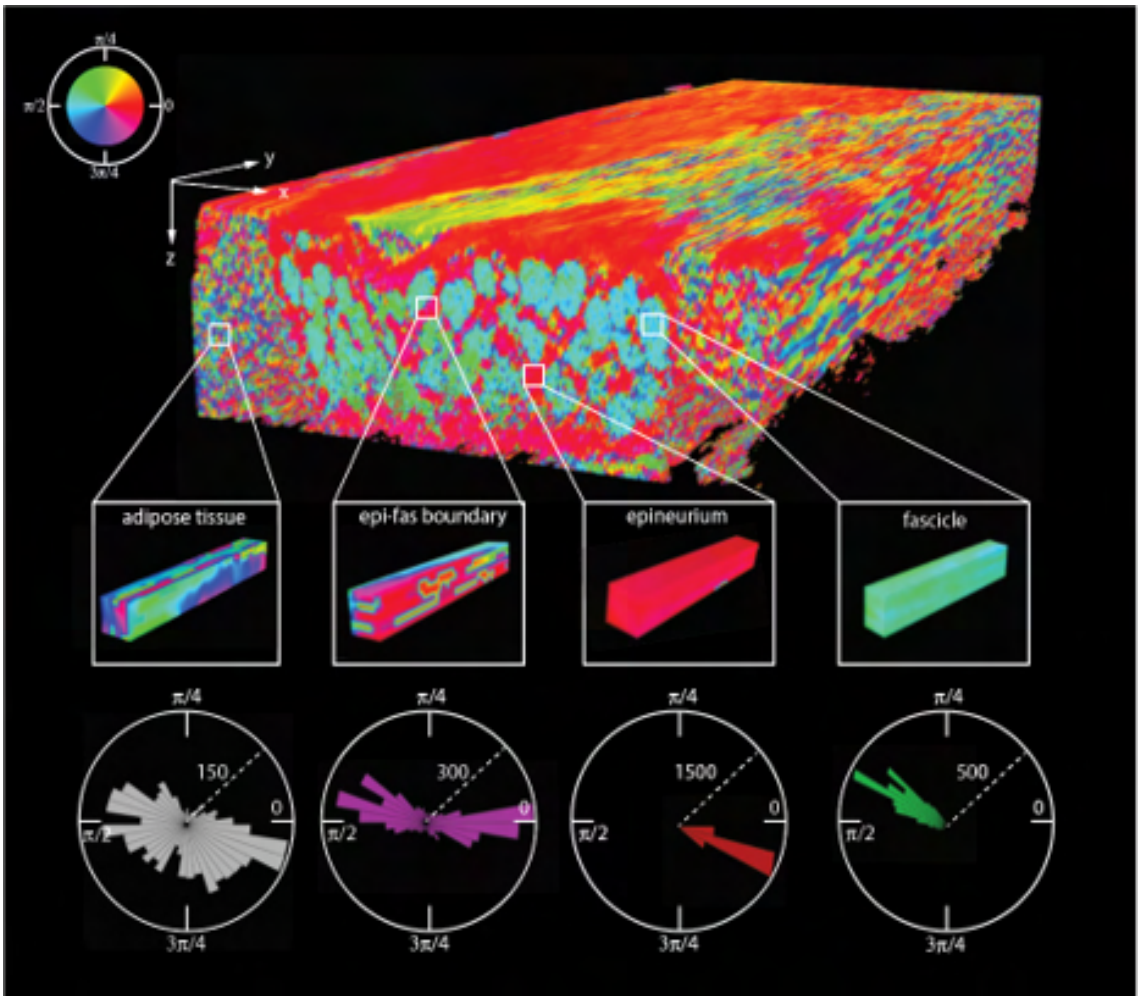

Figure 5.6: The fascicle segmentation algorithm takes advantage of the polarimetry features of the assumed three tissue types to discriminate fascicle voxels. Histogram of OA axis orientation (0 to π radians map to an HSV color wheel) distribution is shown for different tissue types. The radius of the polar histogram shows the maximum count. The fascicle and epineurium exhibit orthogonality, while adipose tissue follows a quasi-random distribution. A two-step segmentation algorithm was written to mask voxels with strong adipose tissue signals and to separate the fascicle from the epineurium.

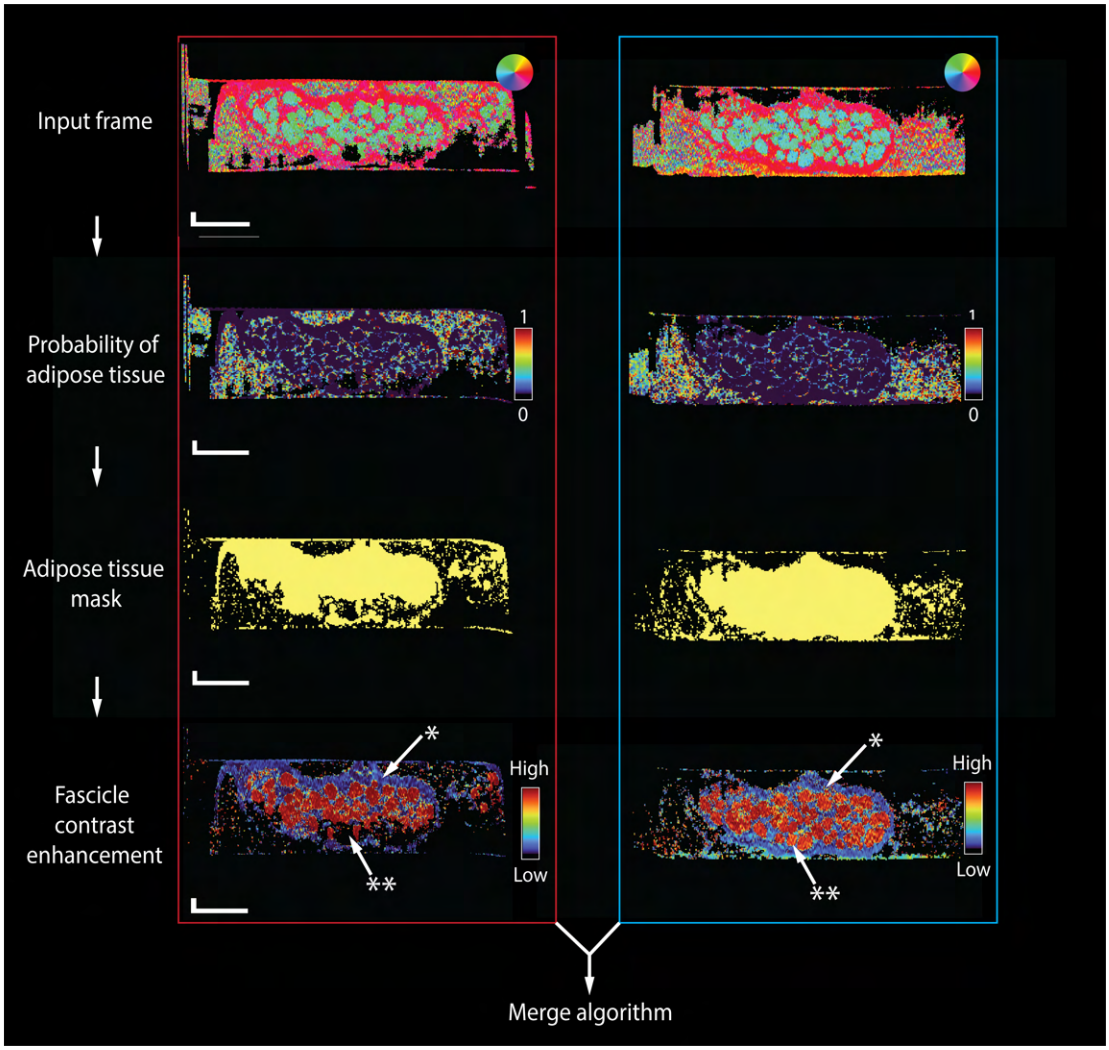

Figure 5.7: The adipose removal component of the fascicle segmentation algorithm takes the curvature-corrected OA images (row 1) and generates the probability of adipose tissue (row 2) and adipose tissue masks (row 3). The contrast enhancement component acts on the adipose-masked OA images to further enhance the contrast between the fascicles and epineurium (row 4). The cross-section image of contrast-enhanced images had missing or obscured information denoted by * and **. The vertical and horizontal scale bars are 100 µm and 1 mm, respectively.

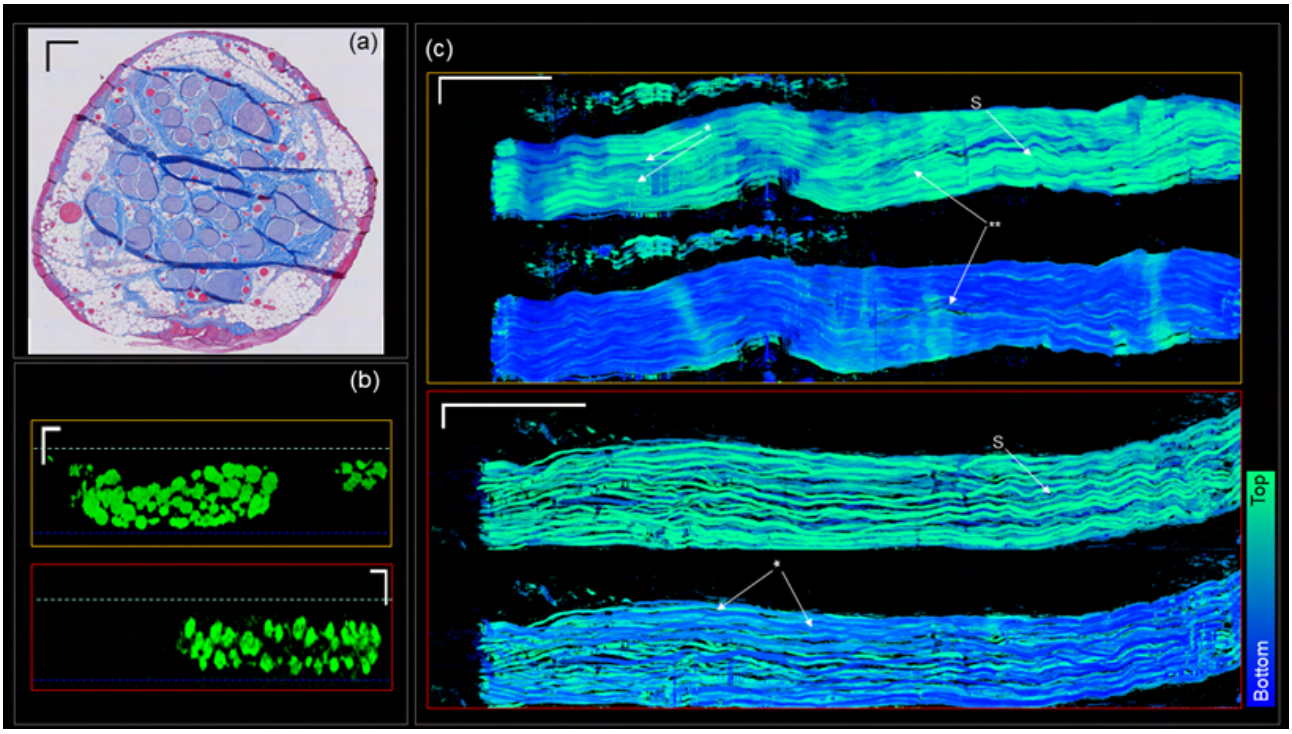

Figure 5.8: PS-OCT can resolve fascicles as small as 20 µm in diameter across the full depth of the VN sample and allows multi-centimeter length fascicle tracing. Sample A is denoted by a solid orange box, and sample B is denoted by a solid red box. (a) A representative histology slide of a cervical VNE showing gross fascicle morphology. Scale bar: 300 µm. (b) Fascicle-enhanced cross-sectional image of the two VN samples in orange and red boxes. Scale bar: 300 µm. The dotted lines show nominal top and bottom surfaces. (c) Depth-projected sample images. * and ** denote fascicles splitting/merging and fascicles traversing the full width of sample, respectively. S points to a segment of high contortion observed in both samples. Scale bar: 1 mm width by 1 cm length.

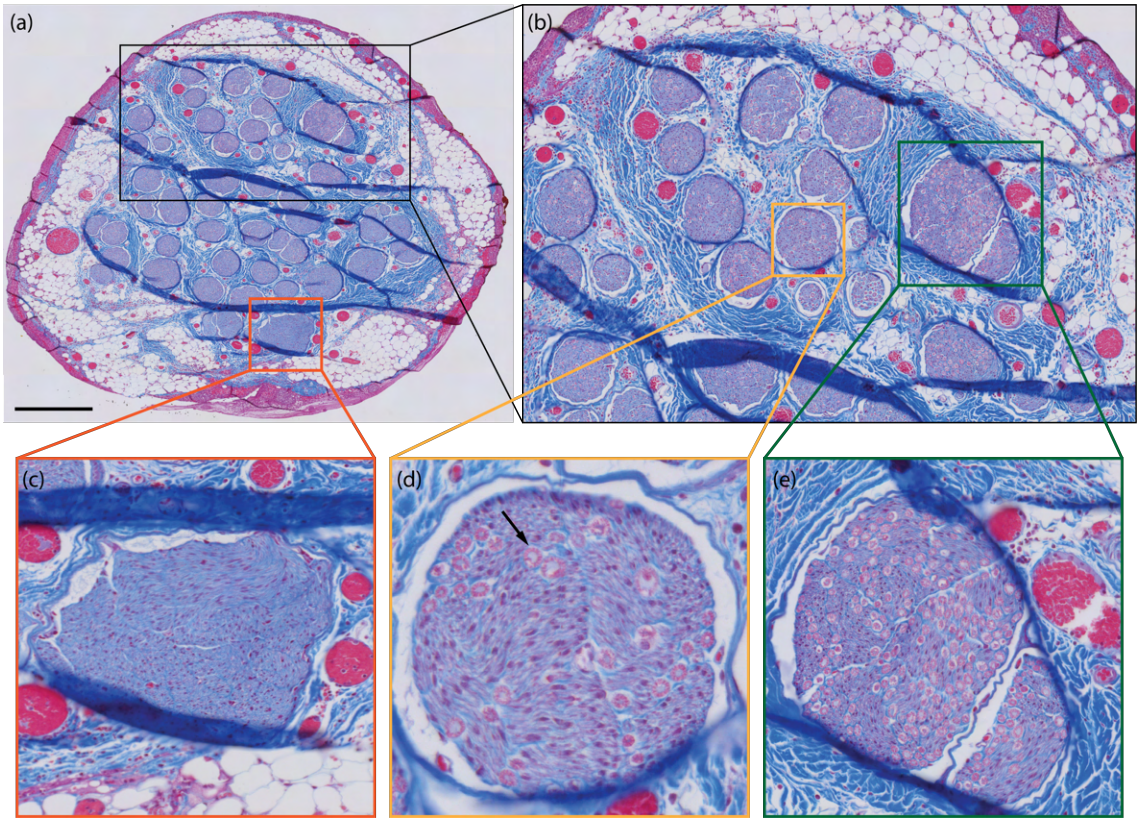

Figure 5.9: A representative histology slide showing myelination pattern typically seen in cervical porcine VN samples. (a) Full nerve view. (b) Detail of a group of fascicles exhibiting a relatively large number of myelinated neurons. Bottom row detail of individual fascicles show a range of myelination: (c) Predominantly small-diameter unmyelinated fibers, (d) Moderately numerous large-diameter myelinated fibers, and (e) Multiple large-diameter myelinated fibers. The black arrow in (d) identifies a large myelinated nerve exhibiting the characteristic oval, pink-white lipid sheath. Scale bar: 500 µm.

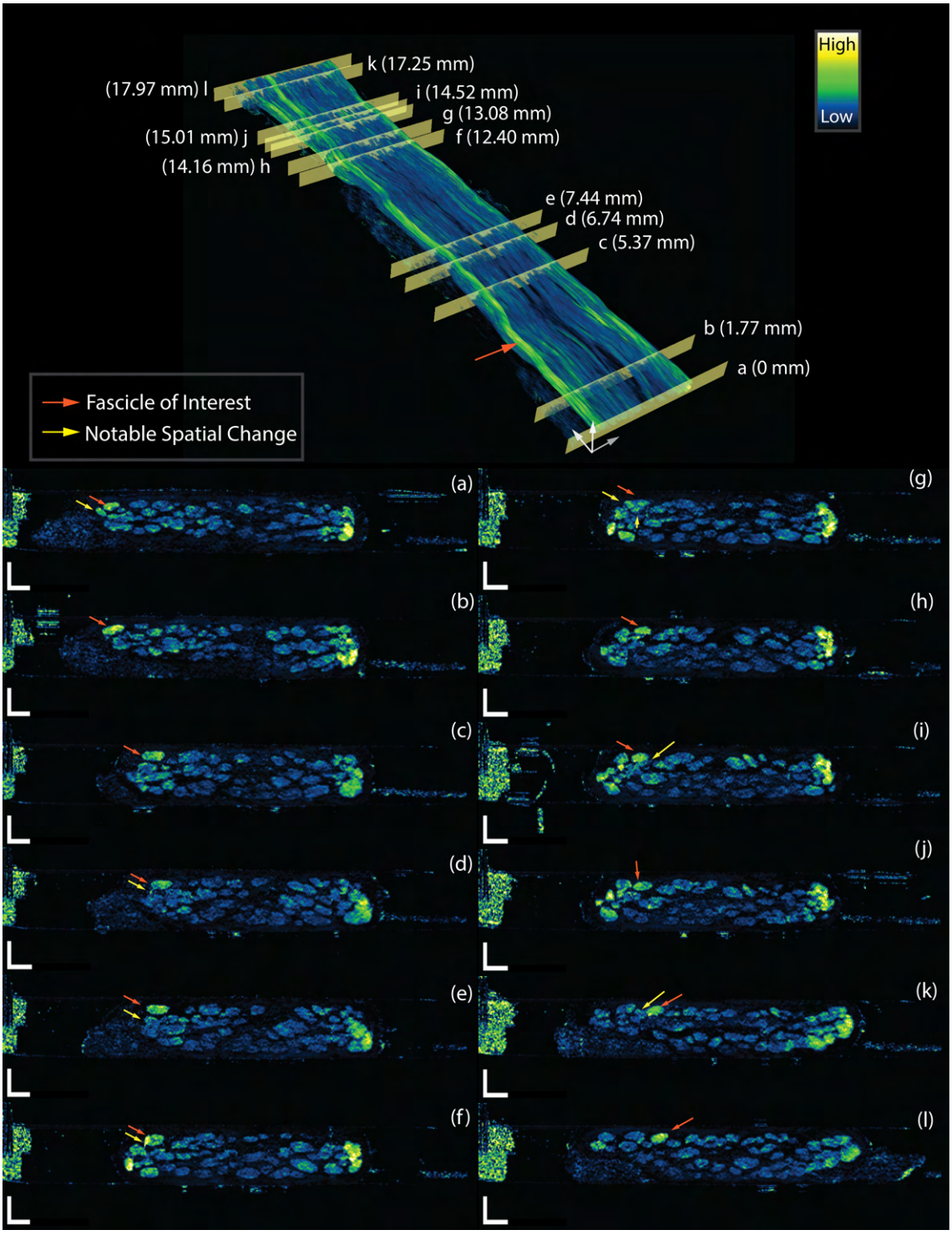

Figure 5.10: Cross-sectional images of directional retardance along a 1.8 cm segment of the fascicle. The fascicle of interest (orange arrow) has retardance than others. The yellow arrow identifies key events. Between (a) and (c), two fascicles merge. In (d), a small segment of the fascicle of interest splits and merges with another fascicle, increasing the retardance as seen in (e). A similar event occurs in (f), where a small fraction of a fascicle splits and merges with the fascicle of interest, elevating the local retardance. (g) shows the fascicle of interest splitting into three smaller fascicles. (i) and (j) show the fascicle of interest contacting a low retardance fascicle. Scale bar: 300 µm.

Chapter 6

Conclusion

Avoiding nerve damage exclusively by relying on anatomical landmarks has clear limitations. In North America, at least, there is an enormous incentive to bring robotic technology to the operating room in order to make surgery more precise. This is especially true for minimally invasive surgery (MIS) due to a significant cost advantage and improved patient experience. With a compound annual growth rate of 17%, the market for robotic MIS is expected to grow to $173.9 billion by 2029. Adoption of robotic platforms is expected to grow across the board, especially with 89% of orthopedic and 85% of neurosurgeons interested in using them. This presents an opportunity to integrate quantitative imaging tools for surgical guidance into the robots. The CPU of the robot can also help interpret the images with various advanced computational tools and machine learning algorithms. Most importantly, since there is no need for exogenous labeling, the time to translation is significantly reduced, and the linear surgical flow will not be interrupted if surgeons could receive real-time feedback.

A depth-resolved volumetric platform like OCT is best-suited, but the technical requirement to meet the hardware requirement (see Chapter 1) is non-trivial, and in fact impossible with existing approaches and the technology available in the market. Especially the need to be compatible with endoscopic cameras poses a massive data challenge and hardware challenge to performing scanner-less OCT imaging. To address these problems, CL-OCT was developed, which has a data rate perfectly compatible with cameras and gets rid of the hardware complexity. The remaining task is to show that the CL-OCT data are compatible with

machine learning models for feature extraction. Ultimately, the goal of CL-OCT is not to replace existing white light imaging but to enhance the surgeons' vision with high-contrast images. Thus, the images shown in this work are intermediate results. The end system would incorporate a high-power amplification strategy presented in Chapter 3 to capture the full surgical field without any scanning. This opens new research opportunities for assessing image quality and developing novel source and sensor platforms. Understanding this new imaging modality to the required depth would likely require a few more PhD dissertations, and I happily pass the baton to the next generation of graduate students.

Whether CL-OCT is the right solution remains to be seen. It is, however, encouraging that the solution vector is highly aligned with the current trend (or the spirit) of combining imaging platforms with computational tools to minimize hardware burden. Even if CL-OCT is shown to not be a complete solution, this body of work still teaches an important lesson: Always focus on the relevant boundary conditions when (1) posed with a highly specific problem and (2) existing approaches are ill-suited for the problem - a guided evolution of the existing technology may be required.

Appendix A

Quantum Mechanical Derivations of SNR

Quadrature Measurement Statistic for Coherent State Light

In quantum mechanics, the outcome of an experiment depends on the **type of measurement** performed on the system and the **state** that the system is (or could be) in. Interferometry is a quadrature measurement (phase-sensitive), so we forgo other types of measurements. Harmonic oscillator annihilation and creation operators can be recast to quadrature operators as

$$\hat{X} = \frac{1}{2}(\hat{a} + \hat{a}^{\dagger}) \tag{A.1}$$

$$\hat{Y} = \frac{i}{2}(\hat{a} - \hat{a}^{\dagger}) \tag{A.2}$$

For coherent state (valid assumption for swept-source) $|\alpha\rangle$, the mean of the quadrature operators are

$$\langle \hat{X} \rangle \equiv \langle \alpha | \hat{X} | \alpha \rangle = \frac{1}{2}(\alpha + \alpha^{*}) = |\alpha| cos\theta \tag{A.3}$$

and

$$\langle \hat{Y} \rangle \equiv \langle \alpha | \hat{Y} | \alpha \rangle = \frac{i}{2}(\alpha - \alpha^{*}) = |\alpha| sin\theta \tag{A.4}$$

where the complex amplitude of the coherent state light $\alpha = |\alpha|e^{i\theta}$. The variance is computed by first evaluating the square mean of the operator

$$\begin{aligned}
\langle \hat{X}^2 \rangle &= \frac{1}{4}\langle \hat{a}\hat{a} + \hat{a}^\dagger\hat{a}^\dagger + \hat{a}\hat{a}^\dagger + \hat{a}^\dagger\hat{a} \rangle \\
&= \frac{1}{4}\langle \hat{a}\hat{a} + \hat{a}^\dagger\hat{a}^\dagger + 1 + 2\hat{a}^\dagger\hat{a} \rangle \\
&= \frac{1}{4} + \frac{1}{4}(\alpha^2 + \alpha^{*2} + 2\alpha\alpha^*) \\
&= \frac{1}{4} + \Big(\frac{\alpha + \alpha^*}{2}\Big)^2 \\
&= \frac{1}{4} + (|\alpha| cos\theta)^2 \\
&= \frac{1}{4} + \langle \hat{X} \rangle^2
\end{aligned} \tag{A.5}$$

A similar process yields

$$\langle \hat{Y}^2 \rangle = \frac{1}{4} + \langle \hat{Y}^2 \rangle \tag{A.6}$$

The variance is simply

$$\langle \Delta X \rangle^2 \equiv \langle \hat{X}^2 \rangle - \langle \hat{X} \rangle^2 = \frac{1}{4} \tag{A.7}$$

The other quadrature operator yields the same result

$$\langle \Delta Y \rangle^2 = \frac{1}{4} \tag{A.8}$$

Thus, the coherent state is the minimum uncertainty state predicted by the Cauchy-Schwartz inequality.

$$(\Delta X)^2(\Delta Y)^2 = \frac{1}{16} \tag{A.9}$$

Balanced Detection for Quadrature Measurement

Assume the reference field is (1) much stronger than the signal field and (2) in a coherent state. Let the signal annihilation operator at the input of a beam splitter (BS) be $\hat{a}$, and the reference annihilation operator be $\hat{b}$. These operators are injected into different inputs

port of the BS. The BS input-output relations are

$$\hat{c} = \mathcal{R}\hat{a} + \mathcal{T}\hat{b} \tag{A.10}$$

$$\hat{d} = \mathcal{R}\hat{b} + \mathcal{T}\hat{a} \tag{A.11}$$

where $|\mathcal{R}|^2 + |\mathcal{T}|^2 = 1$ and $\phi_R - \phi_T = \frac{\pi}{2}$.

Single Port Detection

Consider photodetection of $\hat{c}$, $\langle \hat{N}_c \rangle = \langle \hat{c}^\dagger \hat{c} \rangle$. The mean is

$$\begin{aligned}
\langle \hat{N}_c \rangle &= \langle (\mathcal{R}^* \hat{a}^\dagger + \mathcal{T}^* \hat{b}^\dagger)(\mathcal{R}\hat{a} + \mathcal{T}\hat{b}) \rangle \\
&= \langle |\mathcal{R}|^2 \hat{a}^\dagger \hat{a} + |\mathcal{T}|^2 \hat{b}^\dagger \hat{b} + \mathcal{R}^* \mathcal{T} \hat{a}^\dagger \hat{b} + \mathcal{T}^* \mathcal{R} \hat{b}^\dagger \hat{a} \rangle \\
&= \langle |\mathcal{R}|^2 \hat{a}^\dagger \hat{a} + |\mathcal{T}|^2 |B|^2 + |\mathcal{R}||\mathcal{T}||B| \left[(\hat{a} e^{i\chi})^\dagger + (\hat{a} e^{i\chi}) \right] \rangle \\
&= |\mathcal{R}|^2 \langle \hat{N}_a \rangle + |\mathcal{T}|^2 |B|^2 + 2|\mathcal{R}||\mathcal{T}||B| \langle \hat{X}_a \rangle
\end{aligned} \tag{A.12}$$

where θ associated with the quadrature operator is now $\chi = \frac{\pi}{2} + \theta_s - \theta_r$, and $\hat{b} \to |B| e^{i\theta_r}$ given the assumption. The variance is

$$\langle \Delta N_c \rangle^2 = \langle (\hat{c}^\dagger)^2 (\hat{c})^2 \rangle + \langle \hat{c}^\dagger \hat{c} \rangle - \langle \hat{c}^\dagger \hat{c} \rangle^2 \tag{A.13}$$

The first term after neglecting small order terms with respect to $|B|^2$ (and after tedious algebra) is

$$\begin{aligned}
\langle (\hat{c}^\dagger)^2 (\hat{c})^2 \rangle \approx |\mathcal{T}|^4 |B|^4 + 4|\mathcal{T}|^3 |\mathcal{R}||B|^3 \langle \hat{X}_a \rangle + \\
|\mathcal{T}|^2 |\mathcal{R}|^2 |B|^2 \left[(\hat{a} e^{i\chi})^{\dagger 2} + (\hat{a} e^{i\chi})^2 + 4\hat{a}^\dagger \hat{a} \right] \rangle
\end{aligned} \tag{A.14}$$

The second term is simply the mean,

$$\langle \hat{c}^\dagger \hat{c} \rangle \approx |\mathcal{T}|^2 |B|^2 + 2|\mathcal{R}||\mathcal{T}||B| \langle \hat{X}_a \rangle \tag{A.15}$$

The last term is

$$\begin{aligned}\langle \hat{c}^\dagger \hat{c} \rangle^2 \approx |\mathcal{T}|^4 |B|^4 + 4|\mathcal{R}|^2 |\mathcal{T}|^2 |B|^2 \langle \hat{X}_a \rangle^2 + \\ 2|\mathcal{R}|^2 |\mathcal{T}|^2 |B|^2 \langle \hat{a}^\dagger \hat{a} \rangle + 4|\mathcal{R}||\mathcal{T}|^3 |B|^3 \langle \hat{X}_a \rangle\end{aligned} \tag{A.16}$$

From the definition of the quadrature operator

$$\langle \Delta N_c \rangle^2 = 4|\mathcal{T}|^2 |\mathcal{R}|^2 |B|^2 \langle \Delta X_a \rangle^2 + |\mathcal{T}|^2 (1 - |\mathcal{R}|^2) |B|^2 \tag{A.17}$$

The single port homodyne SNR is

$$\begin{aligned} SNR_1 &= \frac{4|\mathcal{R}|^2 |\mathcal{T}|^2 |B|^2 \langle \hat{X}_a \rangle^2}{4|\mathcal{T}|^2 |\mathcal{R}|^2 |B|^2 \langle \Delta X_a \rangle^2 + |\mathcal{T}|^4 |B|^2} \\ &= \frac{\langle \hat{X}_a \rangle^2}{\langle \Delta X_a \rangle^2 + \frac{1-|\mathcal{R}|^2}{4|\mathcal{R}|^2}} \\ &= \frac{|A|^2 cos\chi^2}{\frac{1}{4} + \frac{1-|\mathcal{R}|^2}{4|\mathcal{R}|^2}} \end{aligned} \tag{A.18}$$

where in the last equality, a coherent state was assumed for the signal. Physically, the second term in the noise arises from the corpuscular nature of light: Reference photon can be either transmitted or reflected at the BS and we do not know which way it went. Note that the noise is present despite the clean reference field assumed at the onset. A more inclusive SNR expression without with general reference variance is

$$SNR_1 = \frac{\langle \hat{X}_a \rangle^2}{\langle \Delta X_a \rangle^2 + \frac{1-|\mathcal{R}|^2}{|\mathcal{R}|^2} \langle \Delta X_b \rangle^2} \tag{A.19}$$

This general form can accommodate any deviation from the minimum uncertainty state. Let

$$\hat{b'} \equiv \hat{b} + \Delta \tag{A.20}$$

where the second term is a zero-mean complex amplitude noise, $\mathcal{N}(0, \sigma_\Delta^2)$.

$$\langle \hat{b'}^2 \rangle = \langle \hat{b}^2 \rangle + \Delta^2 \tag{A.21}$$

$$\langle(\hat{b'}^{\dagger})^2\rangle = \langle(\hat{b}^{\dagger})^2\rangle + (\Delta^*)^2 \tag{A.22}$$

$$\langle\hat{b'}^{\dagger}\hat{b'}\rangle = \langle\hat{b}^{\dagger}\hat{b}\rangle + |\Delta|^2 \tag{A.23}$$

Then.

$$\begin{aligned}\langle\hat{X}^2_{b'}\rangle &= \langle\hat{X}^2_b\rangle + \langle\Big(\frac{\Delta+\Delta^*}{2}\Big)^2\rangle \\ &= \langle\hat{X}^2_b\rangle + \langle Re(\Delta)^2\rangle\end{aligned} \tag{A.24}$$

where the zero-mean of the excess noise and the general expression for $\langle\hat{X}^2\rangle$ was used. Then,

$$\langle\Delta X_{b'}\rangle^2 = \langle\Delta X_b\rangle^2 + \sigma^2_{Re(\Delta)} \tag{A.25}$$

the second term is the real variance. We can operationally define a multiplicative noise such as the source RIN.

$$\sigma^2_{Re(\Delta)} = |\mathcal{T}|^2|B|^2 RIN \tag{A.26}$$

In which case,

$$SNR_1 = \frac{\langle\hat{X}_a\rangle^2}{\langle\Delta X_a\rangle^2 + \frac{1-|\mathcal{R}|^2}{|\mathcal{R}|^2}(\langle\Delta X_b\rangle^2 + |\mathcal{T}|^2|B|^2 RIN)} \tag{A.27}$$

Dual Port Balanced Detection

Define the balanced detector operator as

$$\hat{D} \equiv \hat{c}^{\dagger}\hat{c} - \hat{d}^{\dagger}\hat{d} \tag{A.28}$$

Let $\mathcal{T} = \mathcal{R} = \frac{1}{\sqrt{2}}$ with $\hat{b} \to |B|e^{i\theta_r}$. Then,

$$\langle\hat{D}\rangle = |B|\Big[(\hat{a}e^{i\chi})^{\dagger} + (\hat{a}e^{i\chi})\Big] = |B|\langle\hat{X}_a\rangle \tag{A.29}$$

The variance is easy to compute

$$\langle\Delta D\rangle^2 = \langle\hat{D}^2\rangle - \langle\hat{D}\rangle^2 = |B|^2\langle\Delta X_a\rangle^2 \tag{A.30}$$

Thus,

$$SNR_2 = \frac{\langle \hat{D} \rangle^2}{\langle \Delta D \rangle^2} = \frac{\langle \hat{X}_a \rangle^2}{\langle \Delta X_a \rangle^2} \tag{A.31}$$

Thus, the SNR of balanced detector is the signal SNR before the BS (neglecting the beat noise between the signal and the reference RIN predicted in ref). Reference shot noise and excess noise are perfectly balanced out. **This SNR is known as the standard quantum limit.** This simplifies the task at hand dramatically. We just need to know how much noise is added to the quadrature signal propagating through optical elements. The output noise variance is the sum of the input noise variance and the uncorrelated added noise variance.

Balanced Detection after Gain Medium

The input in-phase operator $\hat{X}_a$ after a gain element with gain G is

$$\hat{X}_G = \sqrt{G}\hat{X}_a + \sqrt{G-1}\hat{X}_v \tag{A.32}$$

where $\hat{X}_v$ is an auxiliary mode coupled to a thermal bath (incoherent light). The mean and variance of the output after a gain element is found as follows

$$\langle \hat{X}_G \rangle = \sqrt{G}\langle \hat{X}_a \rangle + \sqrt{G-1}\langle \hat{X}_v \rangle \tag{A.33}$$

$$\langle \hat{X}_G^2 \rangle = G\langle X_a^2 \rangle + (G-1)\langle X_v^2 \rangle + 2\sqrt{G(G-1)}\langle \hat{X}_a \rangle \langle \hat{X}_v \rangle \tag{A.34}$$

where the last term uses the fact that the signal mode and the auxiliary mode are uncorrelated.

$$\langle \hat{X}_G \rangle^2 = G\langle X_a \rangle^2 + (G-1)\langle X_v \rangle^2 + 2\sqrt{G(G-1)}\langle \hat{X}_a \rangle \langle \hat{X}_v \rangle \tag{A.35}$$

$$\langle \Delta \hat{X}_G \rangle^2 = G\langle \Delta \hat{X}_a \rangle^2 + (G-1)\langle \Delta \hat{X}_v \rangle^2 \tag{A.36}$$

From the assumption of thermal noise with the identification of the photon number as the spontaneous emission factor,

$$\langle \Delta \hat{X}_G \rangle^2 = G\langle \Delta \hat{X}_a \rangle^2 + \Big(\frac{G-1}{2}\Big)(n_{sp} - \frac{1}{2}) \tag{A.37}$$

The SNR is

$$SNR_G = \frac{G\langle \hat{X}_a \rangle^2}{G\langle \Delta \hat{X}_a \rangle^2 + \left(\frac{G-1}{2}\right)(n_{sp} - \frac{1}{2})} \tag{A.38}$$

For the coherent state signal, a high gain medium with $n_{sp} = 1$ yields the 3dB NF.

Balanced Detection after Loss Medium

The input in-phase operator $\hat{X}_a$ after a loss element with transmissivity L is

$$\hat{X}_L = \sqrt{L}\hat{X}_a + \sqrt{1-L}\hat{X}_v \tag{A.39}$$

where $\hat{X}_v$ is vacuum mode quadrature operator, necessarily injected to preserve the boson commutation relations. The mean and variance of the output after a loss medium are

$$\begin{aligned} \langle \hat{X}_L \rangle &= \sqrt{L}\langle \hat{X}_a \rangle + \sqrt{1-L}\langle \hat{X}_v \rangle \\ &= \sqrt{L}\langle \hat{X}_a \rangle \end{aligned} \tag{A.40}$$

where the last equality is obtained from $\langle \hat{c}^\dagger \hat{c} \rangle = 0$. With

$$\begin{aligned} \langle \hat{X}_L^2 \rangle &= L\langle \hat{X}_a^2 \rangle + (1-L)\langle \hat{X}_v^2 \rangle + \sqrt{L(1-L)}(\langle \hat{X}_a \hat{X}_v \rangle + (\langle \hat{X}_v \hat{X}_a \rangle) \\ &= L\langle \hat{X}_a^2 \rangle + (1-L)\langle \hat{X}_v^2 \rangle \end{aligned} \tag{A.41}$$

the variance is

$$\langle \Delta X_L \rangle^2 = \langle \hat{X}_L^2 \rangle - \langle \hat{X}_L \rangle^2 \quad = L\langle \Delta X_a \rangle^2 + (1-L)\langle \Delta X_v \rangle^2 \tag{A.42}$$

The balanced detection SNR after a loss medium is

$$SNR_L = \frac{L\langle \hat{X}_a \rangle^2}{L\langle \Delta X_a \rangle^2 + (1-L)\frac{1}{4}} \tag{A.43}$$

This shows that both the signal power and the noise power are reduced by the loss, but an auxilary vacuum mode adds noise to preserve the quadrature quantum noise, $\frac{1}{4}$. The

quantum detection efficiency, η, of a detector can be modeled the same way

$$SNR_{\eta} = \frac{\eta\langle\hat{X}_a\rangle^2}{\eta\langle\Delta X_a\rangle^2 + (1-\eta)\frac{1}{4}} \tag{A.44}$$

This SNR including the detector quantum efficiency is known as the quantum limit as opposed to the standard quantum limit shown earlier.

Balanced Detection after Gain Medium followed by Loss Medium

The vacuum noise and amplifier noise will be uncorrelated so each noise contribution add.

$$\begin{aligned} SNR_{G\to L} &= \frac{LG\langle\hat{X}_a\rangle^2}{LG\langle\Delta X_a\rangle^2 + L\left(\frac{G-1}{2}\right)(n_{sp}-\frac{1}{2}) + (1-L)\frac{1}{4}} \\ &= \frac{\langle\hat{X}_a\rangle^2}{\langle\Delta X_a\rangle^2 + \left(\frac{G-1}{2G}\right)(n_{sp}-\frac{1}{2}) + \left(\frac{1-L}{LG}\right)\frac{1}{4}} \end{aligned} \tag{A.45}$$

where the last expression shows more clearly the relative noise contribution from the loss and gain media. Clearly, for $n_{sp} = 1$, the amplifier noise dominates over the excess loss if

$$G \gg \frac{1-L}{L} \tag{A.46}$$

Balanced Detection after Loss Medium followed by Gain Medium

If the loss comes before the gain,

$$\begin{aligned} SNR_{L\to G} &= \frac{GL\langle\hat{X}_a\rangle^2}{GL\langle\Delta X_a\rangle^2 + G(1-L)\frac{1}{4} + \left(\frac{G-1}{2}\right)(n_{sp}-\frac{1}{2})} \\ &= \frac{\langle\hat{X}_a\rangle^2}{\langle\Delta X_a\rangle^2 + \left(\frac{1-L}{L}\right)\frac{1}{4} + \left(\frac{G-1}{2GL}\right)(n_{sp}-\frac{1}{2})} \end{aligned} \tag{A.47}$$

For high G medium with $n_{sp} = 1$, the additive noise term becomes

$$\frac{2-L}{L} \tag{A.48}$$

therefore, amplifier further degrades SNR_L by the amplifier NF. Thus, the amplifier cannot suppress the quantum noise present at its input.

Balanced IQ Detection

This scenario uses two balanced detectors with the reference field being 90 degrees out of phase. The simultaneous detection of in-phase and the quadrature components takes a 3dB noise penalty relative to the single quadrature detection but the coherent addition of the quadratures recover the SNR. The physical locus of the added noise can be traced to the non-mixing 3dB coupler. Assuming 50/50 mixing coupler, the balanced mean I and Q signals are

$$\langle \hat{I} \rangle = \sqrt{L}\langle \hat{X}_a \rangle = \frac{|A|}{\sqrt{2}} cos\chi \tag{A.49}$$

$$\langle \hat{Q} \rangle = \frac{|A|}{\sqrt{2}} sin\chi \tag{A.50}$$

The quadrature variance are

$$\langle \Delta I \rangle^2 = \langle \Delta Q \rangle^2 = \frac{1}{2}\langle \Delta X_a \rangle^2 + \frac{1}{2}\langle \Delta X_v \rangle^2 = \frac{1}{4} \tag{A.51}$$

recovering the shot noise. We do not know which photon reached the I or the Q detector after passing through the 3dB non-mixing coupler. The simultaneous IQ measurement SNR is

$$SNR_{IQ} = \frac{|\langle \hat{I} \rangle + i\langle \hat{Q} \rangle|^2}{(\langle \Delta I \rangle^2 + \langle \Delta Q \rangle^2)} = ||A|e^{i\chi}|^2 \tag{A.52}$$

Suppose one discards the Q measurement and processes the I measurement only. Then,

$$SNR_I = \frac{\langle \hat{I} \rangle^2}{\langle \Delta I \rangle^2} = 2|A|^2|\frac{e^{i\chi} + e^{-i\chi}}{2}|^2 \tag{A.53}$$

while the noise is halved relative to full IQ measurement, the signal peak power in FD is reduced by a factor of 4. Hence,

$$SNR_{IQ} = SNR_I + 3dB \tag{A.54}$$

Obviously, if only I data is desired, then one would take out the non-mixing coupler and measure the in-phase quadrature with a single detector. In this case, the 3dB coupler NF is removed

$$SNR_I|_{SD} = \frac{||A|cos\chi|^2}{\langle \Delta X_a \rangle^2} = 4|A|^2|\frac{e^{i\chi} + e^{-i\chi}}{2}|^2 \tag{A.55}$$

Thus,

$$SNR_{IQ} = SNR_I|_{SD} \tag{A.56}$$

Note that for time-multiplexed IQ detection, there is no additive vacuum noise contribution from the non-mixing coupler. Assuming the same measurement time for each I and Q as the case analyzed above,

$$SNR_{IQ}^{time} = SNR_{IQ} + 3dB \tag{A.57}$$

Classically, the 3dB is the effective signal power doubling. Quantum mechanically, the signal power and the noise power are both doubled, so the 3 dB benefit is attributed to the absence of additive noise from the non-mixing coupler. There is no inherent benefit between the two IQ methods if the same integrated power is maintained.

Balanced IQ Detection after Gain Medium

Suppose a gain medium is placed before the simultaneous IQ detection circuit. The noise power in the I channel is then

$$\begin{aligned} \langle \Delta I_G \rangle^2 &= \frac{G}{2}\langle \Delta X_a \rangle^2 + \Big(\frac{G-1}{4}\Big)(n_{sp} - \frac{1}{2}) + \frac{1}{2}\langle \Delta X_v \rangle^2 \\ &\approx \frac{G}{2}\langle \Delta X_a \rangle^2 + \frac{G}{4}(n_{sp} - \frac{1}{2}) \\ &= \frac{G}{4} \\ &= \langle \Delta Q_G \rangle^2 \end{aligned} \tag{A.58}$$

where in the penultimate equality high gain amplifier is imposed and in the final equality $n_{sp} = 1$. The quadrature means are

$$\langle \Delta \hat{I}_G \rangle = \sqrt{\frac{G}{2}}|A|cos\chi \tag{A.59}$$

$$\langle \Delta \hat{Q}_G \rangle = \sqrt{\frac{G}{2}} |A| sin\chi \tag{A.60}$$

The simultaneous IQ measurement in this case is

$$\begin{aligned} SNR_{IQ|G} &= \frac{|\langle \hat{I}_G \rangle + i\langle \hat{Q}_G \rangle|^2}{(\langle \Delta I_G \rangle^2 + \langle \Delta Q_G \rangle^2)} = ||A|e^{i\chi}|^2 \\ &= SNR_{IQ} \end{aligned} \tag{A.61}$$

Hence, a high G ideal amplifier can overwhelm the additive noise introduced by the non-mixing coupler. For time-multiplexed IQ detection, each I and Q measurement will take the 3 dB NF penalty such that

$$SNR_{IQ}^{time} = SNR_{IQ|G}^{time} + 3dB \tag{A.62}$$

When adjusted for the power $SNR_{IQ}^{time} = SNR_{IQ}$. So it follows that time multiplexing with amplifier is 3dB worse than spatial multiplexing with amplifier. In short, for simultaneous measurement of conjugate variables, there is no NF penalty for placing an ideal amplifier. For independent measurements, each measurement will take the NF penalty.

Appendix B

Derivation of CLOCT Signal

The analytical solution for the CLOCT signal is fully derived assuming Gaussian form for $S(k)$. The signal is given by

$$I_{BD}(z) = \frac{\eta q}{h\nu}\sqrt{r(z)\sigma(1-\sigma)}\int_{-\infty}^{\infty} S(k)[e^{-i2kz} + e^{-i2kz}]dk \tag{B.1}$$

The frequency comb can be described as

$$S(k) = G(k)\big[L(k) * \sum_{n=-M}^{M} \delta(k - nk_0)\big] \tag{B.2}$$

where the total number of combs is given by $N = 2M + 1$. If linewidth function is assumed to be Gaussian,

$$L(k) = \frac{1}{\sqrt{2\pi\sigma_l^2}} exp\bigg[- \frac{(k-k_c)^2}{2\sigma_l^2}\bigg] \tag{B.3}$$

where k_c is the center frequency and σ_l is the FWHM linewidth. If the envelope is also assumed to be Gaussian,

$$G(k) = \frac{1}{\sqrt{2\pi\sigma_s^2}} exp\bigg[- \frac{(k-k_c)^2}{2\sigma_s^2}\bigg] \tag{B.4}$$

Substituting for $G(k)$ and $L(k)$, and using the sifting property of the convolution and switch-

ing the order of integration yields

$$I_{BD}(z) = \frac{\eta q}{2\pi h\nu}\sqrt{\frac{r(z)\sigma(1-\sigma)}{\sigma_l^2\sigma_s^2}}\sum_{n=-M}^{M}\int_{-\infty}^{\infty} exp\Big[-\frac{(k-nk_0-k_c)^2}{2\sigma_l^2}\Big]exp\Big[-\frac{(k-k_c)^2}{2\sigma_s^2}\Big][e^{i2kz}+e^{-i2kz}]dk \tag{B.5}$$

First, let us integrate the first term of the integrand

$$\mathcal{I}_1 = \int_{-\infty}^{\infty} exp\Big[-\frac{(k-nk_0-k_c)^2}{2\sigma_l^2} - \frac{(k-k_c)^2}{2\sigma_s^2} + i2kz\Big]dk \tag{B.6}$$

The argument of the exponent simplifies to

$$\mathcal{I}_1 = e^C\int_{-\infty}^{\infty} e^{-(Ak^2+Bk)}dk \tag{B.7}$$

where

$$C = \frac{k_0^2n^2\sigma_s^2 + 2k_ck_0n\sigma_s^2 + k_c^2(\sigma_s^2-\sigma_l^2)}{2\sigma_s^2\sigma_l^2} \tag{B.8}$$

$$A = \frac{\sigma_s^2+\sigma_l^2}{2\sigma_s^2\sigma_l^2} \tag{B.9}$$

and

$$B = -\frac{k_0n\sigma_s^2 + k_c(\sigma_s^2+\sigma_l^2) + i2z\sigma_s^2\sigma_l^2}{\sigma_s^2\sigma_l^2} \tag{B.10}$$

The solution has the form

$$\mathcal{I}_1 = \sqrt{\frac{\pi}{A}}e^{\frac{B^2}{4A}}e^C \tag{B.11}$$

After simplification,

$$\mathcal{I}_1 = \sqrt{\frac{2\pi\sigma_s^2\sigma_l^2}{\sigma_s^2+\sigma_l^2}}exp\Big[\frac{(k_0n\sigma_s^2+k_c(\sigma_s^2+\sigma_l^2))^2}{2(\sigma_s^2+\sigma_l^2)\sigma_s^2\sigma_l^2} - \frac{2z^2\sigma_s^2\sigma_l^2}{(\sigma_s^2+\sigma_l^2)}\Big]exp\Big[\frac{i2z(k_0n\sigma_s^2+k_c(\sigma_s^2+\sigma_l^2))}{(\sigma_s^2+\sigma_l^2)}\Big]e^C \tag{B.12}$$

Since the linewidth is much smaller than the spectral bandwidth, $\sigma_s >> \sigma_l$ holds, which further simplifies the equation to

$$\mathcal{I}_1 = \sigma_l\sqrt{2\pi}exp\big[-2z^2\sigma_l^2\big]\sum_{n=-M}^{M} exp\Big[\frac{(k_0n+k_c)^2}{\sigma_l^2}\Big]exp\Big[i2z(k_0n+k_c)\Big] \tag{B.13}$$

Similarly, $\mathcal{I}_2$ can be computed and the resultant equation is

$$I_{BD}(z) = 2\frac{\eta q}{h\nu\sigma_s}\sqrt{\frac{r(z)\sigma(1-\sigma)}{2\pi}}e^{-2z^2\sigma_l^2}\sum_{n=-M}^{M} exp\left[\frac{k_0 n + k_c}{\sigma_l}\right]^2 cos[2z(k_0 n + k_c)] \qquad \text{(B.14)}$$

This equation captures the relevant physics invovled in CLOCT measurement.

Appendix C

Fascicle Segmentation Algorithm And Data Visualization

The VN image is assumed to comprise three basic tissue types: adipose tissue, fascicle, and epineurium. In principle, the fascicle and epineurium have orthogonal OA orientations and are separable with simple thresholding. However, adipose tissue is a potent polarization scrambler that can have any possible OA orientation. In particular, the porcine VN contains much more adipose tissue than a human VN, exacerbating the problem. Moreover, given the imaging resolution, a voxel can contain any possible mixture of the three tissue types, so simple rigid thresholding is challenging. A robust two-step algorithm for fascicle segmentation is presented here. The first step aims to sense and mask adipose-laden voxels, maximally preserving epineurium and fascicle voxels. The second step maximizes the fascicle signal and minimizes the epineurium signal. At this point, a simple threshold can be applied to mask epineurium voxels preferentially.

C.1 Adipose Removal Algorithm

The goal here is to eliminate as many voxels containing adipose tissue as possible and preserve those containing fascicle, epineurium, or a mixture of fascicle and epineurium. Since the orthogonality between the fascicle and epineurium is known, finding the probability of a voxel containing either or both structures first and then subtracting unity from it is simpler.

From a select frame, the user identifies the center of a fascicle. Then, the mean OA angle is estimated from the polar histogram of all pixels contained in the 3D search window centered at the fascicle ROI:

$$< \theta_{fascicle} >_v = \frac{\sum_i^N C_i[V_i/255 \times 2\pi]}{\sum_i^N C_i} \tag{C.1}$$

where v is the center voxel of the search window, N is the number of bins, V_i is the bin edge value between 0 and 255 for the i^{th} bin, and C_i is the i^{th} bin count. Note that the OA is scaled to occupy the full 2π radians instead of π radians for reasons to be explained.

Having determined $< \theta_{fasicle} >$, the algorithm then rotates all voxels by θ_{rot} such that $< \theta_{fasicle} > = \pi/4$ radians. Then, $< \theta_{epineurium} >= 3\pi/4$ radians due to orthogonality and factor of 2 scaling. Also,$<_{adipose}>= 0$ given the random OA distribution. Now, the dot product of the x- and y- components of non-zero vectors in the first and the third quadrants yields a positive value, whereas that in the second and fourth quadrants yields a negative value. Therefore, voxels containing the structures we seek to preserve will have a large net positive value after the dot product, whereas those containing adipose tissue will have a very small value. To bolster robustness, the algorithm also scales the dot product by the angular variance:

$$v_{estimate} = \frac{\mathbf{x} \cdot \mathbf{y}}{Var_{circular}} \tag{C.2}$$

$$v_{estimate} = \frac{\sum_i^N C_i^2 cos([V_i/255 \times 2\pi] - \theta_{rot}) sin([V_i/255 \times 2\pi] - \theta_{rot})}{1 - \frac{\sqrt{[\sum_i^N C_i^2 cos([V_i/255 \times 2\pi)] - <\theta_i>]^2 + [\sum_i^N C_i^2 sin([V_i/255 \times 2\pi)] - <\theta_i>]^2}}{\sum_i^N C_i}}$$

(C.3)

where v is the center voxel θ_i is the mean OA angle of the voxel being interrogated. The range of $v_estimate$ extends from $-\infty$ to ∞. It is converted to a number between 1 and 0

via a logistic function with mean and scaling set by the user:

$$P(v_{adipose}) = 1 - \frac{1}{exp(-(v_{estimate} - \mu)/2)} \tag{C.4}$$

This is computed for all voxels that meet the user-defined intensity threshold, and the adipose tissue mask is generated for each surface.

C.2 Fascicle Contrast Enhancement Algorithm

Once the adipose tissue is masked, the fascicle can be separated from the epineurium. To maximize the contrast, a nonlinear transformation is applied to all voxels.

$$v_{fas-enhanced} = 255 \times \frac{cos(\frac{v}{255} \times 2\pi - < \theta_{fascicle} >) + 1}{2} \tag{C.5}$$

The multiplicative factor of 255 assumes 8-bit depth. The resulting image can then be thresholded.

C.3 Image Visualization

Depth-projection of merged fascicle images

Depth-projection images were generated to visualize the volumetric fascicle anatomy in Fig. 5.8 (c). A color map was chosen to encode the depth information. Appropriate alpha factor and exponential decay constant values were chosen to avoid saturating the final image. Two depth projections were generated for each VN sample, one with the maximum decay in the first depth layer and the other with the maximum decay in the last depth layer. Note that adipose tissue removal is critical for this visualization method to be meaningful.

Directional retardance

Standalone scalar retardance images from the PS processing pipeline do not contain information about the OA orientation. To encode the directionality of the sample, the scalar

retardance was weighted by the angular deviation of the OA with respect to the reference fascicle orientation.

$$\rho_{dir} = \rho_{scalar} cos(\Delta\theta) \tag{C.6}$$

where $\rho_s calar$ is the scalar retardance and $\Delta\theta$ is the OA orientation deviation from the contrast-enhanced reference fascicle OA orientation. Signal from the epineurium and parts of adipose tissue that are orthogonal to the reference fascicle orientation have significantly reduced retardance.

References

[1] G. Antoniadis, T. Kretschmer, M. T. Pedro, R. W. König, C. P. Heinen, and H.-P. Richter, "Iatrogenic nerve injuries: Prevalence, diagnosis and treatment," *Deutsches Ärzteblatt International*, vol. 111, no. 16, p. 273, 2014.

[2] T. Hara, M. Tatebe, T. Kurahashi, and H. Hirata, "Iatrogenic peripheral nerve injuries–common causes and treatment: A retrospective single-center cohort study," *Journal of Orthopaedic Science*, vol. 26, no. 6, pp. 1119–1123, 2021.

[3] C. Godballe, A. R. Madsen, C. H. Sørensen, S. Schytte, W. Trolle, J. Helweg-Larsen, L. Barfoed, L. Kristiansen, V. Z. Sørensen, G. Samuelsen, *et al.*, "Risk factors for recurrent nerve palsy after thyroid surgery: A national study of patients treated at danish departments of ent head and neck surgery," *European archives of oto-rhino-laryngology*, vol. 271, pp. 2267–2276, 2014.

[4] N. Pulos, E. H. Shin, R. J. Spinner, and A. Y. Shin, "Management of iatrogenic nerve injuries," *JAAOS-Journal of the American Academy of Orthopaedic Surgeons*, vol. 27, no. 18, e838–e848, 2019.

[5] M. H. Hohman, P. K. Bhama, and T. A. Hadlock, "Epidemiology of iatrogenic facial nerve injury: A decade of experience," *The Laryngoscope*, vol. 124, no. 1, pp. 260–265, 2014.

[6] L. Rasulić, A. Savić, F. Vitošević, M. Samardžić, B. Živković, M. Mićović, V. Baščarević, V. Puzović, B. Joksimović, N. Novakovic, *et al.*, "Iatrogenic peripheral nerve injuries—surgical treatment and outcome: 10 years' experience," *World Neurosurgery*, vol. 103, pp. 841–851, 2017.

[7] T. Renton and Z. Yilmaz, "Managing iatrogenic trigeminal nerve injury: A case series and review of the literature," *International journal of oral and maxillofacial surgery*, vol. 41, no. 5, pp. 629–637, 2012.

[8] H. H. Tavukçu, O. Aytac, and F. Atug, "Nerve-sparing techniques and results in robot-assisted radical prostatectomy," *Investigative and clinical urology*, vol. 57, no. Suppl 2, S172–S184, 2016.

[9] A. Kumar, V. R. Patel, S. Panaiyadiyan, K. R. S. Bhat, M. C. Moschovas, and B. Nayak, "Nerve-sparing robot-assisted radical prostatectomy: Current perspectives," *Asian Journal of Urology*, vol. 8, no. 1, pp. 2–13, 2021.

[10] A. Tewari, J. O. Peabody, M. Fischer, R. Sarle, G. Vallancien, V. Delmas, M. Hassan, A. Bansal, A. K. Hemal, B. Guillonneau, *et al.*, "An operative and anatomic study to help in nerve sparing during laparoscopic and robotic radical prostatectomy," *European urology*, vol. 43, no. 5, pp. 444–454, 2003.

[11] D. Huang, E. A. Swanson, C. P. Lin, J. S. Schuman, W. G. Stinson, W. Chang, M. R. Hee, T. Flotte, K. Gregory, C. A. Puliafito, *et al.*, "Optical coherence tomography," *science*, vol. 254, no. 5035, pp. 1178–1181, 1991.

[12] M. Wojtkowski, V. Srinivasan, J. G. Fujimoto, T. Ko, J. S. Schuman, A. Kowalczyk, and J. S. Duker, "Three-dimensional retinal imaging with high-speed ultrahigh-resolution optical coherence tomography," *Ophthalmology*, vol. 112, no. 10, pp. 1734–1746, 2005.

[13] M. B. Muijzer, P. A. Schellekens, H. J. Beckers, J. H. de Boer, S. M. Imhof, and R. P. Wisse, "Clinical applications for intraoperative optical coherence tomography: A systematic review," *Eye*, vol. 36, no. 2, pp. 379–391, 2022.

[14] A. S. John, I. Caturegli, N. S. Kubicki, and S. M. Kavic, "The rise of minimally invasive surgery: 16 year analysis of the progressive replacement of open surgery with laparoscopy," *JSLS: Journal of the Society of Laparoscopic & Robotic Surgeons*, vol. 24, no. 4, 2020.

[15] D. Borycki, M. Hamkało, M. Nowakowski, M. Szkulmowski, and M. Wojtkowski, "Spatiotemporal optical coherence (stoc) manipulation suppresses coherent cross-talk in full-field swept-source optical coherence tomography," *Biomedical optics express*, vol. 10, no. 4, pp. 2032–2054, 2019.

[16] I. Newton, *Opticks, or, a treatise of the reflections, refractions, inflections & colours of light*. Courier Corporation, 1952.

[17] A. A. Michelson and E. W. Morley, "On the relative motion of the earth and the luminiferous ether," *American journal of science*, vol. 3, no. 203, pp. 333–345, 1887.

[18] K. C. Zhou, R. Qian, A.-H. Dhalla, S. Farsiu, and J. A. Izatt, "Unified k-space theory of optical coherence tomography," *Advances in Optics and Photonics*, vol. 13, no. 2, pp. 462–514, 2021.

[19] J. A. Izatt and M. A. Choma, "Theory of optical coherence tomography," in *Optical Coherence Tomography: Technology and Applications*, Springer, 2008, pp. 47–72.

[20] M. A. Choma, M. V. Sarunic, C. Yang, and J. A. Izatt, "Sensitivity advantage of swept source and fourier domain optical coherence tomography," *Optics express*, vol. 11, no. 18, pp. 2183–2189, 2003.

[21] S.-H. Yun, G. J. Tearney, J. F. de Boer, N. Iftimia, and B. E. Bouma, "High-speed optical frequency-domain imaging," *Optics express*, vol. 11, no. 22, pp. 2953–2963, 2003.

[22] R. Leitgeb, C. Hitzenberger, and A. F. Fercher, "Performance of fourier domain vs. time domain optical coherence tomography," *Optics express*, vol. 11, no. 8, pp. 889–894, 2003.

[23] J. F. De Boer, B. Cense, B. H. Park, M. C. Pierce, G. J. Tearney, and B. E. Bouma, "Improved signal-to-noise ratio in spectral-domain compared with time-domain optical coherence tomography," *Optics letters*, vol. 28, no. 21, pp. 2067–2069, 2003.

[24] M. R. Hee, D. Huang, E. A. Swanson, and J. G. Fujimoto, "Polarization-sensitive low-coherence reflectometer for birefringence characterization and ranging," *JOSA B*, vol. 9, no. 6, pp. 903–908, 1992.

[25] C. K. Hitzenberger, E. Götzinger, M. Sticker, M. Pircher, and A. F. Fercher, "Measurement and imaging of birefringence and optic axis orientation by phase resolved polarization sensitive optical coherence tomography," *Optics express*, vol. 9, no. 13, pp. 780–790, 2001.

[26] J. F. De Boer, C. K. Hitzenberger, and Y. Yasuno, "Polarization sensitive optical coherence tomography–a review," *Biomedical optics express*, vol. 8, no. 3, pp. 1838–1873, 2017.

[27] C. J. Liu, W. Ammon, R. J. Jones, J. C. Nolan, D. Gong, C. Maffei, B. L. Edlow, J. C. Augustinack, C. Magnain, A. Yendiki, *et al.*, "Quantitative imaging of three-dimensional fiber orientation in the human brain via two illumination angles using polarization-sensitive optical coherence tomography," *bioRxiv*, pp. 2023–10, 2023.

[28] A. Guedan-Duran, N. Jemni-Damer, I. Orueta-Zenarruzabeitia, G. V. Guinea, J. Perez-Rigueiro, D. Gonzalez-Nieto, and F. Panetsos, "Biomimetic approaches for separated regeneration of sensory and motor fibers in amputee people: Necessary conditions for functional integration of sensory–motor prostheses with the peripheral nerves," *Frontiers in Bioengineering and Biotechnology*, vol. 8, p. 584 823, 2020.

[29] B. de Campos Vidal, M. L. S. Mello, A. C. Caseiro-Filho, and C. Godo, "Anisotropic properties of the myelin sheath," *Acta histochemica*, vol. 66, no. 1, pp. 32–39, 1980.

[30] A. S. Nam, J. M. Easow, I. Chico-Calero, M. Villiger, J. Welt, G. H. Borschel, J. M. Winograd, M. A. Randolph, R. W. Redmond, and B. J. Vakoc, "Wide-field functional microscopy of peripheral nerve injury and regeneration," *Scientific reports*, vol. 8, no. 1, p. 14 004, 2018.

[31] M. S. Islam, M. C. Oliveira, Y. Wang, F. P. Henry, M. A. Randolph, B. H. Park, and J. F. de Boer, "Extracting structural features of rat sciatic nerve using polarization-sensitive spectral domain optical coherence tomography," *Journal of Biomedical Optics*, vol. 17, no. 5, pp. 056 012–056 012, 2012.

[32] I. Saytashev, Y.-C. Yoon, B. J. Vakoc, S. Vasudevan, and D. X. Hammer, "Improved in vivo optical coherence tomography imaging of animal peripheral nerves using a prism nerve holder," *Journal of Biomedical Optics*, vol. 28, no. 2, pp. 026 002–026 002, 2023.

[33] M. Siddiqui and B. J. Vakoc, "Optical-domain subsampling for data efficient depth ranging in fourier-domain optical coherence tomography," *Optics express*, vol. 20, no. 16, pp. 17 938–17 951, 2012.

[34] M. Siddiqui, A. S. Nam, S. Tozburun, N. Lippok, C. Blatter, and B. J. Vakoc, "High-speed optical coherence tomography by circular interferometric ranging," *Nature photonics*, vol. 12, no. 2, pp. 111–116, 2018.

[35] G. P. Agrawal and N. A. Olsson, "Self-phase modulation and spectral broadening of optical pulses in semiconductor laser amplifiers," *IEEE Journal of quantum electronics*, vol. 25, no. 11, pp. 2297–2306, 1989.

[36] J. Nilsson, S.-U. Alam, J. A. Alvarez-Chavez, P. W. Turner, W. A. Clarkson, and A. B. Grudinin, "High-power and tunable operation of erbium-ytterbium co-doped cladding-pumped fiber lasers," *IEEE Journal of Quantum Electronics*, vol. 39, no. 8, pp. 987–994, 2003.

[37] C. R. Giles and E. Desurvire, "Modeling erbium-doped fiber amplifiers," *Journal of lightwave technology*, vol. 9, no. 2, pp. 271–283, 1991.

[38] C. M. Caves, "Quantum limits on noise in linear amplifiers," *Physical Review D*, vol. 26, no. 8, p. 1817, 1982.

[39] H. Heffner, "The fundamental noise limit of linear amplifiers," *Proceedings of the IRE*, vol. 50, no. 7, pp. 1604–1608, 1962.

[40] J. Shapiro, "Quantum noise and excess noise in optical homodyne and heterodyne receivers," *IEEE Journal of Quantum Electronics*, vol. 21, no. 3, pp. 237–250, 1985.

[41] B. L. Schumaker, "Noise in homodyne detection," *Optics letters*, vol. 9, no. 5, pp. 189–191, 1984.

[42] K. Kikuchi, "Fundamentals of coherent optical fiber communications," *Journal of lightwave technology*, vol. 34, no. 1, pp. 157–179, 2015.

[43] E. Ip, A. P. T. Lau, D. J. Barros, and J. M. Kahn, "Coherent detection in optical fiber systems," *Optics express*, vol. 16, no. 2, pp. 753–791, 2008.

[44] E. A. Rank, R. Sentosa, D. J. Harper, M. Salas, A. Gaugutz, D. Seyringer, S. Nevlacsil, A. Maese-Novo, M. Eggeling, P. Muellner, *et al.*, "Toward optical coherence tomography on a chip: In vivo three-dimensional human retinal imaging using photonic integrated circuit-based arrayed waveguide gratings," *Light: Science & Applications*, vol. 10, no. 1, p. 6, 2021.

[45] S. Shin, U. Sharma, H. Tu, W. Jung, and S. A. Boppart, "Characterization and analysis of relative intensity noise in broadband optical sources for optical coherence tomography," *IEEE Photonics Technology Letters*, vol. 22, no. 14, pp. 1057–1059, 2010.

[46] M. Al-Qadi, M. O'Sullivan, C. Xie, and R. Hui, "On the phase noise enhancement of a continuous wave in saturated soa used for rin reduction," *IEEE Photonics Technology Letters*, vol. 32, no. 7, pp. 430–433, 2020.

[47] D. J. Harper and B. J. Vakoc, "Relationship between axial resolution and signal-to-noise ratio in optical coherence tomography," *Optics letters*, vol. 47, no. 6, pp. 1517–1520, 2022.

[48] C. Heck, S. L. Helmers, and C. M. DeGiorgio, "Vagus nerve stimulation therapy, epilepsy, and device parameters: Scientific basis and recommendations for use," *Neurology*, vol. 59, no. 6_suppl_4, S31–S37, 2002.

[49] P. Cristancho, M. A. Cristancho, G. H. Baltuch, M. E. Thase, P. John, *et al.*, "Effectiveness and safety of vagus nerve stimulation for severe treatment-resistant major depression in clinical practice after fda approval: Outcomes at 1 year," *The Journal of clinical psychiatry*, vol. 72, no. 10, p. 5594, 2011.

[50] C. W. Austelle, G. H. O'Leary, S. Thompson, E. Gruber, A. Kahn, A. J. Manett, B. Short, and B. W. Badran, "A comprehensive review of vagus nerve stimulation for depression," *Neuromodulation: Technology at the Neural Interface*, vol. 25, no. 3, pp. 309–315, 2022.

[51] E. N. Nicolai, M. L. Settell, B. E. Knudsen, A. L. McConico, B. A. Gosink, J. K. Trevathan, I. W. Baumgart, E. K. Ross, N. A. Pelot, W. M. Grill, *et al.*, "Sources of off-target effects of vagus nerve stimulation using the helical clinical lead in domestic pigs," *Journal of neural engineering*, vol. 17, no. 4, p. 046 017, 2020.

[52] A. Fitchett, S. Mastitskaya, and K. Aristovich, "Selective neuromodulation of the vagus nerve," *Frontiers in neuroscience*, vol. 15, p. 685 872, 2021.

[53] S. L. Blanz, E. D. Musselman, M. L. Settell, B. E. Knudsen, E. N. Nicolai, J. K. Trevathan, R. S. Verner, J. Begnaud, A. C. Skubal, A. J. Suminski, *et al.*, "Spatially selective stimulation of the pig vagus nerve to modulate target effect versus side effect," *Journal of neural engineering*, vol. 20, no. 1, p. 016 051, 2023.

[54] M. L. Settell, N. A. Pelot, B. E. Knudsen, A. M. Dingle, A. L. McConico, E. N. Nicolai, J. K. Trevathan, J. A. Ezzell, E. K. Ross, K. J. Gustafson, *et al.*, "Functional vagotopy in the cervical vagus nerve of the domestic pig: Implications for the study of vagus nerve stimulation," *Journal of neural engineering*, vol. 17, no. 2, p. 026 022, 2020.

[55] A. R. Upadhye, C. Kolluru, L. Druschel, L. Al Lababidi, S. S. Ahmad, D. M. Menendez, O. N. Buyukcelik, M. L. Settell, S. L. Blanz, M. W. Jenkins, *et al.*, "Fascicles split or merge every 560 microns within the human cervical vagus nerve," *Journal of neural engineering*, vol. 19, no. 5, p. 054 001, 2022.

[56] N. A. Pelot, G. B. Goldhagen, J. E. Cariello, E. D. Musselman, K. A. Clissold, J. A. Ezzell, and W. M. Grill, "Quantified morphology of the cervical and subdiaphragmatic vagus nerves of human, pig, and rat," *Frontiers in Neuroscience*, vol. 14, p. 601 479, 2020.

[57] C. Kolluru, A. Todd, A. R. Upadhye, Y. Liu, M. Y. Berezin, F. Fereidouni, R. M. Levenson, Y. Wang, A. J. Shoffstall, M. W. Jenkins, *et al.*, "Imaging peripheral nerve micro-anatomy with muse, 2d and 3d approaches," *Scientific reports*, vol. 12, no. 1, p. 10 205, 2022.

[58] N. Thompson, E. Ravagli, S. Mastitskaya, F. Iacoviello, K. Aristovich, J. Perkins, P. R. Shearing, and D. Holder, "Determining the fascicular anatomy of the porcine vagus nerve with microct," *The FASEB Journal*, vol. 34, no. S1, pp. 1–1, 2020.

[59] M. L. Settell, A. C. Skubal, R. C. Chen, M. Kasole, B. E. Knudsen, E. N. Nicolai, C. Huang, C. Zhou, J. K. Trevathan, A. Upadhye, *et al.*, "In vivo visualization of pig vagus nerve "vagotopy" using ultrasound," *Frontiers in Neuroscience*, vol. 15, p. 676 680, 2021.

[60] S. Vasudevan, J. Vo, B. Shafer, A. S. Nam, B. J. Vakoc, and D. X. Hammer, "Toward optical coherence tomography angiography-based biomarkers to assess the safety of peripheral nerve electrostimulation," *Journal of neural engineering*, vol. 16, no. 3, p. 036 024, 2019.

[61] G. L. Monroy, M. Erfanzadeh, M. Tao, D. T. DePaoli, I. Saytashev, S. A. Nam, H. Rafi, K. C. Kwong, K. Shea, B. J. Vakoc, *et al.*, "Development of polarization-sensitive optical coherence tomography imaging platform and metrics to quantify electrostimulation-induced peripheral nerve injury in vivo in a small animal model," *Neurophotonics*, vol. 10, no. 2, pp. 025 004–025 004, 2023.

[62] B. Cense, T. C. Chen, B. H. Park, M. C. Pierce, and J. F. De Boer, "Thickness and birefringence of healthy retinal nerve fiber layer tissue measured with polarization-sensitive optical coherence tomography," *Investigative ophthalmology & visual science*, vol. 45, no. 8, pp. 2606–2612, 2004.

[63] Y.-C. Chang, M. Cracchiolo, U. Ahmed, I. Mughrabi, A. Gabalski, A. Daytz, L. Rieth, L. Becker, T. Datta-Chaudhuri, Y. Al-Abed, *et al.*, "Quantitative estimation of nerve fiber engagement by vagus nerve stimulation using physiological markers," *Brain stimulation*, vol. 13, no. 6, pp. 1617–1630, 2020.

[64] H. Nakaji, N. Kouyama, Y. Muragaki, Y. Kawakami, and H. Iseki, "Localization of nerve fiber bundles by polarization-sensitive optical coherence tomography," *Journal of neuroscience methods*, vol. 174, no. 1, pp. 82–90, 2008.

[65] F. P. Henry, Y. Wang, C. L. Rodriguez, M. A. Randolph, E. A. Rust, J. M. Winograd, J. F. de Boer, and B. H. Park, "In vivo optical microscopy of peripheral nerve myelination with polarization sensitive-optical coherence tomography," *Journal of Biomedical Optics*, vol. 20, no. 4, pp. 046 002–046 002, 2015.

[66] L. A. Havton, N. P. Biscola, E. Stern, P. V. Mihaylov, C. A. Kubal, J. M. Wo, A. Gupta, E. Baronowsky, M. P. Ward, D. M. Jaffey, *et al.*, "Human organ donor-derived vagus nerve biopsies allow for well-preserved ultrastructure and high-resolution mapping of myelinated and unmyelinated fibers," *Scientific Reports*, vol. 11, no. 1, p. 23 831, 2021.

[67] B. H. Park, M. C. Pierce, B. Cense, and J. F. De Boer, "Real-time multi-functional optical coherence tomography," *Optics express*, vol. 11, no. 7, pp. 782–793, 2003.

[68] M. Villiger, E. Z. Zhang, S. K. Nadkarni, W.-Y. Oh, B. J. Vakoc, and B. E. Bouma, "Spectral binning for mitigation of polarization mode dispersion artifacts in catheter-based optical frequency domain imaging," *Optics express*, vol. 21, no. 14, pp. 16 353–16 369, 2013.

[69] N. Stakenborg, P. J. Gomez-Pinilla, T. J. Verlinden, A. M. Wolthuis, A. D'Hoore, R. Farré, P. Herijgers, G. Matteoli, and G. E. Boeckxstaens, "Comparison between the cervical and abdominal vagus nerves in mice, pigs, and humans," *Neurogastroenterology & Motility*, vol. 32, no. 9, e13889, 2020.

[70] M. Menzel, K. Michielsen, H. De Raedt, J. Reckfort, K. Amunts, and M. Axer, "A jones matrix formalism for simulating three-dimensional polarized light imaging of brain tissue," *Journal of the Royal Society Interface*, vol. 12, no. 111, p. 20 150 734, 2015.

[71] N. Jayaprakash, W. Song, V. Toth, A. Vardhan, T. Levy, J. Tomaio, K. Qanud, I. Mughrabi, Y.-C. Chang, M. Rob, *et al.*, "Organ-and function-specific anatomical organization of vagal fibers supports fascicular vagus nerve stimulation," *Brain stimulation*, vol. 16, no. 2, pp. 484–506, 2023.

[72] J. Zhao, Y. Winetraub, L. Du, A. Van Vleck, K. Ichimura, C. Huang, S. Z. Aasi, K. Y. Sarin, and A. de la Zerda, "Flexible method for generating needle-shaped beams and its application in optical coherence tomography," *Optica*, vol. 9, no. 8, pp. 859–867, 2022.

[73] N. Thompson, S. Mastitskaya, F. Iacoviello, P. R. Shearing, K. Aristovich, and D. Holder, "Human vagus nerve fascicular anatomy: A microct segmentation and histological study," *BioRxiv*, pp. 2023–07, 2023.

[74] K. C. Zhou, R. Qian, S. Degan, S. Farsiu, and J. A. Izatt, "Optical coherence refraction tomography," *Nature photonics*, vol. 13, no. 11, pp. 794–802, 2019.